GRI-98/0089

GRI®

Annual Report

Development of Stimulation Diagnostic Technology

Prepared by:
Sandia National Laboratories

Gas Research Institute

Drilling and Completion Team
June 1998

GRI-98/0089 SAND98-1736

DEVELOPMENT OF STIMULATION DIAGNOSTIC TECHNOLOGY

ANNUAL REPORT
(January 1997-December 1997)

Prepared by
N. R. Warpinski,
J. E. Uhl,
B. P. Engler,
R.G. Keefe

Sandia National Laboratories
Department 6116
P.O. Box 5800
Albuquerque, New Mexico 87185

For
GAS RESEARCH INSTITUTE
Contract No. 5089-211-2059

GRI Project Manager
Steve Wolhart
Drilling and Completions Team

February 1998

GRI DISCLAIMER

LEGAL NOTICE This report was prepared by Sandia National Laboratories as an account of work sponsored by the Gas Research Institute (GRI). Neither GRI, members of GRI, nor any person acting on behalf of either:

a. Makes any warranty or representation, express or implied, with respect to the accuracy, completeness, or usefulness of the information contained in this report, or that the use of any apparatus, method, or process disclosed in this report may not infringe privately owned rights; or

b. Assumes any liability with respect to the use of, or for damages resulting from the use of, any information, apparatus, method, or process disclosed in this report.

REPORT DOCUMENTATION PAGE

Form Approved
OMB No. 0704-0188

1. AGENCY USE ONLY *(Leave blank)*	2. REPORT DATE	3. REPORT TYPE AND DATES COVERED
	June 1998	Annual Report, January 1997 to December 1998

4. TITLE AND SUBTITLE
DEVELOPMENT OF STIMULATION DIAGNOSTIC TECHNOLOGY

5. FUNDING NUMBERS
GRI contract no.
5089-211-2059

6. AUTHOR(S)
N.R. Warpinski, J.E. Uhl, B.P. Engler, R.G. Keefe

7. PERFORMING ORGANIZATION NAME(S) AND ADDRESS(ES)
Sandia National Laboratories
MS 0705
P.O. Box 5800
Albuquerque, New Mexico 87185

8. PERFORMING ORGANIZATION REPORT NUMBER
SAND97-1736

9. SPONSORING/MONITORING AGENCY NAME(S) AND ADDRESS(ES)
Gas Research Institute
8600 West Bryn Mawr Ave.
Chicago, IL 60631-3562

10. SPONSORING/MONITORING AGENCY REPORT NUMBER
GRI-98/0089

11. SUPPLEMENTARY NOTES

12a. DISTRIBUTION/AVAILABILITY STATEMENT

12b. DISTRIBUTION CODE

13. ABSTRACT *(Maximum 200 words)*

The approach to stimulation diagnostics is to integrate in situ stress measurements (including microfracs, anelastic strain recovery, circumferential velocity analysis, and coring-induced fractures) with natural fracture characterization, stimulation analyses (including FRACPRO®, other models, finite-element analyses, and various pressure analyses), and fracture diagnostics in order to validate hydraulic fracture concepts, models and diagnostic capabilities. During 1979 efforts centered on final analysis and documentation of the last three M-Site experiments and an interpretation of the meaning of those results. Microseismic tests were performed in the Mesaverde formation, Frontier sandstone, Barnett shale and the Wolfcamp formation. These tests provided information necessary to make changes to the 5-level system to improve its performance. In addition to the fielded experiments, another major task was the analysis of the Carthage Injection Experiment data set from the viewpoint of a single well. Some of these results are different from the original interpretation. Efforts also continue on developing automatic and customer-focused software for processing microseismic events. These various software packages will be used in real time, as post processors, and as customer products. Some work continued on the finite-element studies of the M-Site tiltmeter results, particularly with respect to the final C sandstone tests.

14. SUBJECT TERMS
Tight gas sands, in situ stress, stress measurement, natural fractures, hydraulic fracturing, hydraulic fracture diagnostics, microseisms, acoustic emissions, coring induced fractures, inclinometers, tiltmeters

15. NUMBER OF PAGES
100

16. PRICE CODE

17. SECURITY CLASSIFICATION OF REPORT	18. SECURITY CLASSIFICATION OF THIS PAGE	19. SECURITY CLASSIFICATION OF ABSTRACT	20. LIMITATION OF ABSTRACT
Unclassified	Unclassified	Unclassified	

Title	Development of Stimulation Diagnostic Technology
Contractor	Sandia National Laboratories GRI Contract Number: 5089-211-2059
Principal Investigator	N. R. Warpinski
Report Period	January 1997-December 1997 Annual Report
Objective	To apply Sandia's expertise and technology towards the development of stimulation diagnostic technology in the areas of in situ stress, natural fracturing, stimulation processes and fracture diagnostics.
Technical Perspective	Large quantities of natural gas exist in low permeability reservoirs throughout the US. Characteristics of these reservoirs, however, make production difficult and often uneconomic. Matrix rock permeabilities are often submicrodarcy, and natural fractures are commonly marginal, being anisotropic and easily damaged. Stimulation is required for these types of reservoirs, with hydraulic fracturing being the primary stimulation option. Understanding stimulation behavior is difficult, however, because of the complex nature of most of these reservoirs. Diagnostics that can map out the fracture length, height, and azimuth are the missing element in hydraulic-fracture analysis. Integrating knowledge of the matrix rock, natural fractures, in situ stresses with stimulation models and diagnostics is required if stimulation effectiveness is to be determined and enhanced.
Results	Activities during 1997 included the completion of M-Site analyses and the initiation of industry-centered experiments. At M-Site, the principal activity was the documentation of the C sandstone experiments. The microseismic analyses of the final two injections were finished and final images of the resultant fractures were produced. These results were again compared to the intersecting well results (e.g., multiple fractures in two intervals) and downhole tiltmeter analyses. In general, there was good agreement between the microseismic images and the other diagnostics. In addition to the diagnostics, analyses of fracture mechanisms were examined in order to attempt an explanation for the complexity, lack of height growth, and multiple fracturing that was observed at M-Site. Effects examined include tip behavior, secondary fractures, origin and significance of multiple fractures, pressure drop down fractures, and others. These analyses show that much of the observed behavior can be accounted for post-test, but the difficulty is in predicting it *a priori*.

Four industry diagnostic tests were conducted in 1997, including tests with Mitchell Energy, Barrett Resources, Crosstimbers and Chevron. The Crosstimbers test was a single-level feasibility test, while the other three were multi-level experiments. Results from these tests were mixed due to problems with the receiver system.

Analysis of the Carthage Cotton Valley diagnostic project microseismic data began in 1997. This industry consortium test is being re-analyzed from a single well perspective to provide an independent fracture map. In addition, the data will have a 5-level data set extracted and these data will be analyzed using SMART5 software.

A new-generation receiver system is being designed to improve reliability and to upgrade capabilities to a 200° C operating temperature, a 3-in diameter OD, and for use on current industry fiber-optic video wirelines.

Hardware upgrades are still being made to the 5-level wireline receiver array to improve reliability and operating effectiveness. The industry diagnostic tests have helped identify problems with the hardware system; most of these were corrected in late 1997.

Software programs to process data from these systems are being refined continually to accurately process data under varied conditions. SMART5 is now a usable real-time diagnostic code and VIEW5 is an editing and mapping version of SMART5.

Finite element analyses of the C sandstone inclinometer results were completed and gave the final validation of the microseismic data. A topical report on the tiltmeter calculations has been prepared.

Technical Approach

The approach to stimulation diagnostics is to integrate in situ stress measurements, natural fracture characterization, stimulation analyses (including FRACPRO™ other models, finite-element analyses, and various pressure analyses), and fracture diagnostics in order to validate hydraulic fracture concepts, models and diagnostic capabilities. From now until the end of the project, the emphasis will be on developing a diagnostics system to map out hydraulic-fracture length and other parameters. The methodology which can measure the most fracture attributes is the microseismic method, and most effort will be expended in developing and validating this technology. However, a second technology using a downhole tiltmeter array has also been found to be valuable for measuring some important fracture characteristics and some work will be performed on this technology. The ultimate goal is to develop real-time, industry-run, fracture-diagnostics capabilities.

Project Implications

The focus of this project is on stimulation diagnostics to be used for the optimization of hydraulic fracturing and field development. A key deliverable is to provide the foundation for a service to map hydraulic fractures using analysis of microseismic emissions from and near the hydraulic fracture. The use of microseisms to determine

fracture geometry was validated at M-Site during experiments conducted in the B-Sand and C-Sand. GRI and Sandia began field testing of the hydraulic fracture mapping service at other sites in 1997; this will continue in 1998.

Steve Wolhart
Principal Project Manager, Drilling & Completion

TABLE OF CONTENTS

Tables

Figures

1.0 RESEARCH OBJECTIVES

The objective of this project is for Sandia National Laboratories to apply its expertise and technology towards the development of stimulation diagnostic technology. Stimulation diagnostic technology contains elements such as in situ stress measurements, fracture modeling, and reservoir characterization, but the primary emphasis is on fracture diagnostics which can image the entire fracture. Development of this technology will yield a more complete analysis of hydraulic fracture behavior and effectiveness in the reservoir, and efforts are geared towards developing microseismic fracture diagnostics into a reliable, accurate, near-real time service.

The primary emphasis is on microseismic monitoring, as this technology is believed to be the one foreseeable technology which can image the length, height, azimuth and asymmetry of a hydraulic fracture. Most efforts are concentrated on the microseismic method, but previous GRI research has shown that a downhole tiltmeter array can provide other important information and some limited work on this technology is also ongoing.

The advancement of microseismic (and other seismic) monitoring requires rigorous standards for receivers, recorders, and processing algorithms. Completion of this task requires the application of advanced multi-station receivers that can faithfully record the particle motion induced by the specific events, the use of telemetry and recorders with sufficient dynamic range and band width to transmit and store the data, and the development of analysis techniques that can be applied in real-time or near-real-time modes.

Field experiments are an integral part of GRI's stimulation & completion research and the means by which models, diagnostics, and other procedures can be tested, refined, and verified. Sandia had a lead role in the diagnostic phases of the M-Site tests that were conducted in the Piceance basin near Rifle, CO. This work included the design of the instrumentation string of accelerometers and tiltmeters for a newly drilled monitor well and the application of wireline microseismic instrumentation for existing wells. These field experiments provided the baseline information for developing the hardware and processing algorithms for fracture diagnostic analysis.

In addition to the M-Site activities, Sandia jointly conducted other field experiments with interested companies in other locations. These tests allowed for data to be obtained in other formations with different properties, stresses, depths, etc., and they will also serve as test sites for technology developed under this project.

The objective of these field tests is to provide a test mechanism for exercising the hardware system and the automatic processing codes that are being developed and refined. Of primary importance is the testing and validation of SMART5 and associated software for automatic processing of the microseismic data and the adaptation of the Vidale-Nelson algorithms for fast use in microseismic analysis.

Work on downhole tiltmeters is primarily concentrated on analytic and finite-element analyses of tiltmeter data to extract geometry parameters. However, some work on new tiltmeter devices which could be integrated into downhole receivers is ongoing.

2.0 SUMMARY OF ALL PREVIOUS WORK PERFORMED

2.1 In Situ Stress

Previous work on in situ stresses includes ASR analyses of SFE-4, Canyon Sands, and UPRC Frontier core, and Circumferential Velocity analyses of the same core plus Maxus Cleveland formation and Berea core. In addition, detailed core measurements of stress and material properties were made on an M-Site sandstone sample. A core-based stress-measurement report (GRI-93/0270)[1] and a follow-up stress-azimuth report (GRI-93/0429)[2] were prepared as part of this work. Most recently, the downhole tiltmeters installed at M-Site have been used to accurately determine the closure stress in the B sandstone using a re-opening technique. The tiltmeters have also shown that normal shut-in and flow-back closure-stress techniques do not provide clear closure-stress data because there is no well-defined mechanical closure during the fracture closure process.

2.2 Natural Fractures

Previous natural fracture studies included (1) Green River basin fieldwork which identified two primary fracture sets and (2) efforts to reconstruct the tectonic development of the basin which led to the development of the fractures. These results have been documented in two topical reports (GRI-94/0020[3] and GRI-95/0151[4]) covering the Green River basin. Studies of natural fractures in core were used to develop a theory of the role of diagenesis in fracture development. This theory has proved useful in explaining Frontier fracture systems. Other limited work has been ongoing with local Green River basin operators.

2.3 Stimulation

Previous stimulation activities include most importantly the analysis and documentation of the Fracture Propagation Modeling Forum results. These data were included in an SPE paper (SPE 25890[5]) and GRI report (GRI-93/0109[6]) summarizing the results. Other modeling activities have been conducted to assess site suitability and for comparison with M-Site results.

2.4 Diagnostics

Fracture-diagnostics field work began in 1992 at the M-Site location for site suitability testing and continued in 1993 at the M-Site for the "A" sand experiments. These experiments form the basis for all of the M-Site design work and the development of processing codes for fracture diagnostics.

The suitability testing was performed in order to assess whether the M-Site near Rifle was acceptable for fracture diagnostic research. Results from that test were highly positive, indicating that microseisms were generated in large numbers, they were highly analyzable, and they could be used to map fracture progress. Results of these tests were documented in an SPE paper[7] and GRI-93/0050.[8]

The "A"-Sand Multi-Level and Treatment-Well Diagnostic Tests was conducted in October-November of 1993. These tests included a detailed velocity survey and four fracturing experiments monitored with a four-level receiver system in an offset well and a single receiver (or other instrumentation) in the treatment well. Results showed a very asymmetric fracture with considerable height growth. Results of these tests are documented in SPE 27985,[9] SPE 30507[10] and GRI-95/0046.[11]

Instrumentation for the new M-Site monitor well was designed and emplaced during 1994. These instrument systems included 30 triaxial receiver arrays and 6 biaxial inclinometer arrays that were grouted in the new monitor well at M-Site. Initial check-out of the instrumentation showed extremely high noise levels due to the rural power system and large amount of drilling activity in the area. These noise problems were solved by:

- designing and fabricating new amplifier and power-supply systems that were highly shielded from the both electric and magnetic fields
- providing electric and magnetic shielding for all surface cable runs

- using isolation transformers on all instrumentation
- using battery power for all power supplies

The B sandstone experiments were conducted in 1995, although analysis continued into 1996. Seven separate fracture injections were conducted and monitored using microseismic and inclinometer arrays. Except for the initial breakdown injection, sufficient microseismic diagnostics were obtained to construct video images of fracture growth with time and pressure.

After the breakdown, the three following injections were water fractures which resulted in contained fracture behavior and rapid lateral growth out to lengths of almost 400 ft for volumes up to 200 bbl. The two subsequent injections were linear-gel minifracs which initiated similarly to the water fracs, but eventually experienced some height growth when net pressures became large enough. These minifracs had injected volumes of 400 bbl.

Finally a propped fracture treatment was conducted using about 600 bbl of crosslinked gel and 80,000 lb of sand. This test was considerably more complicated than the earlier injections. The fracture initiated much like the linear-gel minifracs, but pressures rose significantly above those observed during the minifracs and considerable height growth occurred. Results of the B sand experiments are documented in SPE 36452,[12] SPE 36451,[13] SPE 36449[14] and SPE 36450.[15]

The C sand experiments were conducted in 1996, completing all M-Site activities prior to abandonment of the site in early 1997 at the request of the operator. There were six injections in the C sandstone, including a cross-linked-gel breakdown, two linear-gel minifracs, two cross-linked-gel minifracs, and a propped stimulation. The unique feature of the C sand experiments was the drilling of a lateral deviated borehole through the C sand prior to any fracture injections. This borehole intersected the C sandstone at a location approximately 300 ft from the treatment well on the east wing and was used to determine the fracture characteristics at that location and the timing of fracture intersection.

The first three injections were conducted in August, 1996 and resulted in high-quality microseismic maps of fracture growth. In particular, the second injection intersected the deviated lateral well and provided a validation of the length of the fracture, as determined by the microseisms. The difference in the measured fracture length vs the microseismically imaged length was at most a few tens of feet, approximately the accuracy of the technology. The fourth injection was conducted in November, 1996 and resulted in a complex asymmetric fracture which was clearly affected by the complex cross-linked-gel fluid system. Approximately 800 analyzable microseisms were detected and provided high-quality information on fracture growth and behavior.

The final two injections in the C sandstone were conducted in late December of 1996. These results were analyzed in 1997.

To validate the fracture heights using inclinometers (downhole tiltmeters), analytic models were developed for 2-D, radial, and flat elliptic cracks. These models were implemented in a real-time inclinometer monitoring program which plots tilt as a function of time and as a function of depth. The analytic models can be superposed on the tilt data and parameters can be varied to obtain an acceptable match of the models with the measured data. To assess the effects of layers, moduli differences, and stress contrasts, a finite-element tilt code was implemented in both 2D and 3D geometries. For the B sandstone, tiltmeter finite element analyses showed good agreement in fracture height values compared to the microseismic heights.

An algorithm by Vidale and Nelson[16,17] was chosen as the best tool for advanced analysis of microseisms in complicated layered media. This algorithm solves the Eikonal equations to determine the travel time from each receiver to every point in a grid space encompassing the microseismic volume of interest. The results are stored in files for each receiver and for each phase (e.g., p and s waves). When arrival time data for an event have been determined, a minimization routine is used to determine the best fit location to match the arrival times. This routine is guaranteed to find an absolute minimum, unlike most other algorithms which may stop at a local minimum. This code can also be ported to a personal computer and used for field processing.

A real-time automatic processing routine named SMART5 has been written for field analysis of multi-level microseismic data in a single well. This routines picks p waves, finds polarization information, and locates the events. This code is currently being upgraded for s-wave analysis and other features.

3.0 SPECIFIC OBJECTIVES OF THE CURRENT YEAR

Specific objectives of the current year are:

Complete analysis of M-Site C sandstone experiments and prepare documentation of those results, including SPE papers and final reports.

Begin technology transfer seminars of all M-Site results.

Conduct several industry fracture diagnostic tests to evaluate system and processing capabilities.

Continue the development of codes for using Vidale-Nelson algorithm to located microseisms in a layered structure.

Perform finite-element analyses of M-Site C-sandstone inclinometer results.

Refine software codes for the automatic processing of microseismic data (SMART5). Most importantly, the code will be updated to include automatic processing of the s wave.

Upgrade hardware for the 5-level system to improve reliability and functionality.

Begin development of a new-generation receiver system.

4.0 WORK PLANS FOR THE CURRENT YEAR

Work plans for the current year include:

Complete all QA work on M-Site C-sandstone microseismic locations. Prepare maps and visualizations of all of these tests and complete documentation in a final report and SPE papers. Conduct technical seminars on all M-Site results and the implications for fracturing.

Perform analyses of M-Site fracturing results to interpret unusual aspects of fracture height growth, multiple fracturing, fracture complexity, large pressure drops, and short lengths.

Conduct fracture experiments in several different basins for interested oil companies. Locations of interest include the Green River basin, Piceance basin, Barnett shale, and west Texas.

Provide analysis capabilities for the Carthage Cotton Valley Diagnostic project.

Continue the refinement of SMART5, the automatic processing system for microseismic detection and location. Add a second code for editing and re-mapping data; this code will be available to customers for their own QC and analysis efforts.

Continue the development of advanced codes for microseismic location algorithms using both homogeneous and layered-earth models. Complete a joint p/s regression for locating microseisms in a uniform velocity field and continue the porting of the Vidale-Nelson algorithms for use on a PC platform.

Conduct finite-element analyses of the M-Site C-sandstone inclinometer results to obtain the best possible height estimate for comparison with the microseismic data. These results show the accuracy of the microseismic method by comparing the microseismic-calculated heights with the mechanical heights, as deduced from inclinometer-measured deformation.

Perform hardware upgrades on the current 5-level receiver system to improve reliability. Efforts will be concentrated on the areas of receiver diagnostics and power distribution.

Begin design of a new generation receiver system that is capable of higher temperatures (200°C), is capable of being used in $4\text{-}^{1}/_{2}$ in casing (3-in OD), and is capable of being run on industry video wirelines.

5.0 PROCESSING SOFTWARE FOR MICROSEISMIC ANALYSIS

There are many levels of software needed for adequately processing, checking, editing, and distributing microseismic imaging data. These include the software for data acquisition, real-time processing codes (SMART5), quality control codes which can be used to examine microseismic waveforms in detail, codes which can edit and remap data (VIEW5), advanced processing codes, visualization codes, and sundry codes for maintaining, checking or altering data and results.

5.1 SMART5

The primary code for real-time processing of seismic data is SMART5, which stands for Seismic Monitoring & Analysis in Real Time, 5-level. To understand how SMART5 operates, it is first necessary to describe the entire software system and how SMART5 fits into it. Figure 1 shows the flow of 5-level data. Since the microseisms are digitized downhole, there is no A/D converter required for uphole data acquisition. The Manchester-coded data from downhole are brought into a handling interface where they are decoded and sent to full backup and to the data acquisition PC. In the data acquisition PC, the event data are displayed on a bubble meter and processed through an initial amplitude event-detection algorithm. If events are declared, they are also displayed on the screen for a quick perusal. These events are also written to a file and sent across a network to a second PC for storage and for further processing by SMART5.

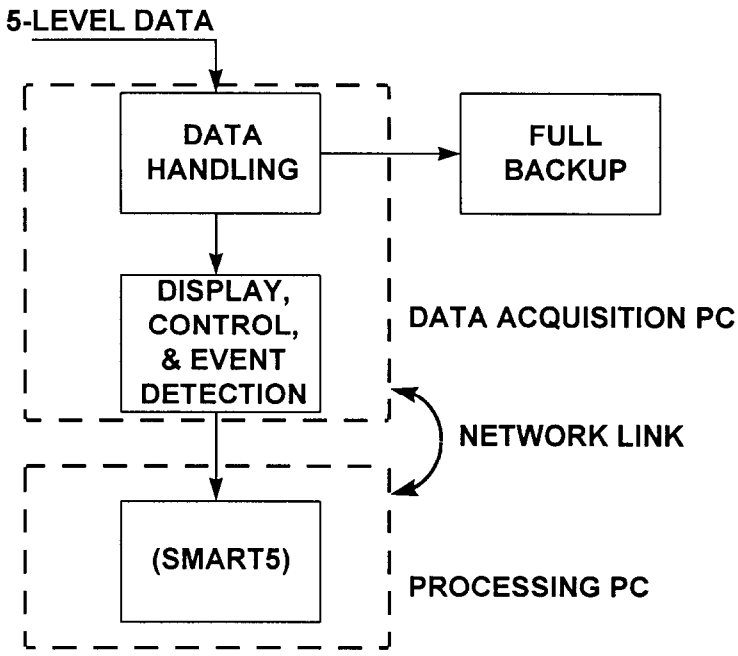

Figure 1. Block diagram of microseismic data processing.

The SMART5 code reprocesses the event and determines if it is a likely microseism (as opposed to noise or an electrical glitch). If it appears to be a microseism, the p-wave arrival, s-wave arrival, and p-wave polarization are determined and the event is located. The initial event-location scheme in SMART5 assumes uniform p and s velocities throughout the formation and uses a joint p-s regression to determine the correct elevation and distance to the microseism. The azimuth determined from the p-wave particle motion (a hodogram of its polarization) completes the location of the microseism in three-dimensional space. While hodograms can result in errors of as much as 10° in azimuth on any given level, the statistics generated from hodograms on each of 5 levels generally reduces the uncertainty to a few degrees.

5.1.1 Joint P-S Regression

The initial location analysis in SMART5 uses a joint p-s regression to calculate the elevation of and distance to the microseism. The equation which is minimized is

$$F = w_p \sum_n \left[V_{pi}^2 \left(t_{pi} - t_o\right)^2 - \left(r_i - r_o\right)^2 - \left(z_i - z_o\right)^2 \right]^2 + w_s \sum_m \left[V_{si}^2 \left(t_{si} - t_o\right)^2 - \left(r_i - r_o\right)^2 - \left(z_i - z_o\right)^2 \right]^2 ,$$

where the V_{pi} and V_{si} are the p and s velocities, r refers to the horizontal distance, z refers to the elevation, t is the time, the subscript "o" denotes the origin location and the subscript "i" denotes the i[th] receiver. The n and m variables are the numbers of p-wave and s-wave arrivals respectively. Variables w_p and w_s are weighting functions which can be used if one of the phases has less certainty than the other. The result of the minimization is the location coordinate, (r_O, z_O, t_O), which places the microseism in a two-dimensional vertical plane at the time the microseism occurred.

The minimization process results in the following three equations.

$$w_p \sum_n \left(z_o - z_{pi}\right)^2 - w_p V_p^2 \sum_n \left(t_{pi} - t_o\right)^2 + w_s \sum_m \left(z_o - z_{si}\right)^2 - w_s V_s^2 \sum_m \left(t_{si} - t_o\right)^2 + (w_p m + w_s n) r_o^2 = 0$$

$$w_p r_o^2 \sum_n \left(z_o - z_{pi}\right) + w_p \sum_n \left(z_o - z_{pi}\right)^3 - w_p V_p^2 \sum_n \left(t_{pi} - t_o\right)^2 \left(z_o - z_{pi}\right) + w_s r_o^2 \sum_m \left(z_o - z_{si}\right) + w_s \sum_m \left(z_o - z_{si}\right)^3 - w_s V_s^2 \sum_m \left(t_{si} - t_o\right)^2 \left(z_o - z_{si}\right) = 0$$

$$w_p r_o^2 \sum_n \left(t_{pi} - t_o\right) + w_p \sum_n \left(z_o - z_{pi}\right)^2 \left(t_{pi} - t_o\right) - w_p V_p^2 \sum_n \left(t_{pi} - t_o\right)^3 + w_s r_o^2 \sum_m \left(t_{si} - t_o\right) + w_s \sum_m \left(z_o - z_{si}\right)^2 \left(t_{si} - t_o\right) - w_s V_s^2 \sum_m \left(t_{si} - t_o\right)^3 = 0$$

The solution of these equations for r_O, z_O, and t_O is quite complicated, as all of the terms need to be multiplied out to extract and solve for the variables. However, this approach was chosen because it allows us to use any collection of p-wave and s-wave data that is available. It is not necessary to have both p and s data on the same level, nor is it even necessary to have any data from either phase (although there must be three arrival times to solve the equations).

The second advantage to using this approach is that it lends itself to fast uncertainty analyses using standard regression methods. To use standard methods, however, it is first necessary to transform the regression equation to standard form. Given the following substitutions

$$y_i = z_{pi}^2 - V_p^2 t_{pi}^2 , \quad \text{for p waves;}$$

$$y_i = z_{si}^2 - V_s^2 t_{si}^2 + t_o^2 \left(V_p^2 - V_s^2\right) , \quad \text{for s waves;}$$

$$x_{1i} = z_{pi} , \quad \text{for p waves;}$$

$$x_{1i} = Z_{si} , \quad \text{for s waves;}$$

$$x_{2i} = V_p^2 t_{pi} , \quad \text{for p waves;}$$

$$x_{2i} = V_x^2 t_{si} , \quad \text{for s waves.}$$

The distance equation can now be written as

$$y_i = a_o + a_1 x_{1i} + a_2 x_{2i} ,$$

where

$$a_o = V_p^2 t_o^2 - r_o^2 - z_o^2 ,$$

$$a_1 = 2z_o \text{ , and}$$
$$a_2 = -2t_0 \text{ .}$$

This equation is now in a standard format for multiple regression. Note that while this equation appears much easier to solve than the one actually used, it would require an iterative solution since t_O is in the y_i term. Thus the direct solution above is preferred.

We can now take averages and normalize the equation to get

$$Y_i = a_1 X_{1i} + X_{2i} \text{ ,}$$

where

$$Y_i = y_i - a_o$$
$$X_{1i} = x_{1i} - \sum_p x_{1i}$$
$$X_{2i} = x_{2i} - \sum_p x_{2i}$$

and p is the total number of arrival times in the regression. Since the variances of a_1 and a_2 are simple, i.e.,

$$S_{a1} = \frac{s}{\sum_p X_{1i}}$$

$$S_{a2} = \frac{s}{\sum_p X_{2i}}$$

with s being the deviations mean square,

$$s^2 = \frac{\sum_p \left(Y_i - \hat{Y}_i\right)^2}{p-3} \text{ ,}$$

and $\hat{Y}_i$ obtained from X_{1i} and X_{2i}, the variance of z_0 and t_0 are found readily as

$$s_{z_o} = \frac{1}{2} S_{a1}$$

$$s_{t_o} = \frac{1}{2} S_{a2}$$

from the definitions of a_1 and a_2.

The determination of the variance of r_O is considerably more difficult since the definition of a_O involves several terms and squares of those terms. To obtain an estimated variance of r_O, a predicted value can be obtained from

$$\hat{r}_{oi} = \sqrt{-y_i + a_1 x_{1i} + a_2 x_{2i} + V_p^2 t_o^2 - z_o^2} \text{ ,}$$

from which an expected value and a variance can be obtained. The resultant value of s_{r_o} will only be an approximation for the true value, but it has been found to be consistent with separate determinations of distance to the microseism (e.g., from each individual level) and the resultant variance in those distances.

5.1.2 Detection of S-Wave Arrival

From the initial studies of the location capabilities of SMART5, it was found that using only the p-wave arrival will result in quite accurate estimation of the microseismic origin elevation, but yield large uncertainty in the location distance for relatively closely spaced arrays (as the array aperture increases, this problem is reduced, but is still significant; alternately, more receivers would also reduce the problem). To provide the highest quality results, an s-wave-arrival detection algorithm was constructed for use in SMART5. This algorithm is relatively simple for fast processing on the PC, but we believe that it captures all of the essentials for accurate processing.

The algorithm allows for a weighted average of the three primary indicators of an s wave. These include:

- reduction in frequency compared to the p wave;
- change in amplitude relative to the immediately preceding part of the wave train;
- approximately 90° change in polarization compared to the p wave

The implementation of these features clearly requires that a p wave be detected on the given level, as it is necessary to look for changes in both frequency and phase.

The frequency shift is handled by using a higher-order crossing (HOC) approach to quickly estimate frequency in a given section of the waveform. The HOC approach is equivalent to counting how many times the wave crosses from negative to positive amplitude, except that it is based on the derivative of the amplitude to avoid problems with DC offsets and to capture any changes in the amplitude behavior. In this way, any change in the waveform from declining amplitude to increasing amplitude and vice versa is captured. The HOC method is simply implemented by taking the difference of successive points and comparing the ratio of the current difference with the previous difference. A sign change indicates an HOC. The waveform is divided into running bins of pre-set sizes and the number of HOC's is calculated for each bin. A clear reduction in the number of HOC's is indicative of a reduction in frequency. The running bins are started at the p-wave arrival point in order to obtain the baseline frequency information from which to make a decision about the s wave. Generally, the HOC data are filtered by raising them to some power to increase the difference between the discrete difference values. They are then weighted for the decision algorithm.

The amplitude shift is handled by taking rms amplitude measurements over running bins, again starting at the p-wave arrival time. A large increase in the rms amplitude of several bins is taken as an indication of a new wave impinging on the receivers. These data are normalized and weighted for use in the decision algorithm.

The polarization shift is accomplished by determining the hodogram angle of running bins and comparing the bin angle to the original p-wave azimuth. Bins are assigned a value of 1 if no phase shift and 2 if a phase shift exists. The offset angle for deciding on a phase shift can be preset. These data are then weighted for the decision algorithm

Finally, the results from the three processes are combined in a product function which can be tested all along the waveform to find the most likely location for an s-wave arrival. The task now is to test this algorithm with many different data sets to find the best values for the preset variables.

5.2 VIEW5

SMART5 contains a large amount of GRI-proprietary software which should not be arbitrarily distributed. However, SMART5 is also a versatile editing and mapping package which can be used to QC the results and change them as needed. To make these editing and mapping features available to customers of this product, a second software package, called VIEW5, has been extracted from SMART5 for this application. VIEW5 is able to access all of the data files, map file, and information files used and generated by SMART5 in order to display event waveforms, hodograms, and locations. VIEW5, however, does not have the p-wave arrival routine or the s-wave arrival routine. Any changes in the picks must be performed manually.

5.3 Vidale-Nelson Algorithm

The Vidale-Nelson algorithm[16,17] has now been fully ported to the PC environment. This code is an advanced processing code which finds the best location for a microseism using the full velocity structure of the formation. It is intended as a refinement of the joint p-s regression in SMART5, which assumes a uniform velocity field for both the p and s waves. The method of application of the original Vidale-Nelson algorithm required that 5 separate codes be run and many arrival time files be written and kept track of to perform an analysis. A single code has been written to manage these five codes and allow the data to be analyzed using one program.

Additional work still needs to be performed to improve the data-input method, as it is still quite cumbersome. We expect to put a revised input methodology into this algorithm sometime in 1998.

6.0 MICROSEISMIC RECEIVER HARDWARE

Considerable effort was expended in 1997 on receiver-system hardware issues. These included problems and refinements with the receivers, the fiber optics, the interconnects between receivers, the data acquisition equipment, and the surface communications, as well as the design of a new receiver system.

7.0 M-SITE MODELING ACTIVITIES

Some form of stimulation, usually hydraulic fracturing, is required for the economic production of gas from tight reservoirs. A long-sought objective has been comprehensive hydraulic-fracture models that could be used for the design, analysis, and, ultimately, real-time control of the fracturing process. In order to help validate such comprehensive models, Sandia is tasked to (1) analyze appropriate field stimulation and minifrac data in order to obtain an independent assessment of fracture performance, and (2) conduct any advanced activities (e.g., finite element analyses, model comparisons, etc.) which provide independent confirmation of model validity.

Activities in 1997 centered on interpretation of M-Site experimental results. Particular areas studied were fracture height growth, multiple fracturing, pressure drops, fluid-system effects, volumetric discrepancies, and fracture complexity. Table 1 gives a summary of some of the important pressure, volume, rate, and geometry features that were measured in the B- and C-sandstone injections. These results will be used for the following analyses.

Table 1 Geometry parameters from microseismic results

TEST	FLUID	RATE (bpm)	NET P (psi)	VOL (bbl)	WEST L (ft)	EAST L (ft)	TOTAL H (ft)	H ABOVE ZONE** (ft)	H BELOW ZONE** (ft)
1-A	LINEAR	25	1000	590	100	250	265	125	100
1-B	X-LINK	7	850	19	---	---	---	---	---
2-B	KCL	3	700	27	200	150	40	0	0
3-B	KCL	10	900	100	250	325	55	5	5
4-B	KCL	10	900	210	275	425	55	5	5
5-B	LINEAR	22	1300	400	250	375	80	30	5
6-B	LINEAR	22	1300	400	300	400	75	25	5
7-B*	X-LINK	20	2000	670	325	425	135	90	0
1-C	X-LINK	20	1000	95	200	200	105	25	0
2-C	LINEAR	20	900	132	375	425	80	0	0
3-C	LINEAR	22	1000	247	425	475	100	15	5
4-C	X-LINK	40	1200	982	350	625	200	80	40
5-C	X-LINK	30	1400	480	450	475	140	30	30
6-C*	X-LINK	30	2000	2118	425	450	190	40	70

* Treatments Include Proppant ** Zone thicknesses are: A sand- 40 ft; B sand-45 ft; C sand-80 ft

7.1 Fracture Height Growth

Results from the B and C sandstone injections showed a limited amount of fracture height growth even though pressures were well in excess of the confining stresses in the adjacent shales, mudstones, and siltstones. As can be seen in Table 1, there is very little height growth for most of the injections relative to the high net pressures measured during each of the tests. Of major interest are the propped fractures (7-B & 6-C), but complications due to sand effects on the rheology, proppant bridging, and near-well pressure drops make these fractures difficult to analyze. Nevertheless, much information can be gleaned by examining injections which have relatively simple fluid systems, in this case the following groupings of tests:

- 3-B & 4-B net pressure = 900 psi
- 5-B & 6-B net pressure = 1300 psi
- 2-C net pressure = 900 psi
- 1-C & 3-C net pressure = 1000 psi
- 5-C net pressure = 1400 psi

In all 5 groups of tests, there was considerably less height growth than would be predicted from most fracture models. Possible reasons for the better-than-expected containment include:

1. high-stress layers that were missed during stress testing,

2. high-permeability layers such as coals,
3. enhanced tip effects,
4. full slip at some interface, or
5. other stress/energy-dissipative processes.

The second containment feature, high-permeability layers, can be ruled out because these rocks are less than 0.1 md, water saturations are relatively high (60-70%), and there are few natural fractures and no coals at this depth.

The first and third features can be examined by calculating the stresses or fracture toughnesses required to contain the fractures to the size measured. This calculation can be performed with a fracture model, but most models have time dependence associated with their height calculations that make cross correlations difficult. A more straightforward approach is to perform equilibrium height calculations which, although they are the limiting cases, should be quite good for these tests because the amount of height growth is so small. In this case equilibrium height growth calculations were performed with a model which accounts for various layers having different stresses and toughnesses, but it does not account for modulus effects.

Two sets of calculations were performed to examine this problem. In the first set, the stress within the pay zone was kept at its measured value and the bounding stresses were increased until they resulted in the appropriate level of containment. In the second set, all stresses were set at their measured values and the fracture toughnesses of the bounding layers were increased until the correct height growth was achieved. Table 2 shows the results of these calculations. For the first set of calculations, it shows a comparison of the stress needed to contain the different injections (columns 3 and 4) to the measured stresses (columns 5 and 6). For the second set of calculations, it shows the fracture toughnesses needed to contain the fractures at the required locations.

Table 2. Calculated stress and toughness values need to produce the observed fracture height

Zone	Pressure (psi)	Stress Above (psi)	Stress Below (psi)	Measured Stress Above (psi)	Measured Stress Below (psi	Fracture Toughness (psi$\sqrt{in}$)
3-B & 4-B	900	5000	5000	4500	4600	15,000
5-B & 6-B	1300	4700	6000	4500	4600	22,500
2-C	900	5400	5400	3800	4500	25,000
1-C & 3-C	1000	4600	5800	3800	4500	31,000
5-C	1400	5200	5200	3800	4500	42,000

These results immediately suggest that the first possible explanation for containment, that of high-stress layers being present but not measured, is probably not tenable. At the M-Site location, approximately 75 stress measurement[15] have been made between 4000 and 8000 ft in all lithologies, but no measurements have exceeded the lithostatic stress. Given a maximum possible lithostatic stress of 1.07 psi/ft, the B-sand maximum stresses should be about 4800 psi and the C sand about 4600 psi. Since stresses of 5000-6000 psi are needed to contain the fractures in both zones, unmeasured high-stress layers cannot be a reasonable explanation.

Fracture-toughness values that would produce the correct fracture size are about an order of magnitude larger than the values measured in lab tests and must increase with increasing net pressure (and fracture size). These calculations are not meant to imply that higher fracture-toughness values are the correct solution, but rather they give the magnitude of the tip effect needed to produce the required containment. In fact, the full-slip and dissipative features are similar to the enhanced tip one. They all suggest that something else is happening at the fracture tip in these highly layered fluvial reservoirs.

An alternate approach to the containment issues is to treat the layered-rock medium as a composite material, since features of composite materials result in some degree of enhanced toughness, interface slip, and stress and energy dissipation. Figure 2 shows a schematic of the types of behavior found in laminates undergoing fracture. In this figure, the darker layers are the strength members (e.g., sandstones) while the white layers are weaker and possibly ductile (e.g., shales). The left figure shows that the strength members take much more stress and can microfracture

ahead of the tip, thus dissipating energy but also creating a situation that could explain multiple fractures. Each of the microfractures could begin to propagate if fracture fluid can migrate out to them through bedding planes, natural fractures, or other open paths. The center figure shows interface slip, which could entirely contain the fracture or could result in offsets if the fracture breaks through the strength layer. The right figure shows yielding in the soft material, which obviously dissipates stress and energy and could result in discontinuous fracture growth through the shale layers.

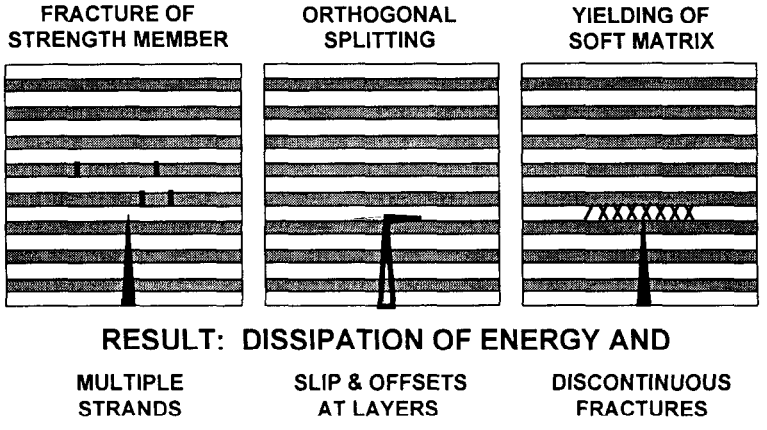

Figure 2. Composite behavior for height growth.

Although there is uncertainty in the operative mechanisms, it is worth noting the significance of applying the correct containment mechanism. Figure 3 shows two width contours for the 1000-psi C-sand calculations (fourth case above). The contour labeled "stress" shows the fracture width that is achieved if higher-stress layers are used to contain the fracture to the measured height. The "K_{Ic}" calculation shows the profile if some tip mechanism stopped fracture growth. Note that there is a 28% difference in fracture area in these two cases, and thus a 28% difference in volume. If containment is achieved by some tip effect and is modeled by using large stress contrasts, the predicted fracture will be much longer than it should be as less fluid is in stored volume. If containment is achieved by stress contrasts but is modeled as a tip effect, then the predicted fracture will be much shorter than it actually is. Of course, if one uses the original stress and does not realize that the fracture is contained, then the predicted fracture length will also be much shorter than it should be.

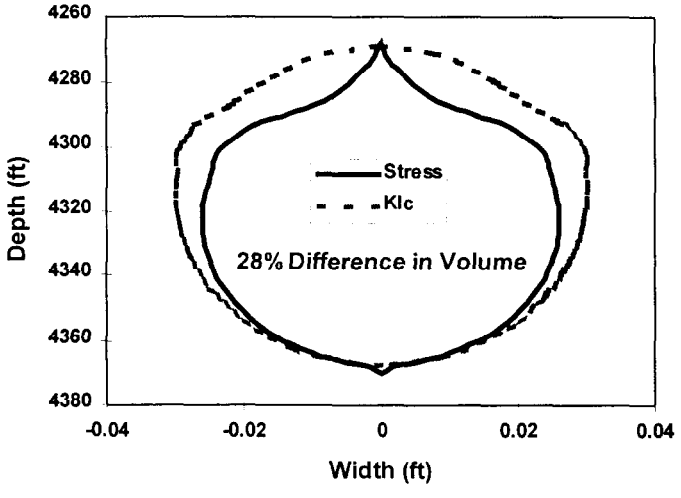

Figure 3. Width profiles for stress and toughness cases.

7.2 Multiple Fractures

As more cored hydraulic fractures are obtained, it is becoming clear that multiple fractures are a common occurrence. At the M-Site location, the following fracture statistics have been observed in three different cores through hydraulic fractures:

Depth(ft)	Number	Intervals	Separation (ft)
7000	37	2	50
4500	11	1	NA
4300	15	2	47

These statistics include the total number of fractures seen in each test and whether those fractures were seen in one or more intervals.

In attempting to sort out the relevance of multiple fractures to hydraulic fracturing, two major issues arise:

- how are multiple fractures generated and
- how important are they to the fracturing process.

While the genesis problem may appear to be a more basic research problem, it is very relevant to current fracturing practices because it may suggest much about the details of the fracture-tip process zone and, therefore, the way fracture tips should be modeled.

One mechanism for generating multiple fractures has already been suggested and has been observed in the composites literature. A highly layered material will spread the stress field ahead of the crack and could result in fracturing of the strength members in multiple locations (mechanism 1 in Figure 2). Such fractures could interconnect at bedding planes or other discontinuities and allow fracture fluid access to them, or they could forever remain separated and have only a small effect on the gross-fracture mass balance. However, this mechanism would only explain multiple fractures associated with height growth and would not explain the 11 fractures observed in the B sand (where there was only lateral growth within the sand to reach the intersection point).

For lateral growth within the sandstone, it is instructive to examine the stress field around the fracture tip to determine if any associations can be made between stress calculations and the observed results. To do this, the Green and Sneddon solution[18] for a 3-D, flat elliptic crack was used to calculate the stresses around the crack tip, which were then contoured to show the distance at which given stress levels were observed. Figure 4 shows one such calculation of a representative M-Site fracture having a wing length of 300 ft, height of 100 ft, net pressure of 1000 psi, Poisson's ratio of 0.2 and Young's modulus of 4.57e+06 psi. Contour levels of 200, 400, 600, 800 and 1000 psi tensile stress are shown. The crack tip is at the (0,300) coordinate.

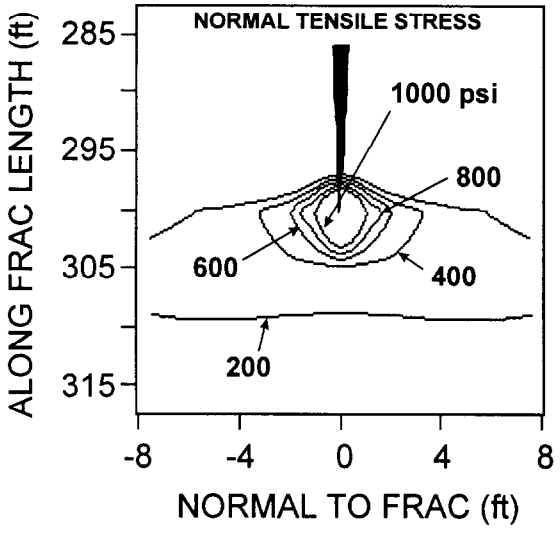

Figure 4. Contours of tensile stress near crack tip.

In this example, the 1000 psi contour level, which is approximately the tensile strength of unfractured sandstones, is observed about 1 ft on either side of the fracture tip as well as ahead of it. This two-foot wide interval is approximately the same dimension as the zone of fractures seen on all of the cored fracture intervals. Significant, but lower, stress levels extend out several feet to the side and, although these would not be sufficient to break unfractured rock, they could be sufficient to open any pre-existing weakness plane. It is important to note that the size of this zone is dependent on the size and pressure within the fracture. Larger fractures will have wider high-stress zones and shorter fractures will have narrower high-stress zones.

This calculation suggests that a *scale-dependent* process zone could explain the genesis of multiple fractures. That is, as the fracture increases in dimensions, the zone of increased tensile stress widens. This process zone would never be observable in the lab because the fractures are too small to create a sufficiently wide tensile zone. Only in field tests with large fractures would the process zone extend far enough to generate separate fracture strands. This mechanism also suggests that multiple-fracture zones should widen as the fractures enlarge and individual fractures would not be expected to extend from the wellbore to the tip.

While this calculation suggests that stresses are sufficient to create multiple fractures in the near tip region, there remains the issue of connecting those fractures to the primary tip. This connection could be accomplished via pre-existing natural fractures, bedding planes and other features, as noted previously. Fractures that are not connected probably remain small and have only a limited role in the fracturing process. Fractures that do interconnect are pressurized and propagated, depending on the clamping forces due to the main fracture and fluid mechanics within the main fracture (i.e., formation of gel plugs, prop bridges, etc. would facilitate fracturing into these secondary strands).

Of more immediate importance to practitioners is the question of the relevance of multiple fractures to design models. Multiple fractures can have four separate effects on the fracturing process depending on their characteristics. These include:

- Excess Stored Volume (reduced length),
- Additional Leakoff Faces (reduced length, dehydration),
- Additional Viscous Pressure Drop (reduced length), and
- Enhanced Tip Resistance (reduced length)

All of these results are negative, as they serve to reduce the amount of fluid available for length penetration. These four characteristics should not be used arbitrarily as separate features in a simulator. If multiple fractures are interconnected, then there will be increased storage, increased leakoff and increased pressure drop. These should not be turned on and off independently. Only the tip effects may be somewhat independent of the others.

Unfortunately for modeling of this problem, it is not clear whether several similarly sized fractures are created or one dominant and several secondary strands are created. This problem must be understood before the pressure drop can be assessed, but it has little effect on storage or leakoff. The spacing of the multiple fractures may have an effect on the leakoff behavior. Closely spaced multiple fractures will exhibit high leakoff rates at first (since the leakoff volumes are independent at first), but will rapidly decline as the various leakoff regions begin to interfere with each other. Widely spaced strands may never interfere.

Finally, if multiple fractures are generated near the tip, they must have an effect on the tip mechanics. Any dilation associated with lateral multiple fractures will reduce the opening of the main fracture tip and require higher pressures to open the fracture. This behavior could be called dilatancy, as coined by Cleary. Similarly, if these lateral fractures undergo any shear movement, then they will never close entirely and will leave a residual asperity opening which essentially adds additional stress closing the fracture. It is expected that stresses from individual strands are additive and could be quite large if there are many fracture strands generated near the tip.

7.3 Secondary and T-Shaped Fractures

The 6-C injection exhibited a surprising amount of complexity, including likely secondary and T fractures, as observed by the microseismic imaging. The secondary fracturing started early in the treatment, at approximately 10

minutes, and at a net pressure near 1500 psi. The T fracture became evident with about 20 minutes left in the injection at a net pressure greater than 1800 psi.

It is worthwhile examining stress relationships to determine if the net pressures are consistent with expected stress relationships. Nolte and Smith[19] give the pressure to open vertical fissures from a long fracture as

$$P_{net} = \frac{\sigma_{H\max} - \sigma_{H\min}}{1-2\nu}, \qquad (1)$$

where σ_{Hmin} and σ_{Hmax} are the principal horizontal stresses and ν is Poisson's ratio. Based on stress measurements at greater depths,[20] it is likely that the horizontal stress difference in the C sand is about 800 psi. Using Eq. 1, the net pressure at which secondary fractures open would be about 1300 psi, which is very close to observed level. Once open, however, the mechanics change and the extension pressure of a long secondary fracture will be a function of the normal stress on that fracture plane.

The T fracture occurs near the end of the treatment when the pressure is approximately 4900 psi, which is 300 psi above the calculated overburden stress. It is a reasonable expectation that horizontal T fractures will form and propagate when the fracturing pressures are elevated above the overburden stress level, as seen here.

A visual examination of pressure data from the 6-C fracture (e.g., see section 8.3.2) would not show any indication of unusual or complex behavior, nor would any model history match of the pressure, as these usually attempt to match the pressure at shut in and seldom match exactly with observed pressures during the full extent of the treatment. Gulrajani,[21] however, has analyzed the injection data and has found that the pressure-derivative diagnostic plot indicates that a significant change in the behavior of the fracture occurred at about the time at which horizontal fracturing began. Figure 5 shows an injection derivative plot[22] for this test which indicates that non-ideal behavior occurred throughout most of the treatment (flat derivative curve), as well as at the time of T fracturing when there was a significant change in the derivative. This example is a reminder that these diagnostic plots have value even if model history matches are being performed.

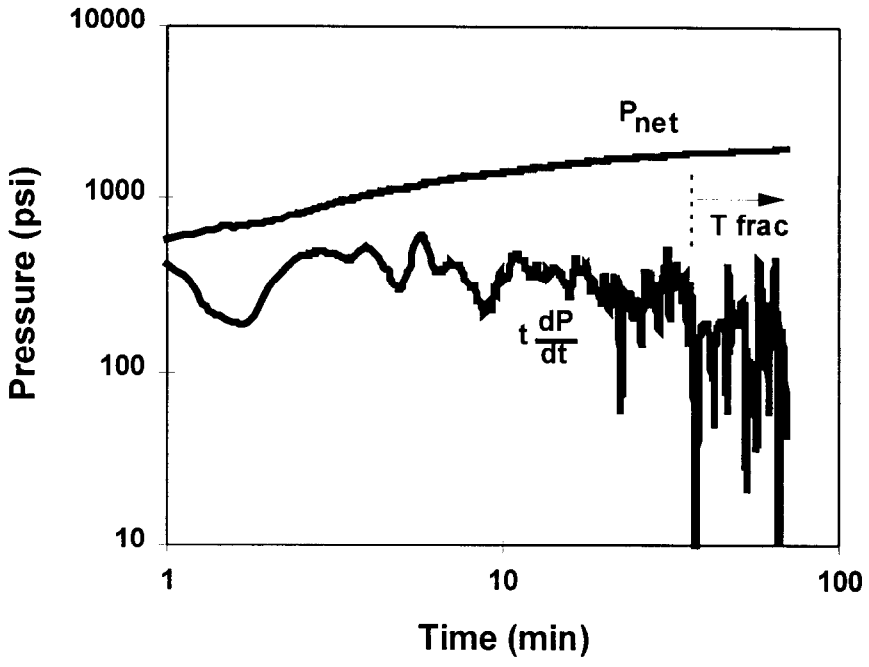

Figure 5. Diagnostic plot of 6C injection.

7.4 Large Pressure Drops

The M-Site experiments provided the unique opportunity to measure the pressure at a location within the hydraulic fracture as well as at the wellbore. However, these measurements were only made in the 4-C, 5-C and 6-C injections, after a clear connection between the fracture and the wellbore had been achieved. Given the two pressure measurements, it was possible to determine the pressure drops in the fractures at various times. Examples of these pressure drop magnitudes are:

	Mid-Frac	Shut-In	1 Hr Post-Shut-In
4-C	400 psi	100 psi	250 psi
5-C	1600 psi	1000 psi	600 psi
6-C	1500 psi	1000 psi	500 psi

These results initially appear to be very large, although some of the "Mid-Frac" data also have a sizable perforation pressure drop included.

It is difficult to attempt any detailed evaluation of tests 4-C and 6-C because of the complexity of their growth (4-C was highly asymmetric and 6-C had complex fracturing), but test 5-C is an ideal candidate, having very symmetric growth, both in height and length, and no operational difficulties or observed complexity. Several simulations of the 5-C experiment were conducted to evaluate the pressure-drop results.

To perform this analysis independent of any particular commercial simulator, a simple, finite-difference, PKN type simulator[23] was used in a quasi-constant-height mode. The quasi-constant-height mode uses the stress distribution to provide the correct width distribution, but fracture height is kept constant (except in the tip region) to mimic the observed behavior of the 5-C injection, which had limited height growth. There were absolutely no variable knobs used in the base-case simulations. However, several separate simulations using a tip overpressure to simulate various tip effects were performed, as were several simulations using an increased viscous resistance by employing a factor multiplying the viscosity. Results from these three types of models were then compared with the measured data.

Figure 6 shows the net pressure for three example simulations, including a base case (no knobs), a tip case, and a resistance case. Relevant parameters for these runs are

$n'=0.4$,
$k' = 0.2$ lb-sec$^{n'}$/ft^2,
leakoff coefficient = 0.001 ft/$\sqrt{}$min,
spurt = 0.01 gal/100 ft^2,
a leakoff height of 76 ft,
Young's modulus = 4.57e+06 psi, and
Poisson's ratio = 0.2.

Since there is an approximately 200 psi perforation pressure drop seen at shut in, it can be seen in Figure 6 that the base case (as well as all others) overshoot the measured net pressures if the fracture height is known and stipulated. In reality, most of the models would have predicted much more height and therefore would have had considerably lower net pressures. Fracture lengths for all three cases are about 420-480 ft, approximately the same as imaged (this is one of the few injections where modeled and measured lengths were similar).,

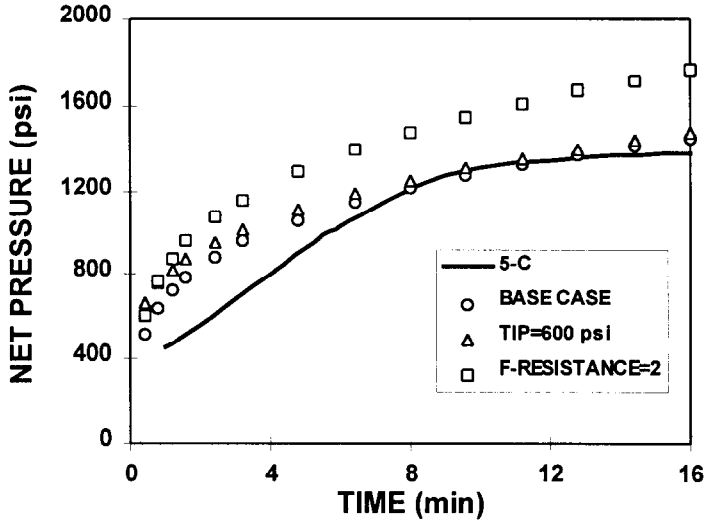

Figure 6. Simulation results for 5-C injection.

Of more importance here, however, is the pressure drop developed between the wellbore and a point 300 ft into the fracture. The calculated pressure drops at shut in (the most accurate point since there is no perforation pressure drop) are:

base case:	454 psi
tip overpressure=600 psi:	430 psi
resistance factor=2	689 psi

In all cases, the calculated pressure drops are not nearly as large as the measured drop for 5-C. Increasing the tip overpressure decreases the pressure drop while only slightly increasing the net pressure (up to the point where the tip overpressure exceeds the base net pressure). Increasing the flow resistance factor will significantly increase the pressure drop, but it also increases the net pressure to levels inconsistent with those measured. A shorter fracture length, which would require a greater pressure drop over the first 300 ft, would provide a possible solution, but if the imaging length data are believed (and these data are corroborated by the timing of the intersection pressure data), then a short fracture cannot be the explanation.

One possible solution is the development of a large tip zone with little pressure drop, which would only occur if there was little fluid movement in that zone. Such a process zone would need to be at least 50-100 ft long to match both the microseismic lengths and the measured pressure drops. Under this scenario, injection 4-C has a small pressure drop at shut in because the 625-ft wing length puts the "tip zone" far past the intersection well, whereas the 5-C and 6-C injections, with their 450-475 ft wings, have tip regions which reach back close to the intersection point. The size of this zone seems too large to be realistic, but it may be affected by the previous fractures in this interval.

It is also likely that the sand in injection 6-C had a significant effect on the resultant pressure drops and overall net pressures. Both 6-C and 7-B, the two sand fractures, achieved net pressures of 2000 psi, much higher than would be expected. Much of the increased net pressure could be a result of sand bridging to minimize height growth and increase net pressures.[25]

7.5 Fluid System Effects on Fracture Growth

Comparisons of the geometries relative to the pump parameters of various tests shows that there is a strong influence of the fluid system (rheology, leakoff, etc.) on the shape of the fractures. Prior to evaluating the differences between systems, it is first necessary to compare some similar fluid-system tests in order to evaluate the

accuracy of any comparisons. For example, injections 5-B and 6-B were pumped identically using a 40#-linear-gel system and yielded the following comparison:

	Lengths	Height
5-B	250/375 ft	80 ft
6-B	300/400 ft	75 ft

Similarly, a comparison of injection 5-C at shut in with injection 6-C after 480 bbl should be similar, as they both used the same cross-linked fluid. Their comparison is given below:

	Lengths	Height
5-C (Shut in)	400/400 ft	140 ft
6-C (480 bbl)	325/375 ft	125 ft

There, thus appears to be about a 10-15% uncertainty between any size-characteristic comparisons. Any differences greater than this amount are likely to be statistically significant.

The best direct comparison between different fluid systems occurs in injections 1-C and 2-C. At shut in (95 bbl), injection 1-C has a symmetric length of 125 ft and about 15 ft of upward height growth using a 40# cross-linked borate system. At 95 bbl, injection 2-C (40# linear gel) has no height growth and a length of 250 ft, even though there was a six minute shut-in period after 66 bbl, during which time leakoff continues to occur. This comparison is summarized below:

	Lengths	Height
1-C (X-link)	125/125 ft	95 ft
2-C (linear)	250/250 ft	80 ft

A reverse comparison can be made by comparing injections 3-C (40#-linear gel) and 5-C (40#-cross-linked gel). Both injections achieved the same lengths even though injection 5-C has 28% higher rate (less leakoff) and nearly double the volume. Injection 5-C did have somewhat greater height growth into the bounding shales. This comparison is given below:

	Lengths	Rate	Volume
3-C (linear)	425/475	22 bpm	247 bbl
5-C (X-link)	450/475	30 bpm	480 bbl

These two examples show that there is a significant difference (approximately a factor of 2) in the fracturing results obtained with linear gels compared to cross-linked gels. Whether due to viscosity, elasticity, effects of the fluid system on the fracture process or other mechanisms, it is clear that penetration rates and height containment are much better with non-cross-linked systems. It is this effect which was first described as rapid lateral extension in early M-Site publications. As noted here, it appears to occur only in the thinner fluid systems, which are much more efficient at developing fracture length.

7.6 Discrepancies in Fracture Volume

While a few of these injections appear to have imaged sizes similar to that which would be predicted from models (e.g., 5-C), the majority of them have much smaller imaged sizes than predicted. This discrepancy is not obvious in most of the modeling work that has been performed to date because the modelers have been tasked to try to match the imaged size and have invoked additional mechanisms (e.g., multiple fractures) to achieve that objective. For the purposes of this paper, numerous model calculations have been performed to match the net pressure with minimal *ad hoc* mechanisms. The simulations have helped to show the differences and to justify the imposition of additional mechanisms.

Injections 5-B and 6-B are good model candidates because they are relatively simple fluid systems with no unusual

behavior from the image data. The both also have nearly constant height, so the quasi-constant-height approach described earlier can be applied, thus further reducing model variability factors. Using an n'=0.56 and a k'=0.006 lb-sec$^{n'}$/ft^2 for the linear gel, with all other parameters the same as noted previously, the modeled dimensions for three simulations compared to the imaged results are shown in Figure 7. The three simulations include

- a base case which does not attempt to correctly match the net pressure
- a case with increased viscous resistance (using a numerical factor=6), and
- a case with increased tip overpressures (1200 psi).

The last two cases were designed to match the net pressure of the treatment at shut in. The leakoff coefficient (0.001 ft/√min) was chosen to yield an approximately 50-60% efficiency at shut in, a typical number for these reservoirs based on numerous shut-in tests. It is clear in Figure 7 that simply matching the net pressure does not result in a fracture size that matches the imaged size.

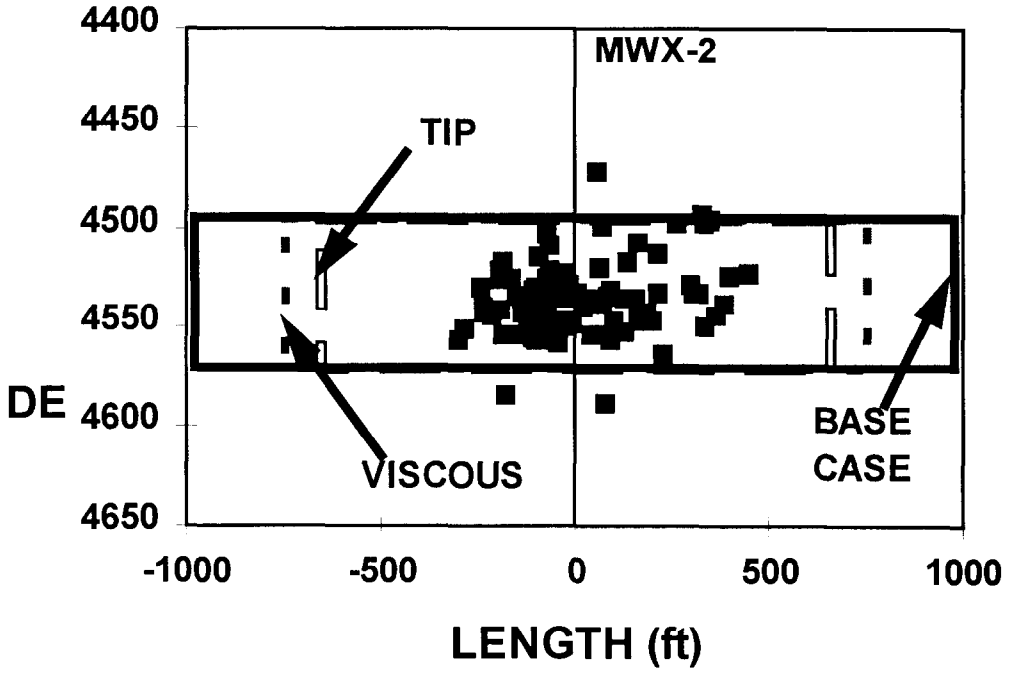

Figure 7. Comparison of modeled & imaged sizes: 5-B, 6-B.

Figure 8 shows a similar comparison for injection 6-C, except in this case the base-case calculation matches the net pressure closely and it is not necessary to invoke other mechanisms (other than stipulating the quasi-constant-height value of 190 ft) to elevate the pressure. For this case, n'=0.4 and k' = 0.2 lb-sec$^{n'}$/ft^2. As would be expected, given the complexity observed in injection 6-C, the modeled size is not even close to the imaged size, with the explanation being the obvious loss of fluid into the secondary and T fractures. Nevertheless, the comparison is still valid as it shows the discrepancies that develop for any number of reasons.

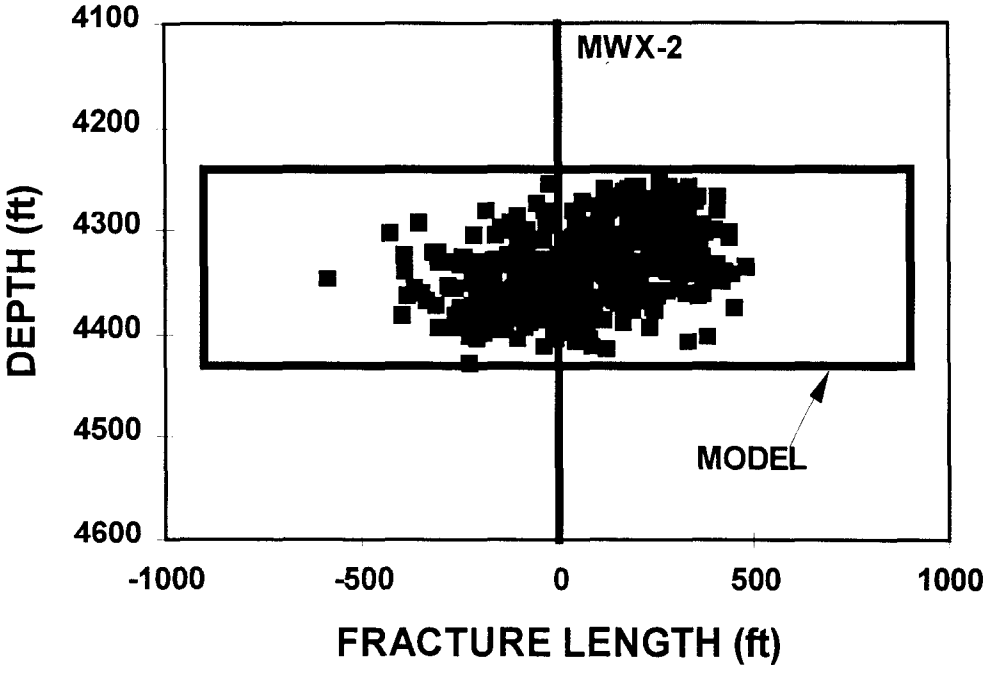

Figure 8. Comparison of modeled and imaged sizes-6-C.

These discrepancies indicate that additional fluid is being stored in the fracture or lost into the formation, but not in such a way that it is obvious during shut-in periods where the base leakoff coefficient is evaluated. Possible explanations include storage in multiple fractures, enhanced width (e.g., from a lower compliance factor such as modulus), or pressure-dependent fluid loss such as fissure opening. The fissure opening appears to be a likely possibility for all of the tests because of the apparent secondary fractures observed from microseismic images during injections 4-C and 6-C and from previous history in deeper reservoirs.[23] However, the presence of multiple fractures in the intersecting wellbores lends credence to the storage hypothesis. At this time it is impossible to distinguish between all of the possibilities, but it is important to stress that there are operative mechanisms associated with these treatments which would not normally be recognized without the fracture diagnostics.

8.0 M-SITE EXPERIMENT

Three of the primary goals of GRI's Stimulation and Completion program are (1) validation of hydraulic-fracture design models, (2) development of hydraulic-fracture length diagnostics, and (3) validation of all fracture-diagnostic technology. Validation implies a confirmation of the predicted results by actual measurement in the field, and thus requires an instrumented facility where fracture behavior can be measured. The effort to develop such a capability is named the M-Site Experiments. Sandia has been involved (along with CER Corp., Branagan & Assoc. and RES) in the development and testing at M-Site.

The M-Site location is in the Piceance basin near the town of Rifle, CO, in Mesaverde sandstones at depths from 4000-5000 ft. During the fall of 1992, a site suitability test was conducted, from which highly positive results were obtained. During 1993, the first of several experiments was conducted in the A sand, and planning for a new monitor well was initiated. During 1994, the monitor well was drilled and instrumentation installed. Work in the B sandstone began in 1995, during which time seven injections were conducted. Work in the C sandstone was completed during 1996. Analysis of the final two injections was completed in 1997.

8.1 C-Sandstone Background

C sandstone experiments were conducted during the July 1996 to December 1996 time frame, after which the site was permanently shut down. The C sandstone experiments were considerably different from the B sandstone tests in that the intersection well was drilled prior to fracturing to provide data on both time of intersection and type of intersection. The objectives of the C sandstone experiments were

- Validate fracture length from microseisms using the intersection well to provide time of arrival information (by monitoring the pressure) which could be directly correlated with the microseisms at that time.
- Validate microseismic azimuth by providing a direct measurement of the intersection location.
- Provide modeling validation on fracture length in the same manner as the microseismic comparison.
- Provide information on mechanisms by measuring intersection well pressures and imaging the fractures created in the intersection well.
- Provide inclinometer information on fracture deformation to validate both models and microseisms and to give other useful information on closure, prop distribution, residual deformation and other features.

8.2 Layout of C sandstone wells

The C sandstone lateral well was drilled during July of 1996. A plan view of the intersection is shown in Figure 9, while the details of the intersection are shown in side view in Figure 10. The intersection well cuts through the expected fracture plane about 300 ft from the treatment well.

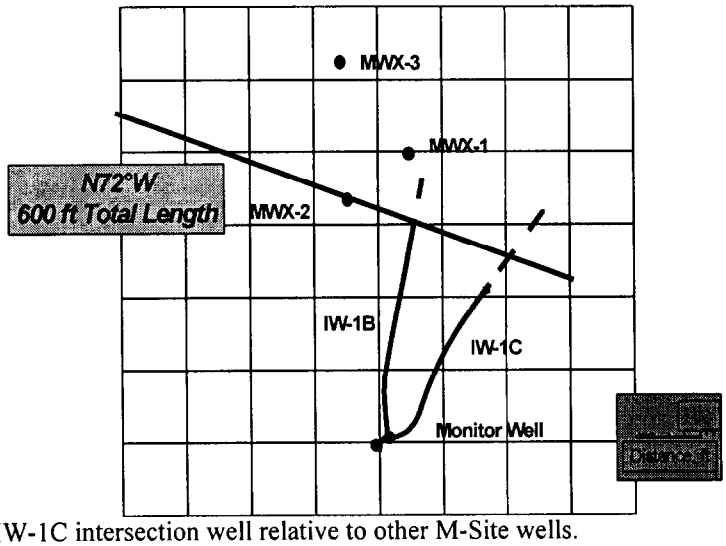

Figure 9. Plan view of IW-1C intersection well relative to other M-Site wells.

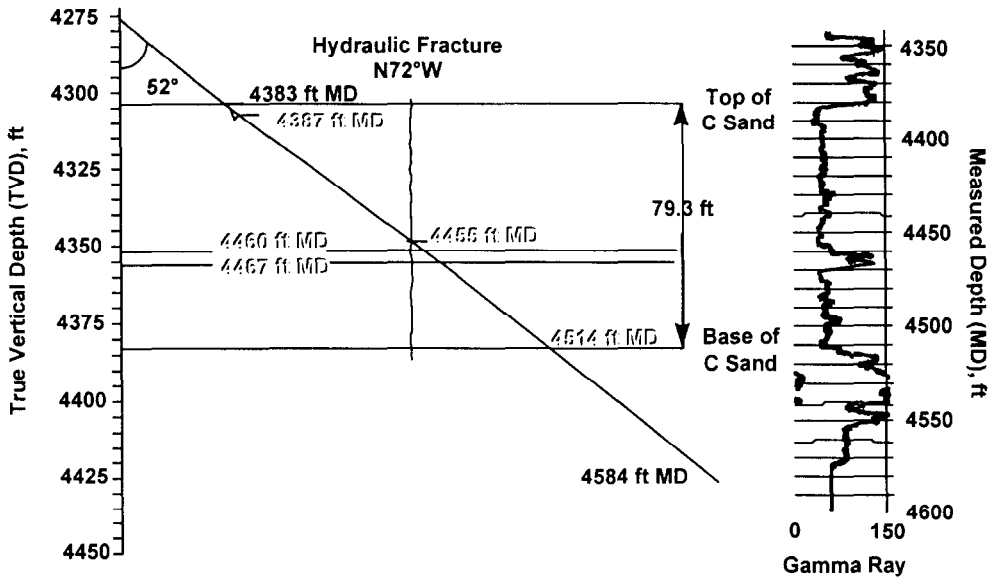

Figure 10. Side view of C-sandstone intersection of IW-1C.

8.3 C Sandstone Fracture Experiments

The C sandstone fracture experiments consisted of six injections conducted between August 1996 and December 1996, including a crosslinked gel breakdown, two linear gel minifracs, two crosslinked gel minifracs and a final propped treatment. Table 3 shows important details of these injections. The fifth column notes where the 5-level wireline seismic array was located, although it failed in the treatment well in fracture 4C. The sixth and seventh columns note whether a gamma ray or FMS log was run in the intersection well after the injection, and the last column notes the lack of pressure communication (NONE), a slow rise in pressure (RISE), or a clear connection in to the wellbore with an associated rapid pressure increase (CONNECT). Microseismic results for the first four of these tests were completed and reported in 1996. This report gives the results for injections 5C - 6C.

Table 3. Details of fracture injections

TEST	FLUID GEL TYPE	RATE (bpm)	VOLUME (bbl)	5-LEVEL	IW-1C TRACER	IW-1C FMS	IW-1C PRESSURE
1C	X-LINK	20	100	MWX-3	NO	NO	NONE
2C	LINEAR	22	136	MWX-3	YES	YES	RISE
3C	LINEAR	24	250	MWX-3	YES	NO	RISE
4C	X-LINK	40	950	MWX-2	YES	YES	CONNECT
5C	X-LINK	30	645	MWX-2	NO	NO	RISE
6C	X-LINK	30	1750	MWX-3	YES	YES	RISE

8.3.1 Injection 5C Microseismic Results

Injection 5C was designed to be a treatment-well diagnostic test, given that injection 4C had a failure of the treatment-well receiver system. The test was conducted on December 17, 1996 and consisted of 480 bbl of a 40-# cross-linked gel injected at 30 bpm. However, prior to the gel injection phase, the full volume of KCl water in the treatment well was injected at low

rates (1-3 bpm), followed by a short shut-in period. The cross-linked injection phase was started at 5 bpm and quickly stepped up to 30 bpm.

The injection pressure for this test is shown in Figure 11. Given a closure stress of approximately 3050 psi, the net pressure of this test reached approximately 1400 psi, well above any measured stress contrasts. It can also be seen that the leakoff rate is relatively high, given the fast pressure decline after shut in.

To obtain treatment well diagnostics, a four level receiver system was inserted into the treatment well, MWX-2. Other diagnostics included the receiver array in the monitor well, the tiltmeter array in the monitor well, the intersection-well pressure, and bottom-hole pressure.

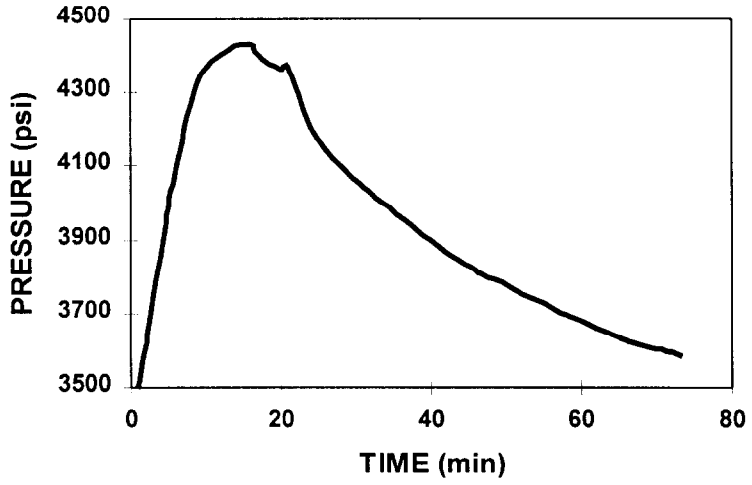

Figure 11. Pressure data from cross-linked-gel injection, test 5C.

The insertion of the multi-level receiver array into the treatment well required some modifications to the procedure. To minimize the placement of receivers in the perforated interval, only a four level system was placed in the treatment well, as a bridge plug was located at 4506 ft. This system was then oriented with perforation shots in MWX-3. Figure 12 shows a schematic of the treatment well aspect of this injection.

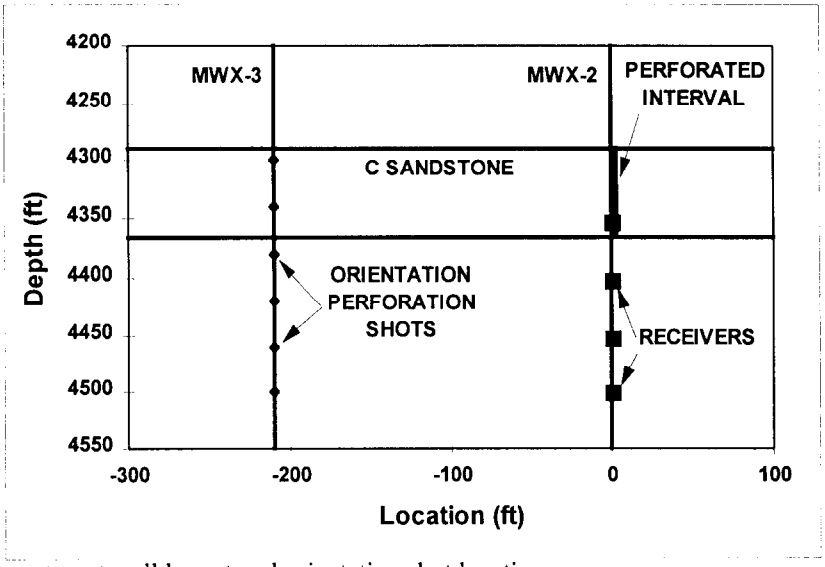

Figure 12 Schematic of treatment well layout and orientation shot locations.

An example of a perforation orientation shot at 4460 ft is shown in Figure 13. While p-wave arrivals are very clear, s waves are difficult to interpret. Since the purpose of these shots is to orient the receivers, the lack of s-waves is not important. This figure shows the traces from each receiver, top to bottom, all scaled to the largest amplitude (observed on level 4, y trace).

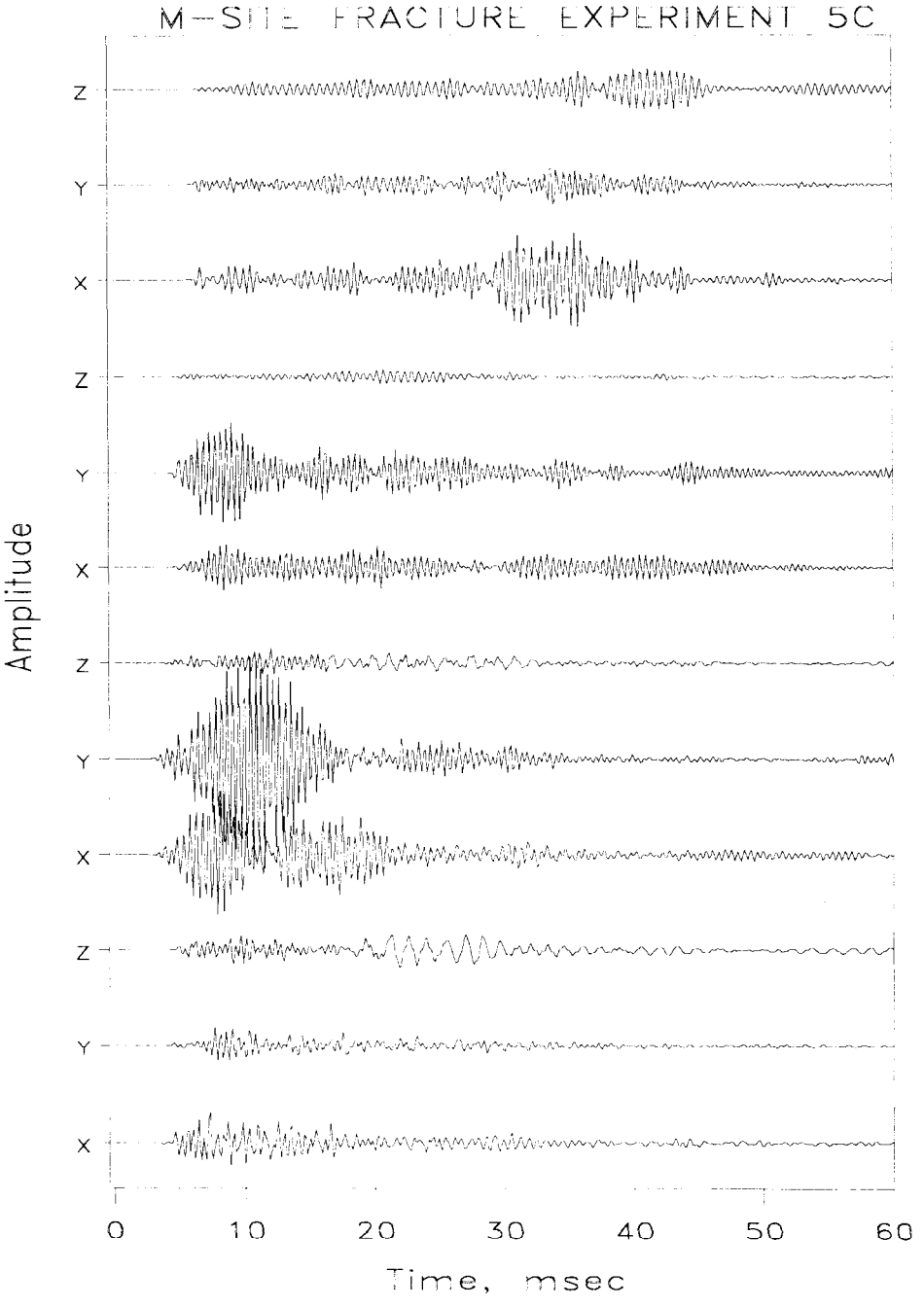

Figure 13 Example perforation orientation shot.

Figure 14 shows traces from the lowest level receiver for the perforation shot at 4460 ft. As noted previously, the p-wave arrival is clear but the s wave is difficult to discern. The hodogram plot for this perforation is shown in Figure 15. The p-wave particle motion for this example is very linear and gives an accurate reference orientation.

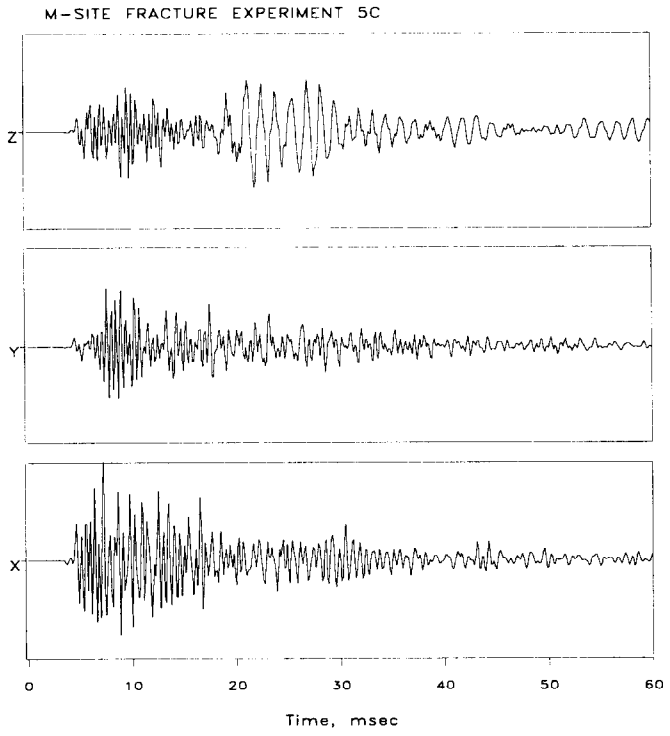

Figure 14 Example traces from perforation orientation shot, level 4.

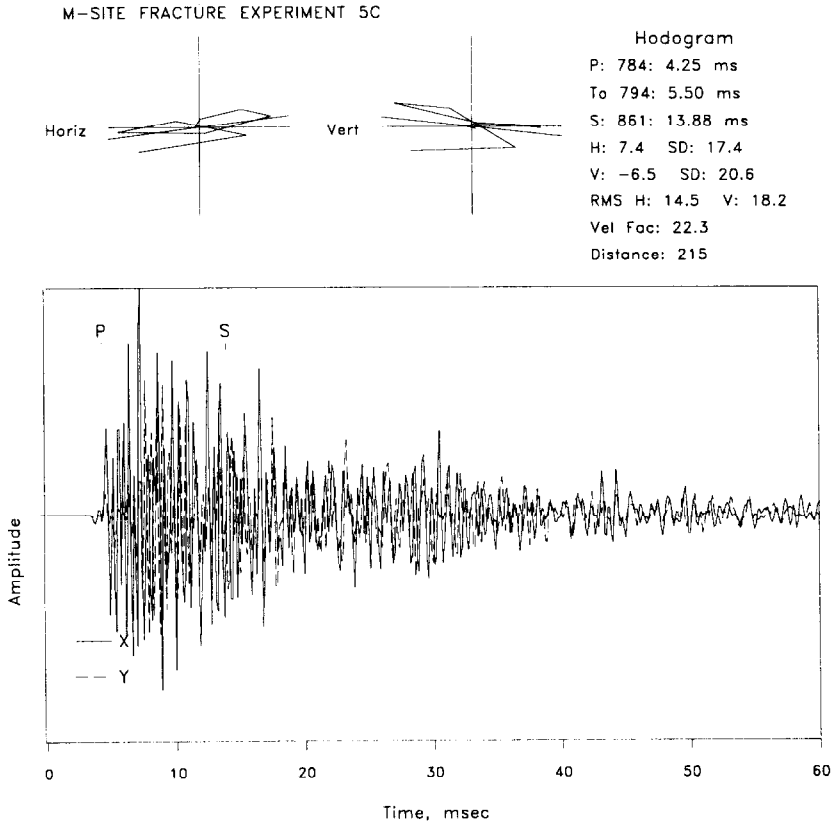

Figure 15 Example hodogram plot for perforation orientation shot, level 4.

The final orientation data for this test are shown in Figure 16. It can be seen that the orientation azimuths (direction of x axis to the perforation location) are very consistent and yield azimuths and standard deviations of -25.6° ± 5.1°, -84.2° ± 0.7°, -47.5° ± 1.5°, and 8.8° ± 2.2° for levels 1-4, respectively. Except for the topmost level, these results are sufficiently accurate to provide high-quality directionality.

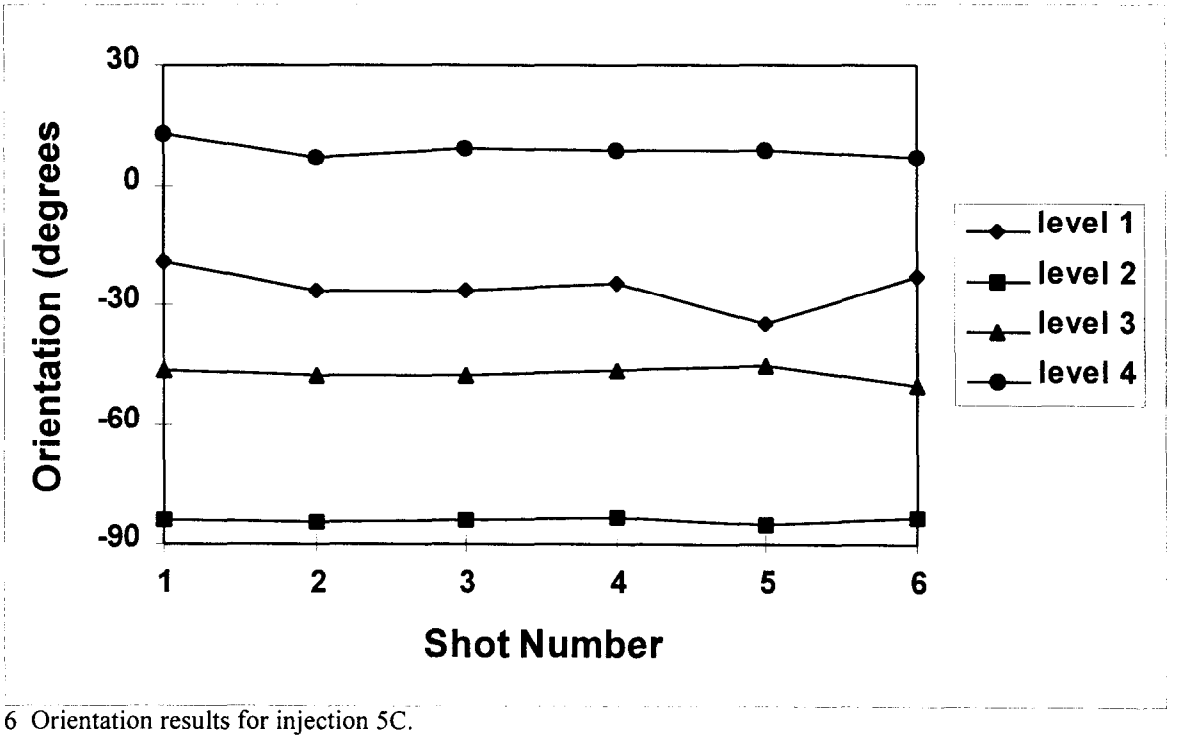

Figure 16 Orientation results for injection 5C.

During the monitoring of injection 5C, approximately 140 events were detected on the monitor-well receiver array, of which 91 were analyzable microseisms. Over 1000 various events were recorded on the 4-level system, but these are very complicated signals and final analysis of the 4-level data is not complete at the time of this report. Thus, all microseismic results presented here for the 5C injection are from the monitor-well array. However, examples of the treatment well events are shown later for reference.

Figure 17 shows example traces from one of the microseisms detected from the monitor-well array. This example has clear p-wave arrivals and relatively clear, but mostly small, s-wave arrivals.

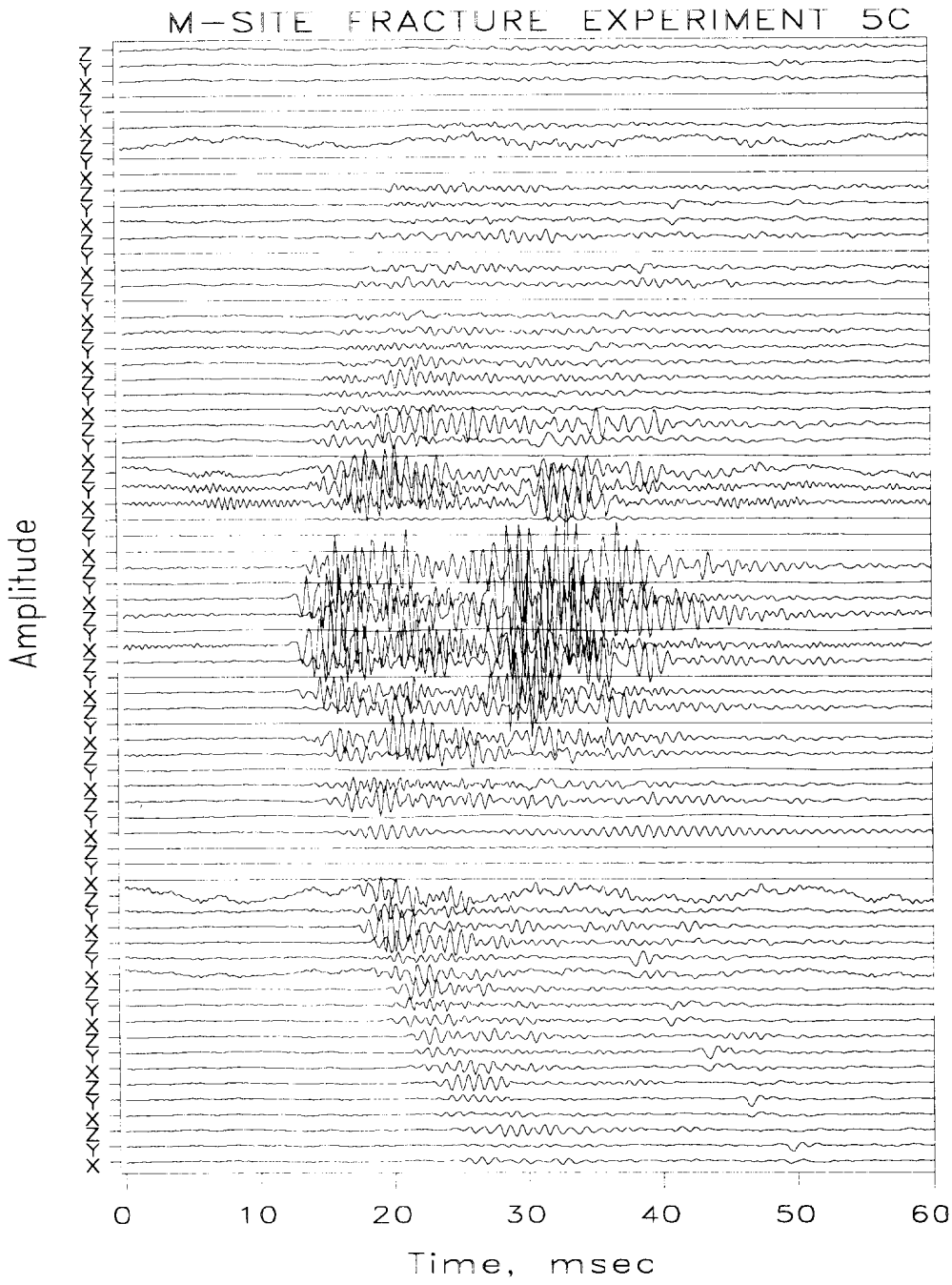

Figure 17 Example monitor well microseismic traces.

More details of the microseism can be seen in the expanded traces shown in Figure 18. This example is from level 27, situated at 4104 ft in the monitor well. This example is also considerably different than previous examples in that it shows a microseism with a smaller s wave, although its arrival is still clear. The hodogram plot for this example is shown in Figure 19. The horizontal hodogram shows a well-defined azimuth. The traces in the bottom part of the figure show p-waves that have horizontal components that are out of phase and s waves that are in phase. Frequency differences are also obvious. This microseism is located 380 ft from the treatment well on the east wing of the fracture near the bottom of the C sandstone.

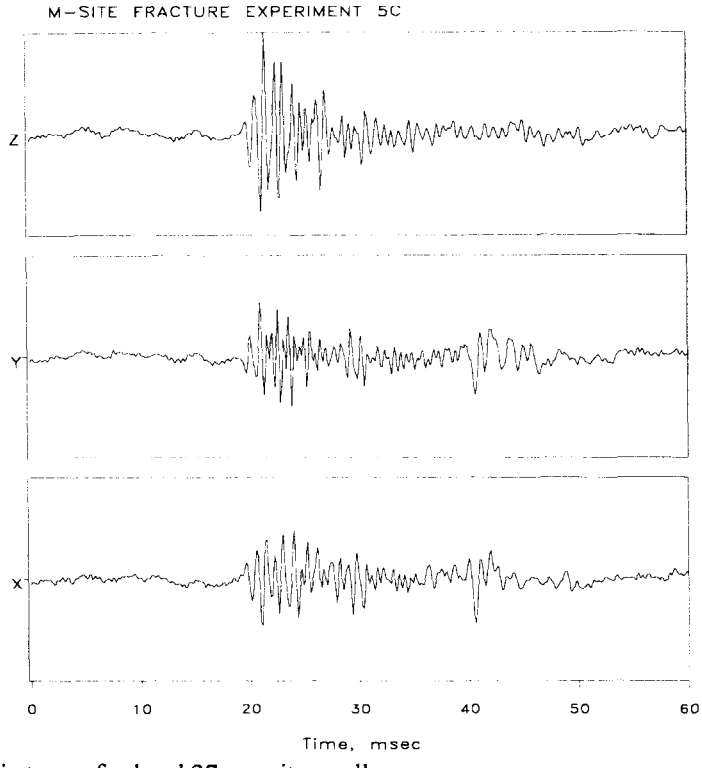

Figure 18 Example microseismic traces for level 27, monitor well.

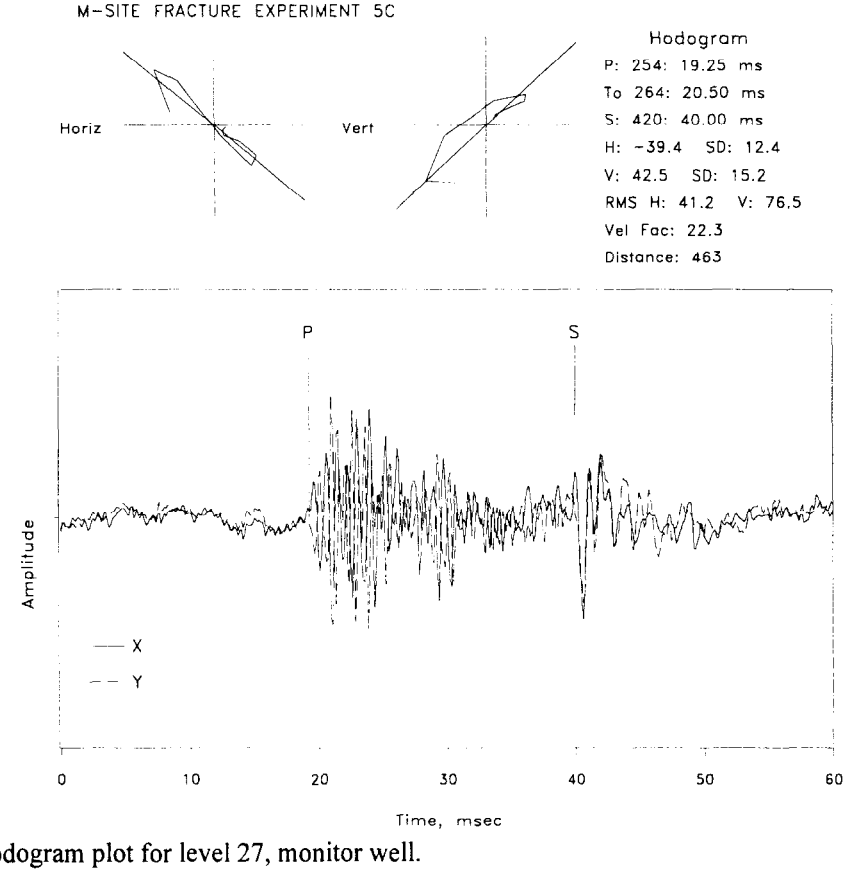

Figure 19 Example hodogram plot for level 27, monitor well.

The microseisms detected after 10 minutes of pumping are shown in plan view in Figure 20 and in profile view in Figure 21. These two plots illustrate a common and interesting phenomenon associated with microseism formation. While the initial one or two injections into a fracture often show a continuous growth of the fracture, later injections often have holes where no microseisms form or they form much later. This effect is thought to be similar to the Kaiser effect in acoustic emissions which essentially stipulates that once a weakness plane undergoes slippage, it will not occur again if the material is unloaded and then reloaded to the same stress. This behavior makes sense if the slippage is caused by asperity breakage and differential movement of the faces of the discontinuity (shear movement). However, microseisms can develop along the same plane at different locations or if greater loadings are imparted on the plane so that microseisms appear to occur in nearly similar locations on subsequent injections. On the other hand, it is also reasonable to expect that the slippage planes have finite length and after several slippages the plane eventually stabilizes (work hardening?) and no further microseisms can be generated on that plane for reasonable stress increases. The hole seen on the east side of the fracture in this injection (Figure 21) and similar "holes" seen in early injections are probably due to this mechanism.

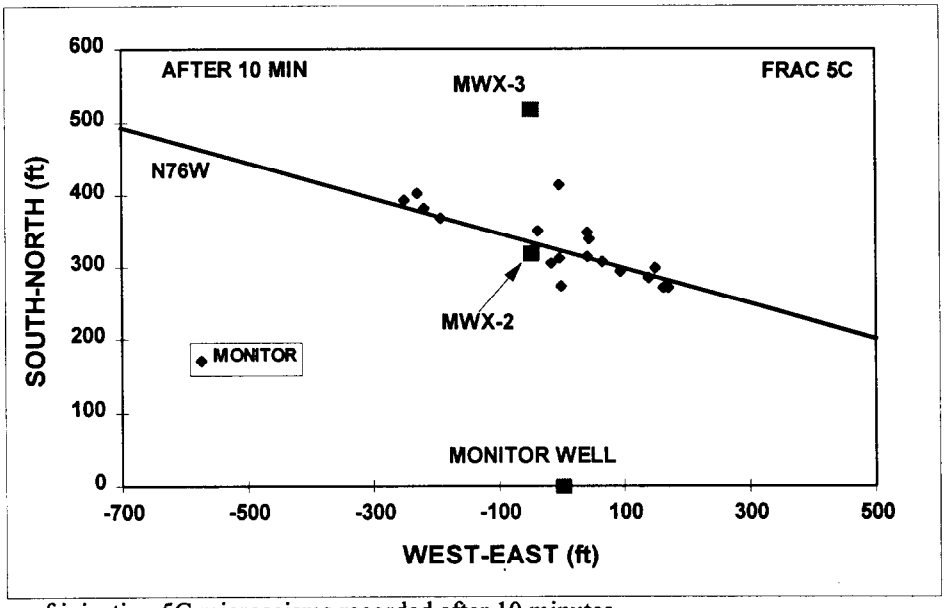

Figure 20 Plan view of injection 5C microseisms recorded after 10 minutes.

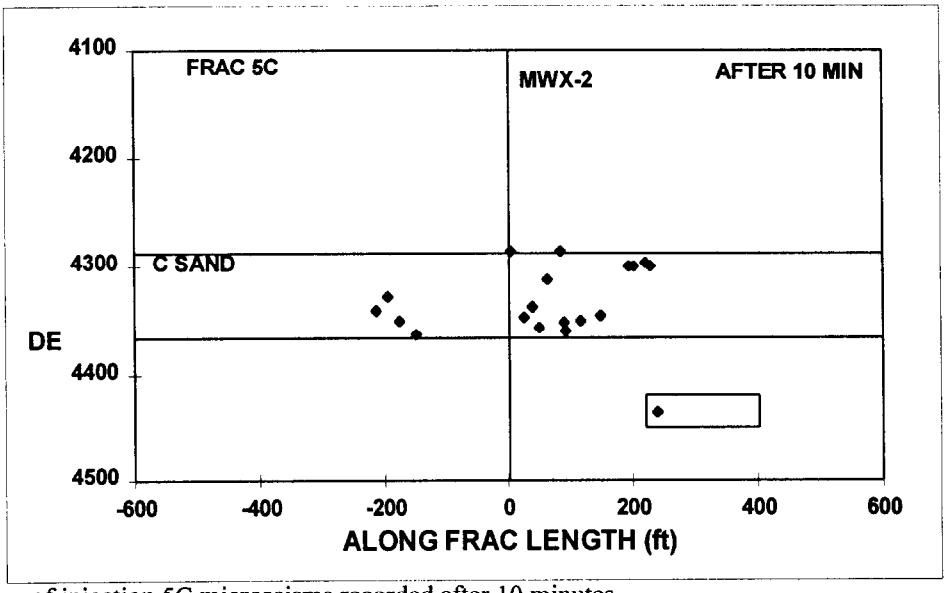

Figure 21 Side view of injection 5C microseisms recorded after 10 minutes.

Microseisms detected up to shut in (21 minutes after injection started) are shown in Figures 22 and 23. At this point the fracture is very symmetric with fracture lengths approaching 400 ft and height growth about 30 ft out of zone in both the upward and downward directions. In addition, some of the "holes" discussed previously have begun to fill in as more energy has been imparted into the system.

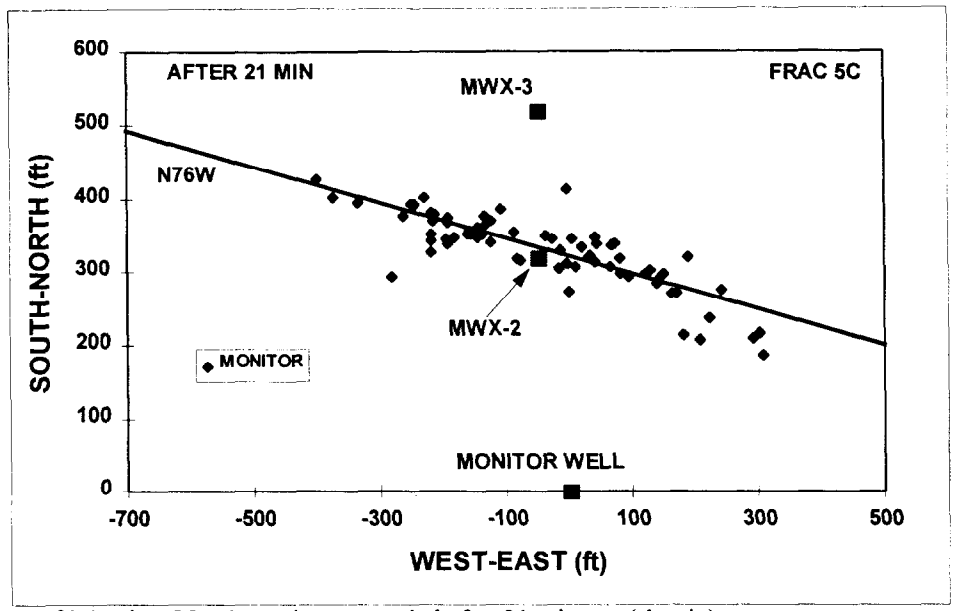

Figure 22 Plan view of injection 5C microseisms recorded after 21 minutes (shut in).

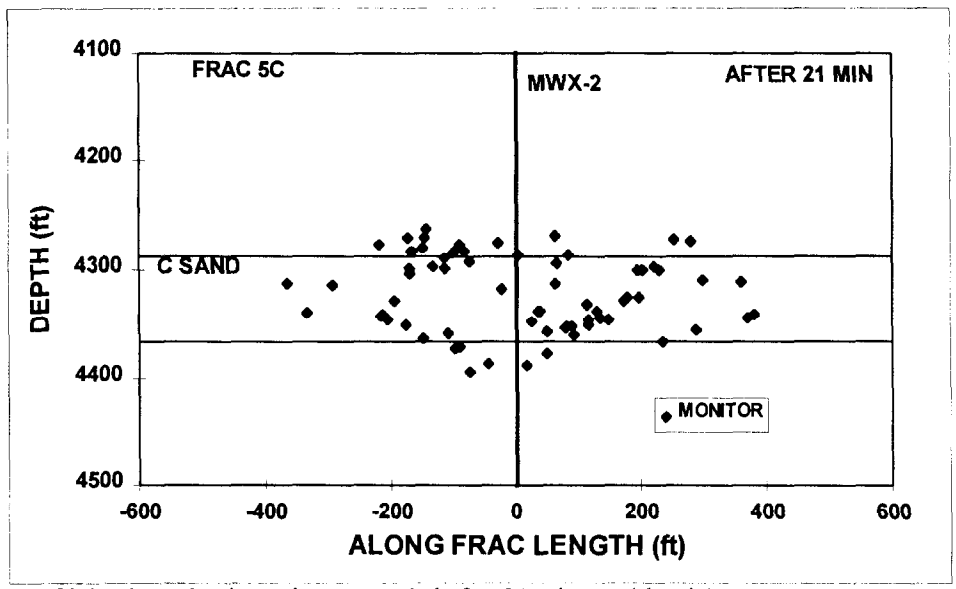

Figure 23 Side view of injection 5C microseisms recorded after 21 minutes (shut in).

All of the detected microseisms for this injection are shown in plan and profile views in Figures 24 and 25. The fracture has undergone an additional 75-100 ft of length growth with a final wing length of 450-475 ft on both sides of the fracture. Height growth has also remained symmetric, but no apparent height growth occurred after shut in.

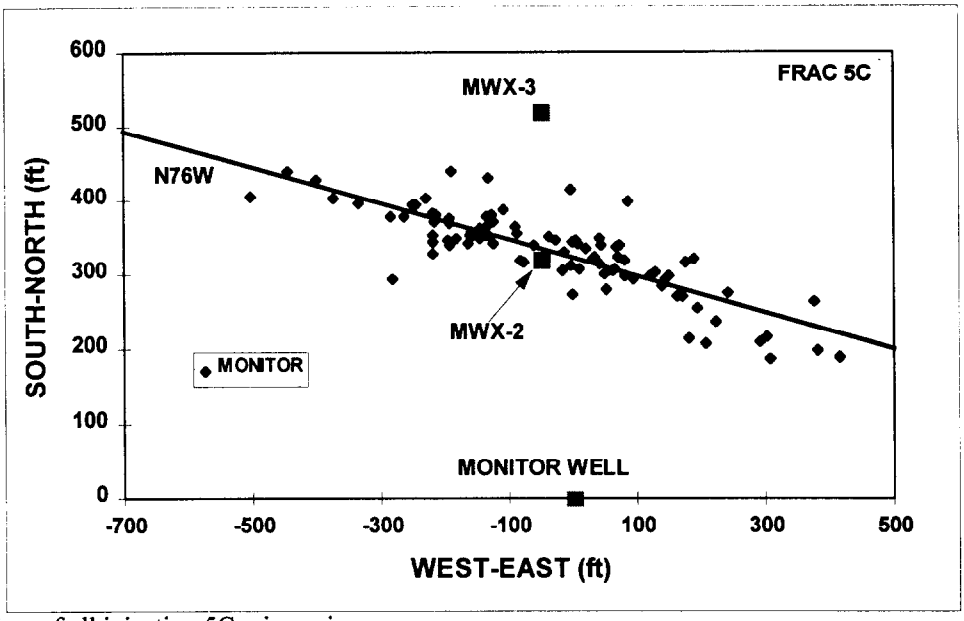

Figure 24 Plan view of all injection 5C microseisms.

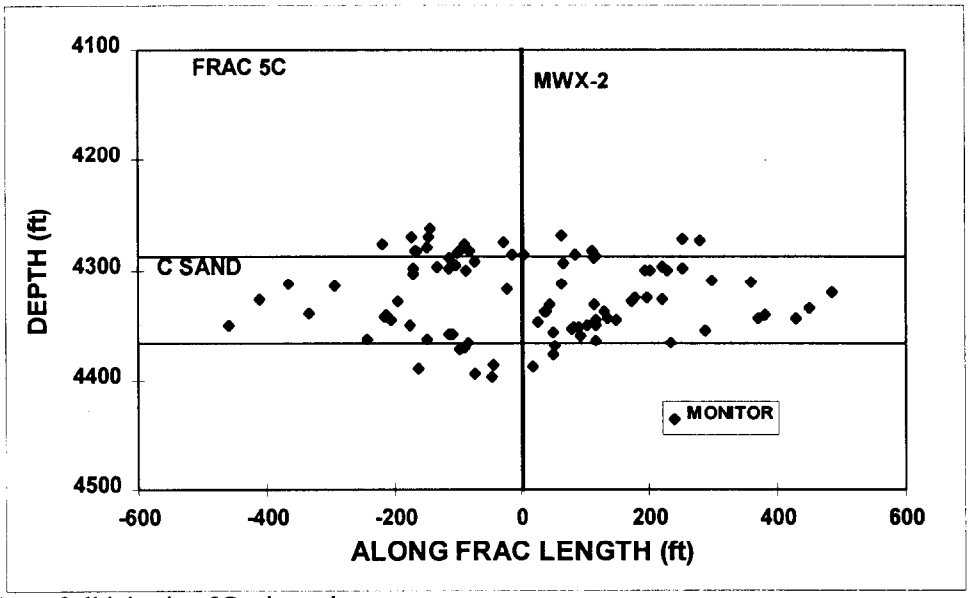

Figure 25 Side view of all injection 5C microseisms.

The recorded data from this injection show very simple fracture behavior compared to the that observed in Injection 4-C. This fracture is of interest because of its lack of complexity, in contrast to the previous test, and also because of the comparable length to the Injection 3-C, even though Injection 3-C employed only half of the fluid used in Injection 5-C. The primary difference between the two tests was the fluid rheology, although Injection 5-C was pumped at a somewhat higher rate.

Examples of the type of waveforms detected in the treatment well with the four-level array are shown in Figures 26 and 27. In the first example, the event is very large on the third level and small on other levels. The signal moveout is at tube wave velocities, suggesting that what is detected here is close to the wellbore or is highly perturbed by some wellbore mechanics.

The second example has more constant amplitude across the various levels, but also shows the tube-wave type moveout. Both examples, which were recorded after injection stopped, show large low-frequency waves on the vertical axes, probably induced by fluid movement. As noted earlier, most events observed in the treatment well are complicated and have not been fully analyzed at this time.

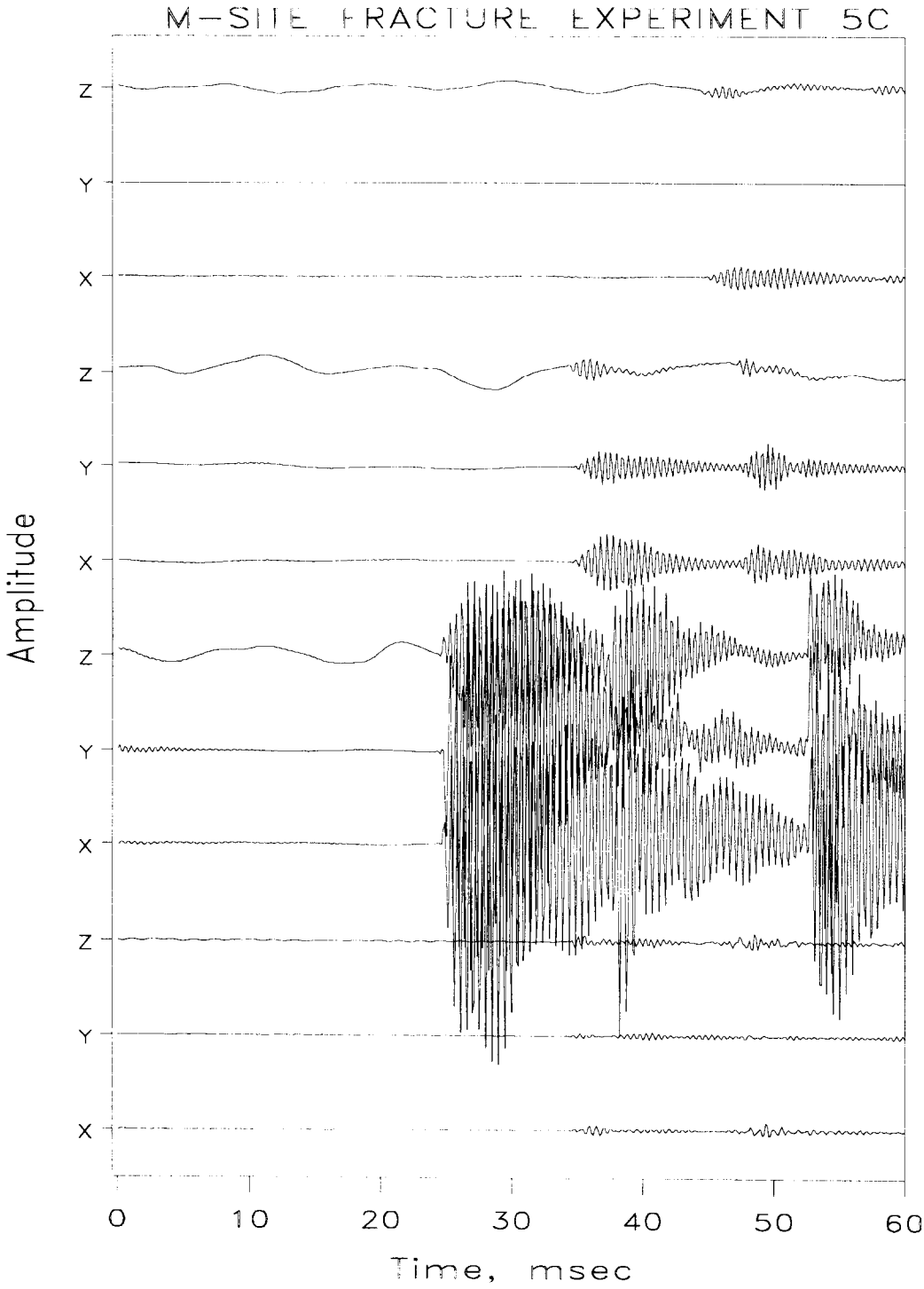

Figure 26 Example treatment well event.

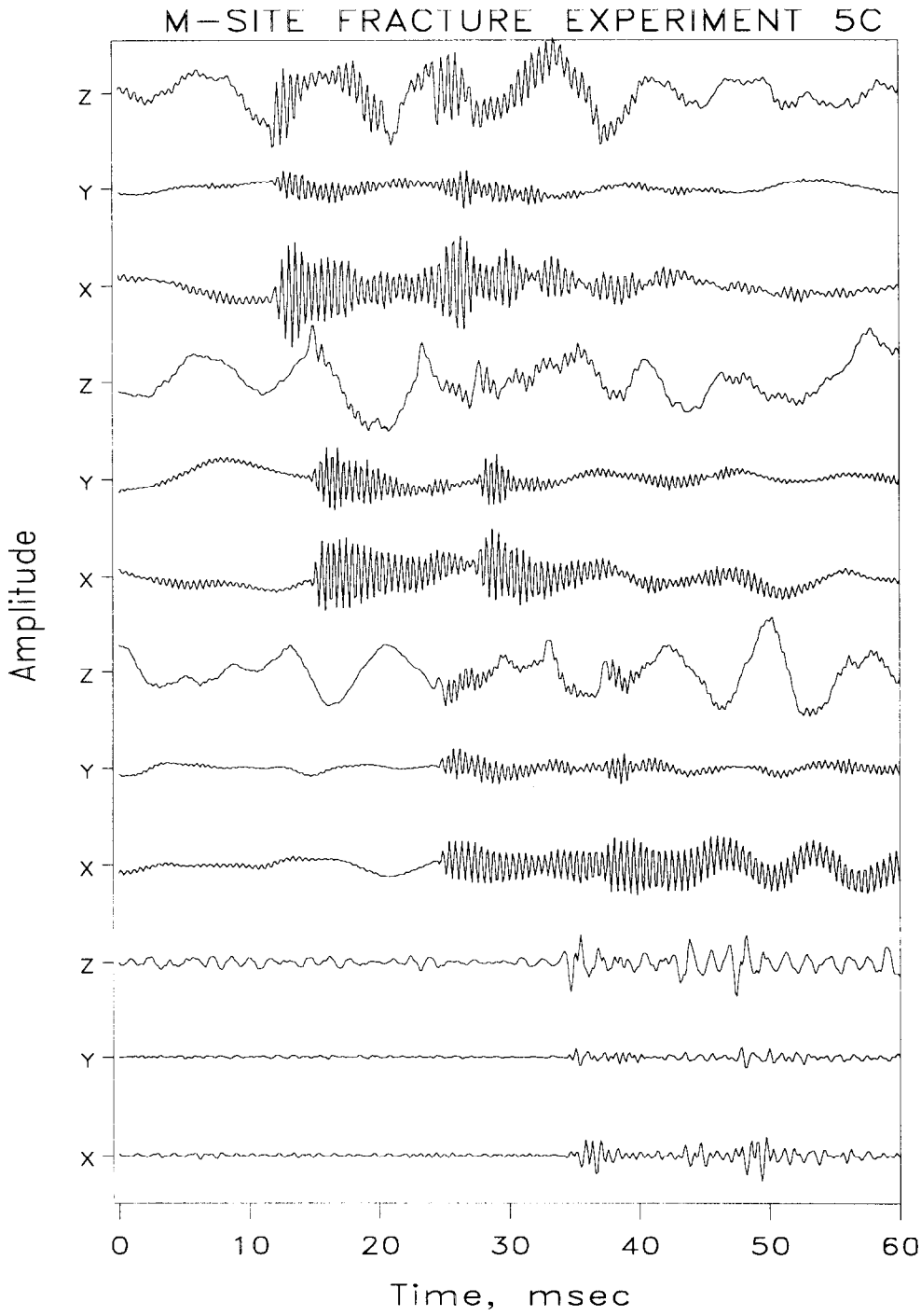

Figure 27 Example treatment well event.

8.3.2 Injection 6C Microseismic Results

Experiment 6C was a 2118-bbl injection of 250,000 lbs of proppant at 30 bpm. It was preceded by the injection of the wellbore load of 166 bbl at a rate of 20 bpm. The size of the treatment was designed to simulate a typical industry-sized treatment typical of this area. Although most treatments conducted by local operators are on the order of 750,000-1,000,000 lbs of proppant, they are usually into 3-4 intervals. Since this test was a single interval,

the appropriate scaling was made to arrive at the designed injection conditions. The proppant was divided into two stages:

3 ppg @ 185 bbls
5 ppg @ 800 bbls.

Figure 28 shows the injection pressure for this test. Important characteristics are the treatment pressures that exceed the maximum horizontal stress within a few minutes and exceed the overburden stress within 20 minutes.

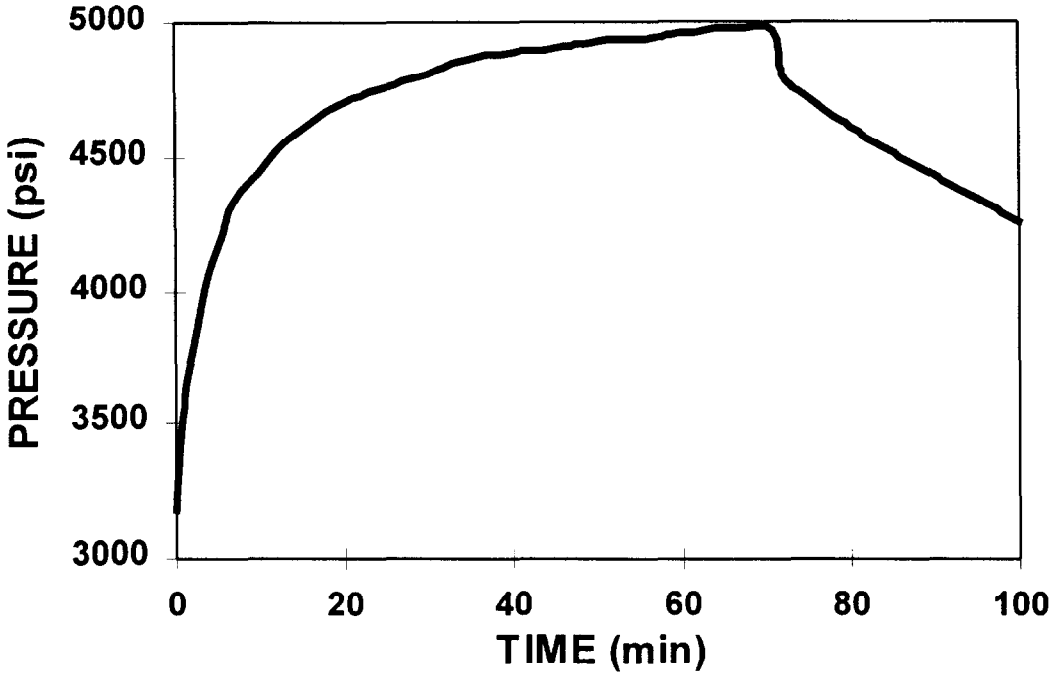

Figure 28. Pressure data from the cross-linked-gel stimulation, test 6C.

Injection 6C was designed to be a two-well monitoring experiment, with the 5-level system in MWX-3 and the usual monitor-well array. However, problems with the 5-level system limited the capability for full multi-level monitoring. During initial operation of the array, several levels started malfunctioning. Because of problems with the cold and with scheduling, there was no alternative but to continue with the injection regardless of the state of the 5-level system. Because of the malfunctions, most of the test was conducted with two operating receivers, at 4282 and 4380 ft, and the lower level often had problems with one of the horizontal axes. However, there were even some periods when the lower of these two levels suffered full communications problems and dropped off for short periods. The upper one always remained operable. The cause of this malfunction was eventually found to be in the fiber-optic cable head, where the connector for one of the downhole powers was etched due to water invasion. This etching reduced the size of the connector, causing significant voltage to be lost at the cable head. Tools began malfunctioning when the power level dropped too low.

Based on a two-level system, processing of the MWX-3 data required both p waves and s waves to be detected on both levels. Given four arrivals, accurate triangulation can be obtained. When the lower level was not adequately functioning and good microseisms were seen only on the top level, elevation data became uncertain and no attempt was made to determine the correct vertical positioning of the microseisms (it was assumed that these microseisms were located in the center of the C sand). However these microseisms still provided valuable plan-view data and are thus included in the data set.

Orientation of the single fully functional level was accomplished using perforation shots in the treatment well at depths ranging from 4220-4400 ft at 20 ft spacing. The configuration is shown in Figure 29.

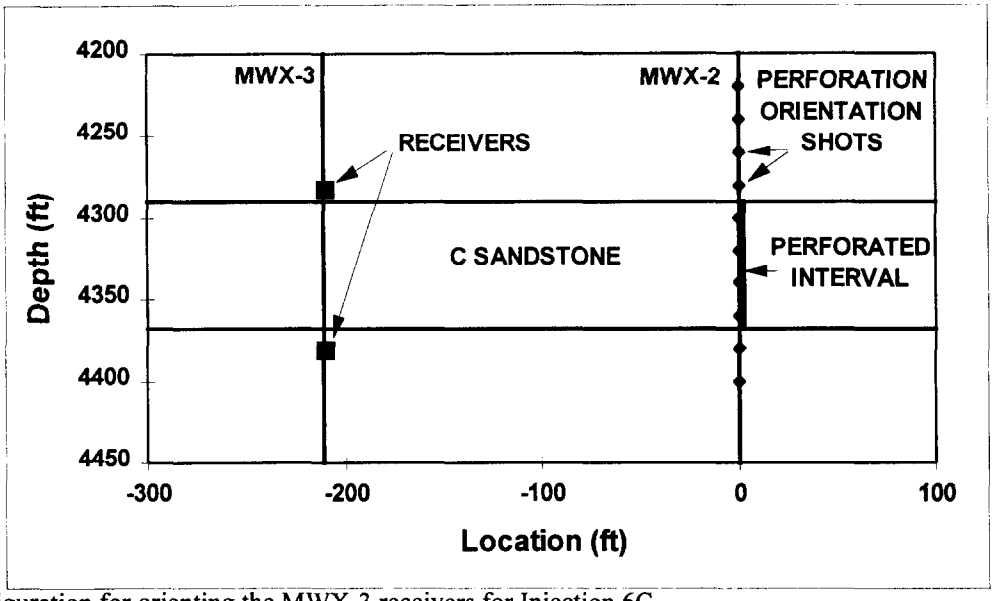

Figure 29 Configuration for orienting the MWX-3 receivers for Injection 6C.

Figure 30 shows example traces from the perforation shot at 4400 ft, as detected on the receiver at 4282 ft. As is typically seen in perforation shots at this site, the p-wave arrival is clear while the s wave is somewhat uncertain. Figure 31 shows a hodogram plot of this shot. The hodogram shows a linear particle motion at about a -67° orientation and a poorly resolved, if not questionable, s wave.

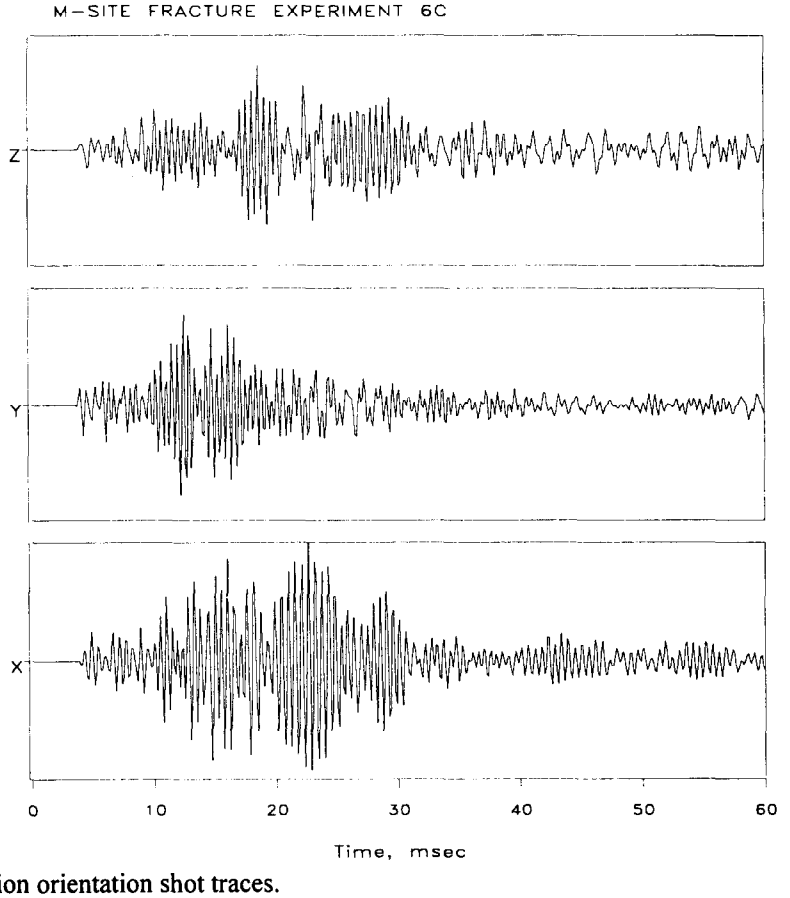

Figure 30 Example perforation orientation shot traces.

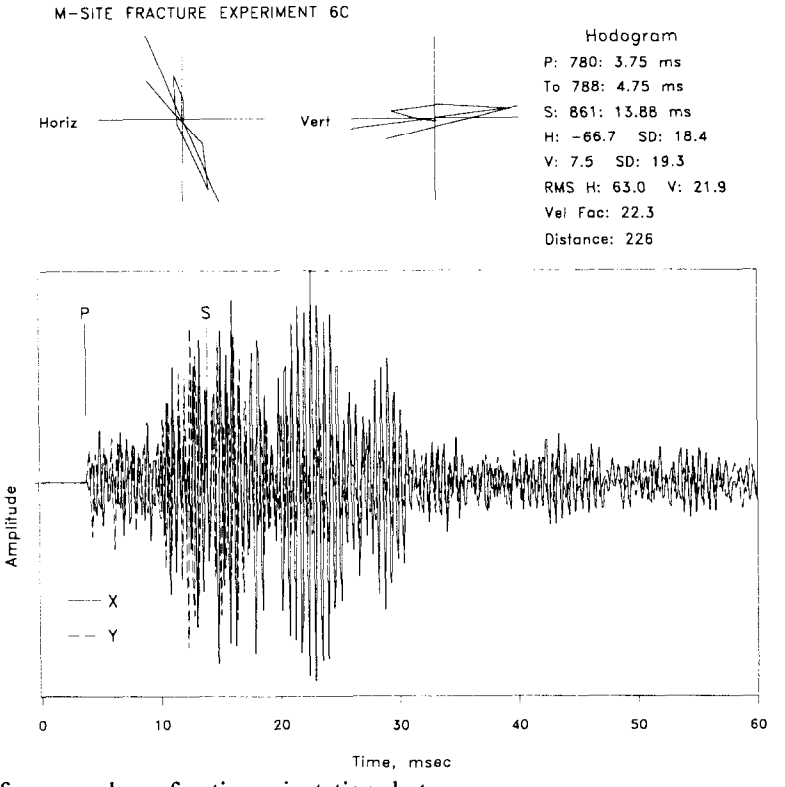

Figure 31 Hodogram plot for example perforation orientation shot.

The orientations for all perforation shots are shown in Figure 32. With the exception of two of the higher perforations, there is very good agreement for the receiver orientation with the x axis positioned at an angle of -69° relative to the treatment well.

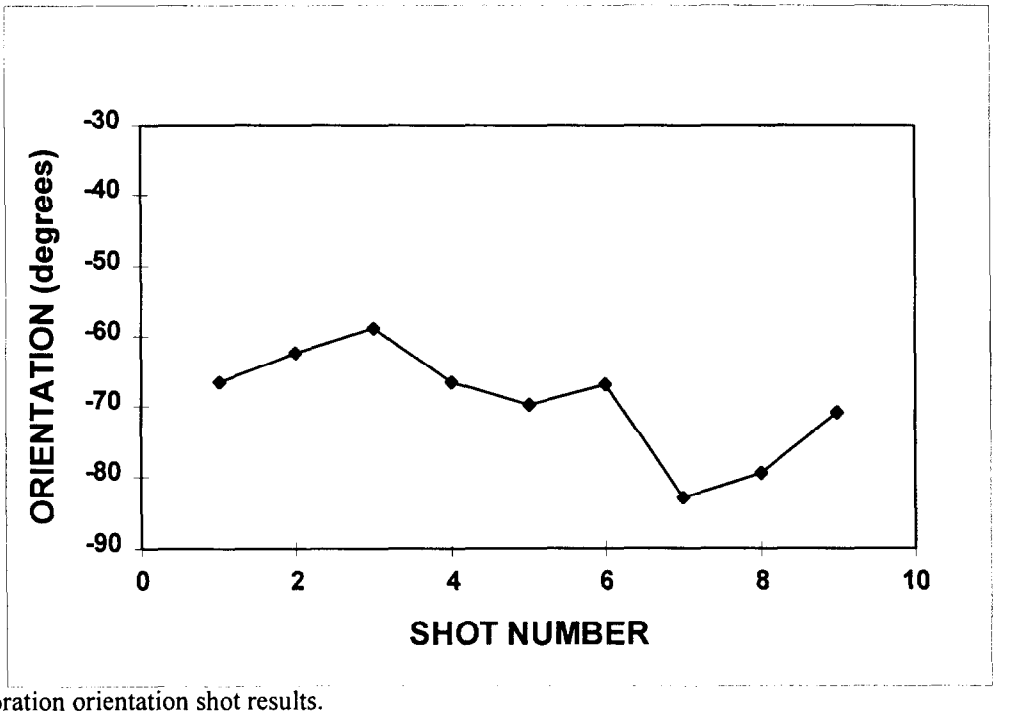

Figure 32 Perforation orientation shot results.

During the 6C treatment, there were 404 events detected on the monitor well array and 433 events detected in MWX-3. Of these, 234 analyzable events were found in the monitor well data and 206 analyzable events were found in the MWX-3 wireline data. Of the 206 microseisms analyzed from the MWX-3 data set, 35 were events in which no data were available from the lower level and which therefore were automatically placed in the center of the sandstone.

Figure 33 shows example traces from a monitor-well microseism. This event has small p waves and large s waves across most of the array. Figure 34 shows a similar example for the two level system in MWX-3 (at a time when both levels were fully functional). The MWX-3 example shows a much different amplitude detected on the two levels, which are separated by 100 ft. The p wave is clear on both levels, but the s wave is most easily identified on the lower level.

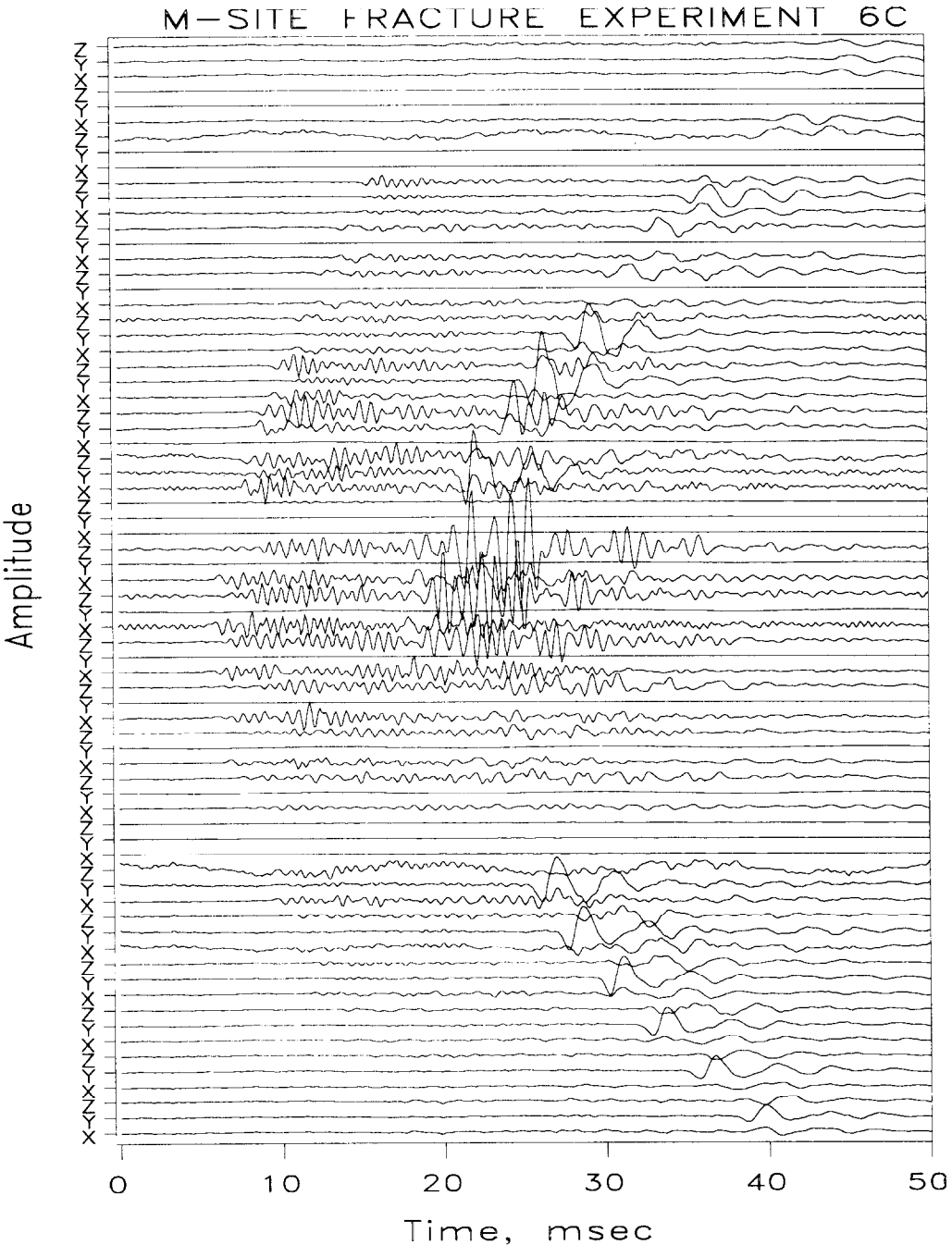

Figure 33 Example monitor well microseismic traces.

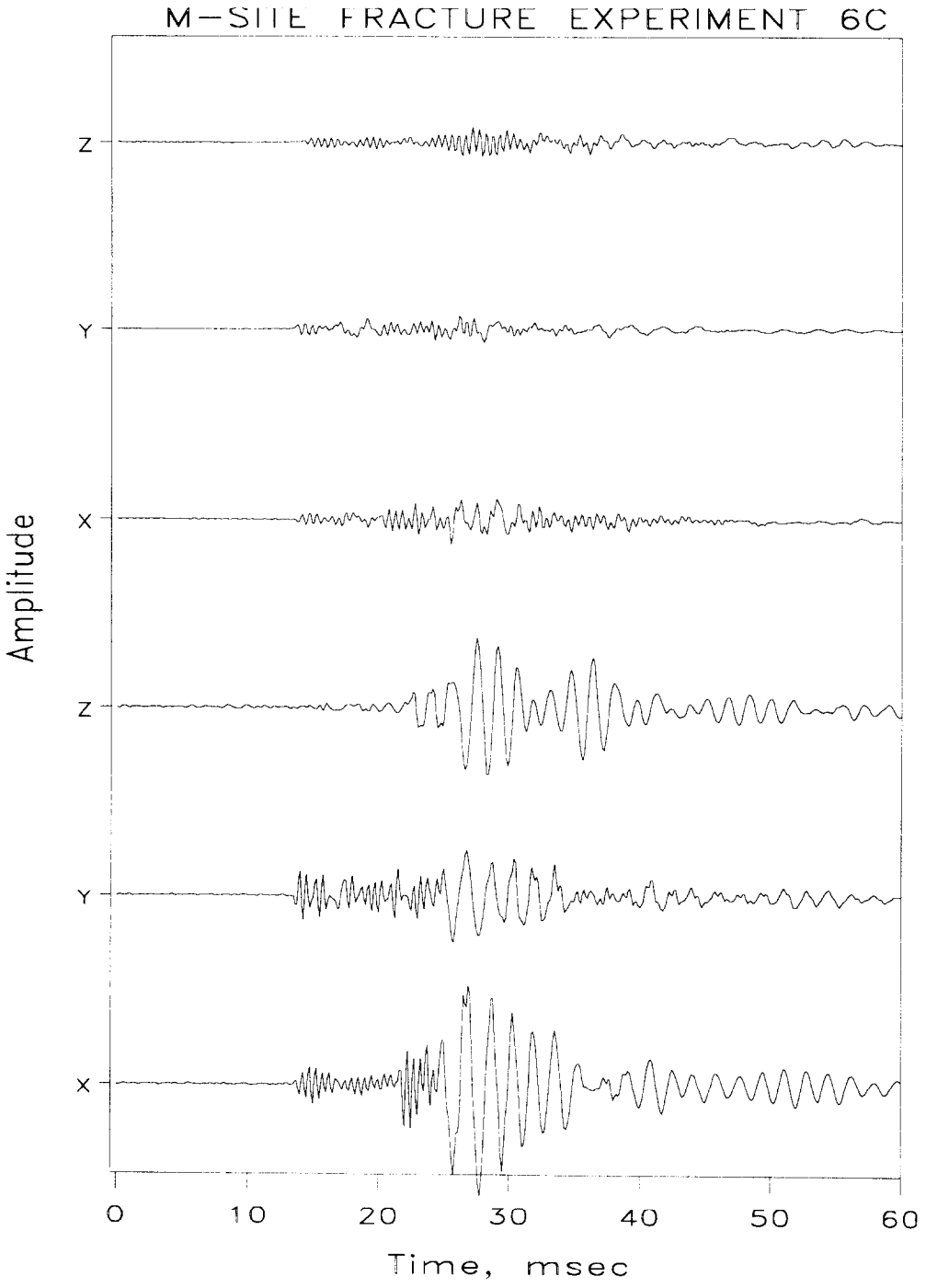

Figure 34 Example microseismic traces from the 2-level receivers.

Expanded traces for level 15 of the monitor-well array, at a depth of 4463 ft, are shown in Figure 35. This is perfect example of the form of a microseism because the x axis is pointing almost exactly at the microseism. Almost all of the p-wave energy is observed on the x axis, while almost all of the s-wave energy is found on the y axis, as would be expected for the different particle motions of the two phases. In addition, the frequency shift is obvious and the vertical s wave is not delayed as much as in many other microseismic examples. The hodogram plot for this example is shown in Figure 36 and there are no unusual or unexpected features. This microseism is located 85 ft from the treatment well on the east wing of the fracture.

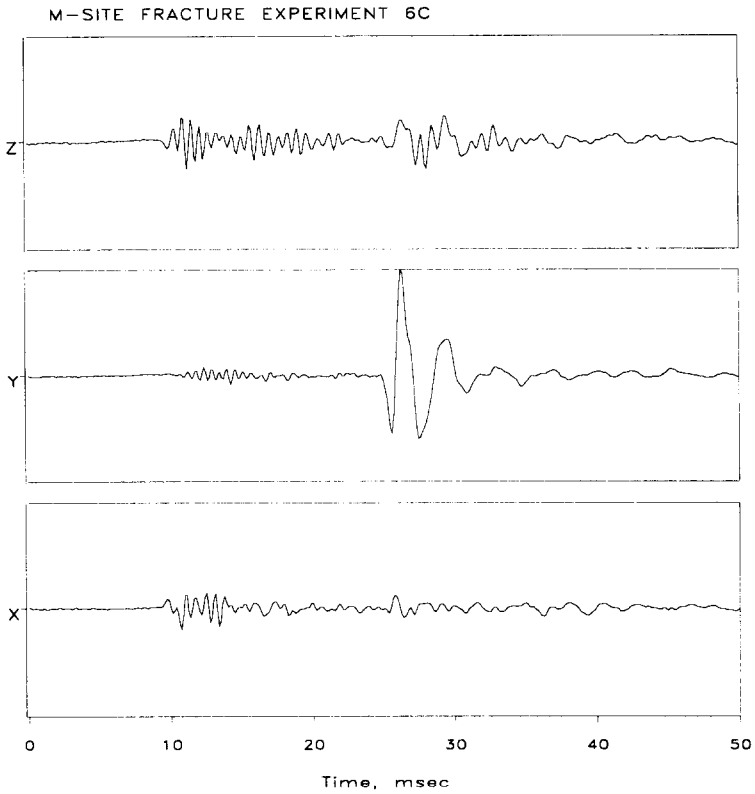

Figure 35 Example microseismic traces for level 15, monitor well.

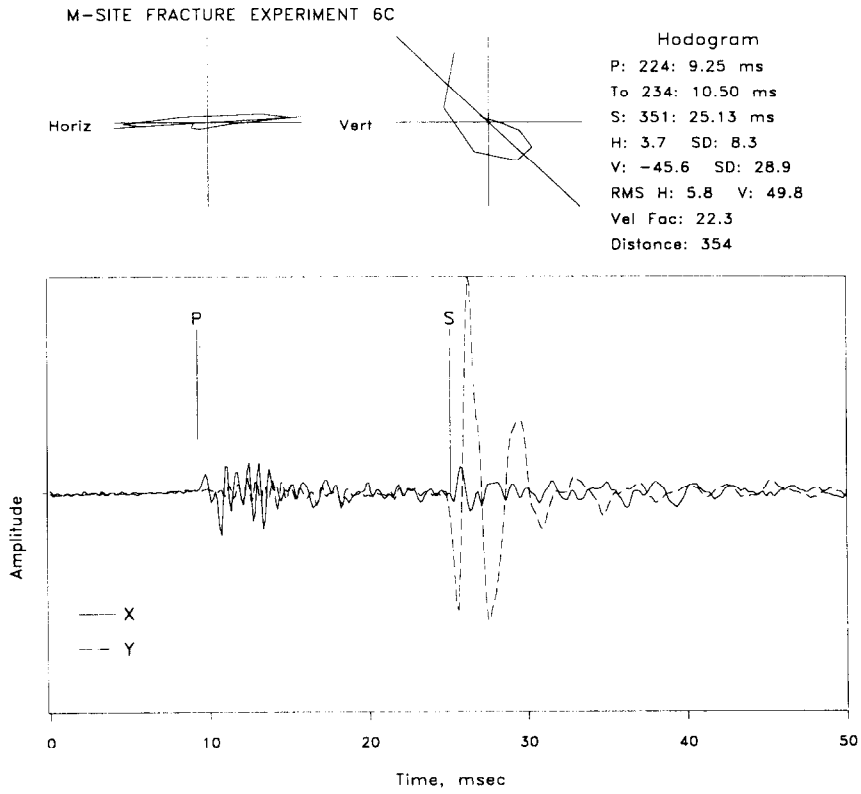

Figure 36 Example hodogram plot for level 15, monitor well.

Expanded traces for the lower level of the example wireline microseismic event are shown in Figure 37 and the hodogram plot is shown in Figure 38. This microseism is located 110 ft from the treatment well on the west wing of the fracture.

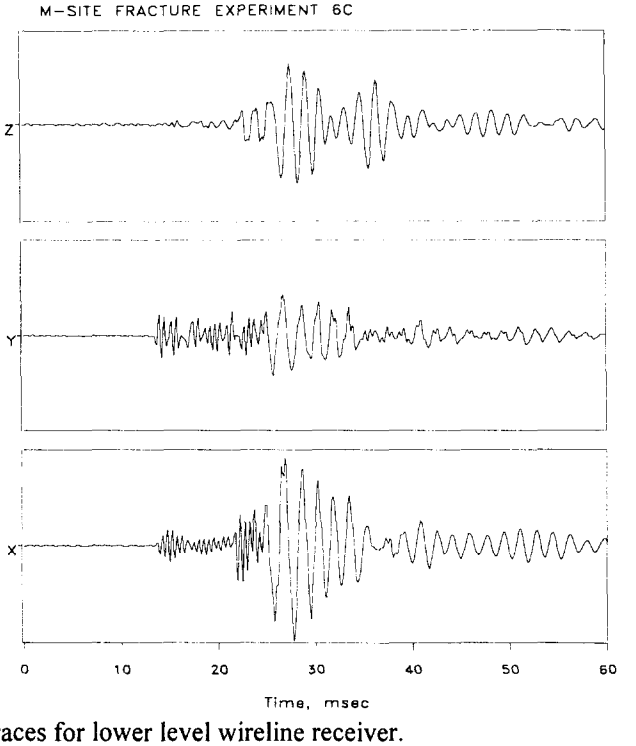

Figure 37 Example microseismic traces for lower level wireline receiver.

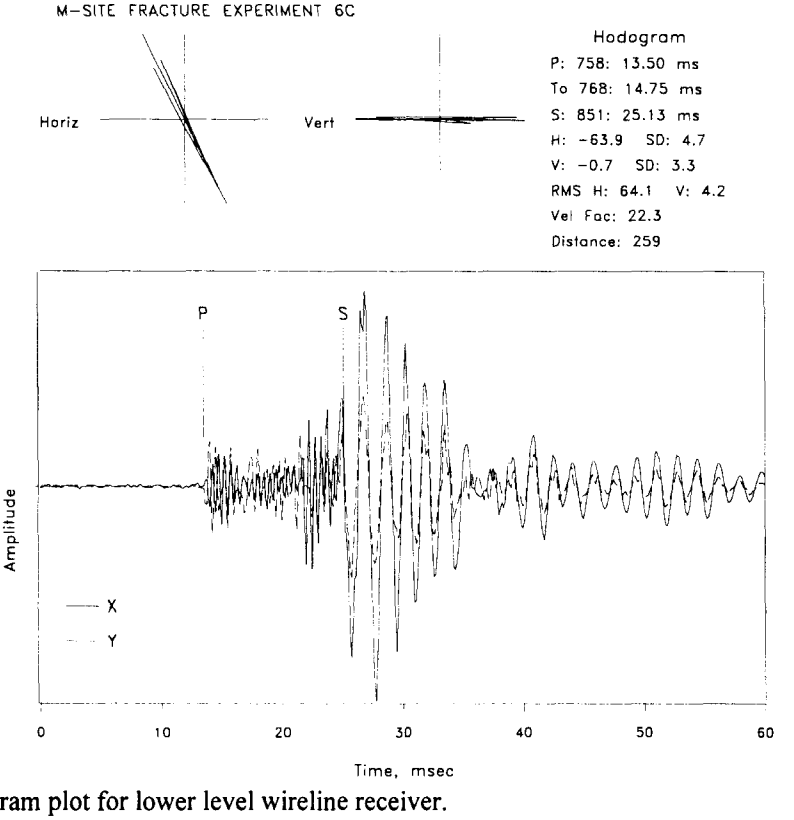

Figure 38 Example hodogram plot for lower level wireline receiver.

The microseismic activity after 15 minutes of injection is shown in Figures 39 and 40. By this time the fracture had extended at least 300 ft on each wing, but, more importantly, a clear secondary fracture(s) had propagated to the northeast and another secondary fracture may have extended more northerly. There is a high degree of certainty that these are secondary fractures because they are so much farther removed from the known fracture plane than any other microseisms detected previously (except for the initial detection of this same feature in the 4-C injection). They also begin to occur after the net pressure exceeds the maximum horizontal stress (estimated at approximately 4000 psi, based on data from deeper in the section). The treatment pressure exceeds 4000 psi after about 5 minutes of pumping and has reached 4600 psi (approximately the overburden stress) after 15 minutes of injection. At 15 minutes, the fracture is also relatively well contained within the C sand.

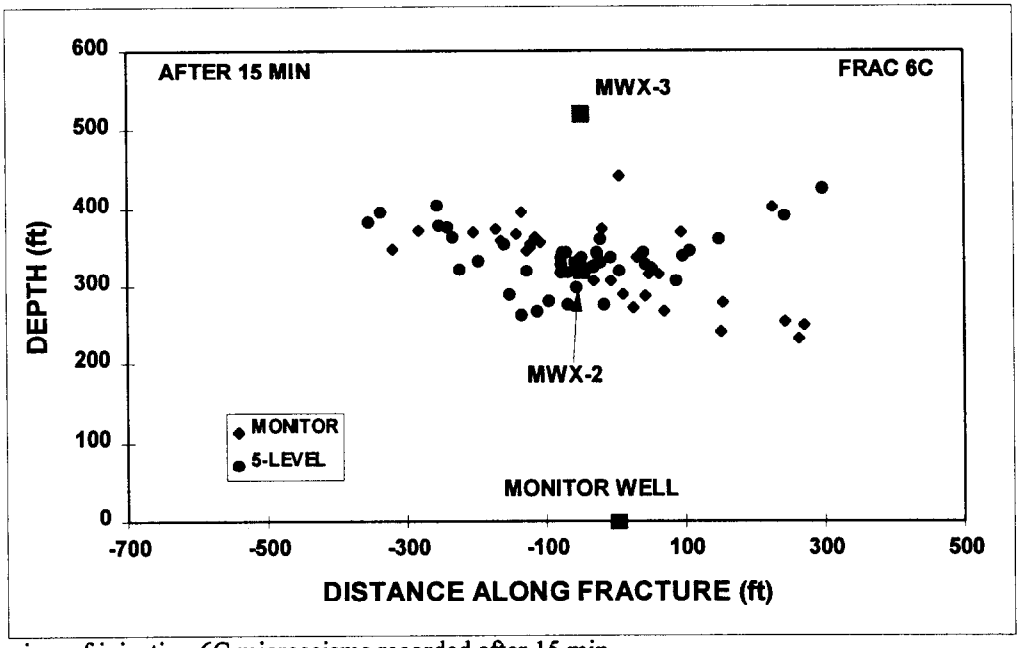

Figure 39 Plan view of injection 6C microseisms recorded after 15 min.

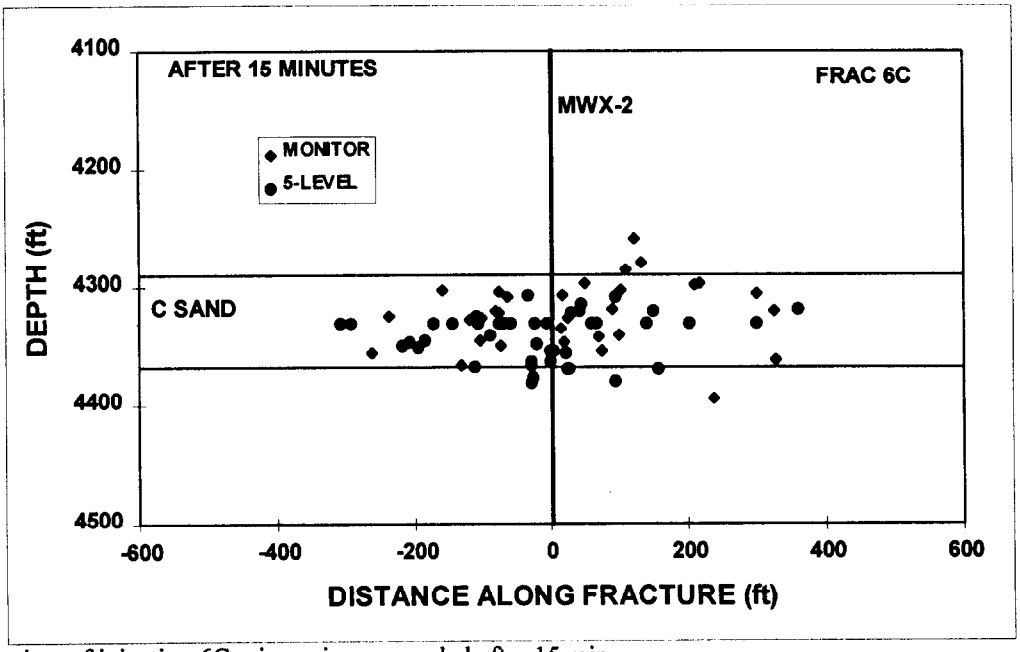

Figure 40 Side view of injection 6C microseisms recorded after 15 min.

After 30 minutes of injection the fracture shows more development of the complexity and a widening band of microseisms in response to the very high pressure levels. Plan and profile views at this time are shown in Figures 41 and 42. The secondary fracture(s) running northeast appears to have spawned or activated a subsidiary fracture running parallel to the original fracture direction. Length increased by only 50-100 ft, to a relatively symmetric wing length of 400 ft, but height growth downward was considerable during the 15-30 minute time span. Some upward growth is also evident. Treatment pressures have reached 4800 psi at this time, approximately 200 psi greater than the overburden stress.

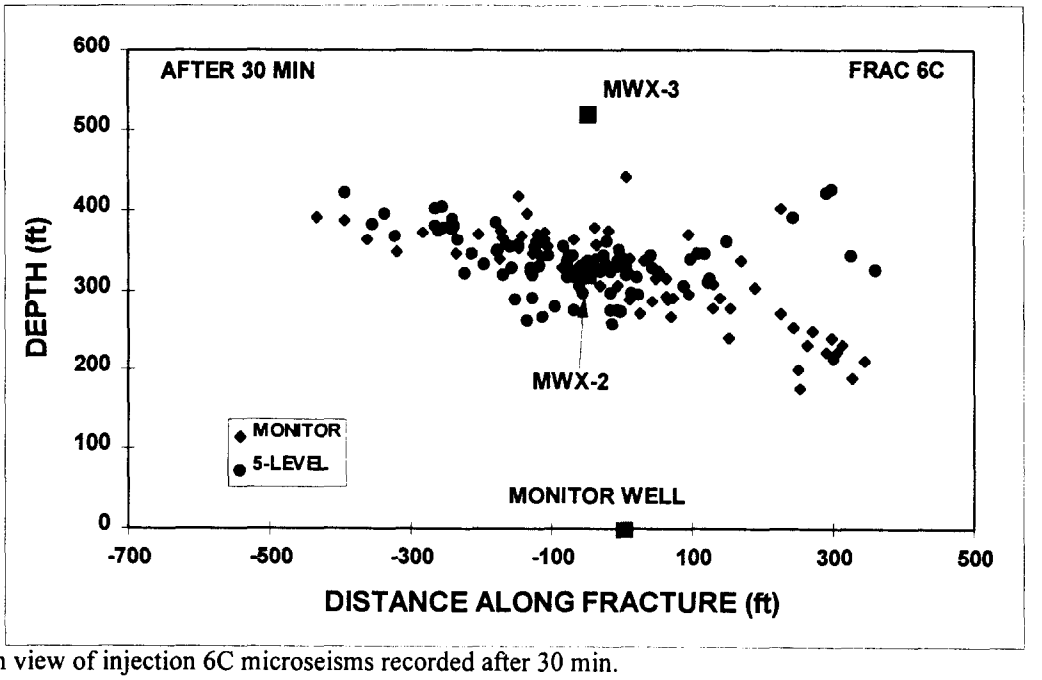

Figure 41 Plan view of injection 6C microseisms recorded after 30 min.

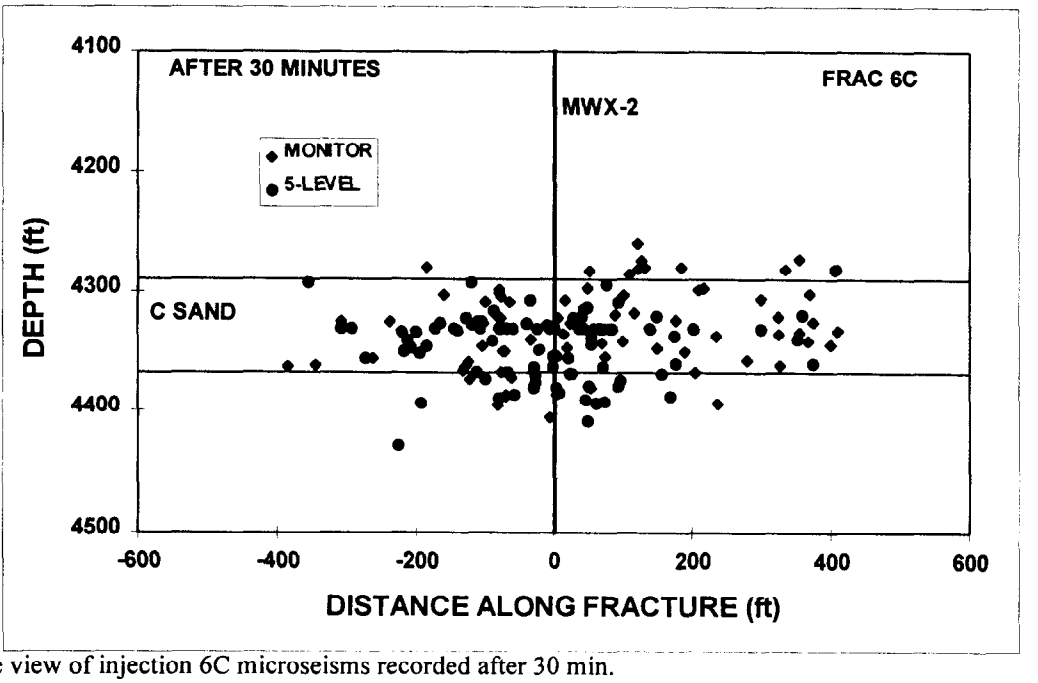

Figure 42 Side view of injection 6C microseisms recorded after 30 min.

After 45 minutes of injection, the pressure has passed 4900 psi. The plan and side views of the microseisms are shown in Figures 43 and 44. There are only small differences between the maps at this time slice compared to the previous time slice. The fracture appears to have grown mostly on the east wing, with some length extension and some height growth upward. Otherwise, the most obvious change is a widening band of microseisms and the filling-in of the fracture area with additional microseisms.

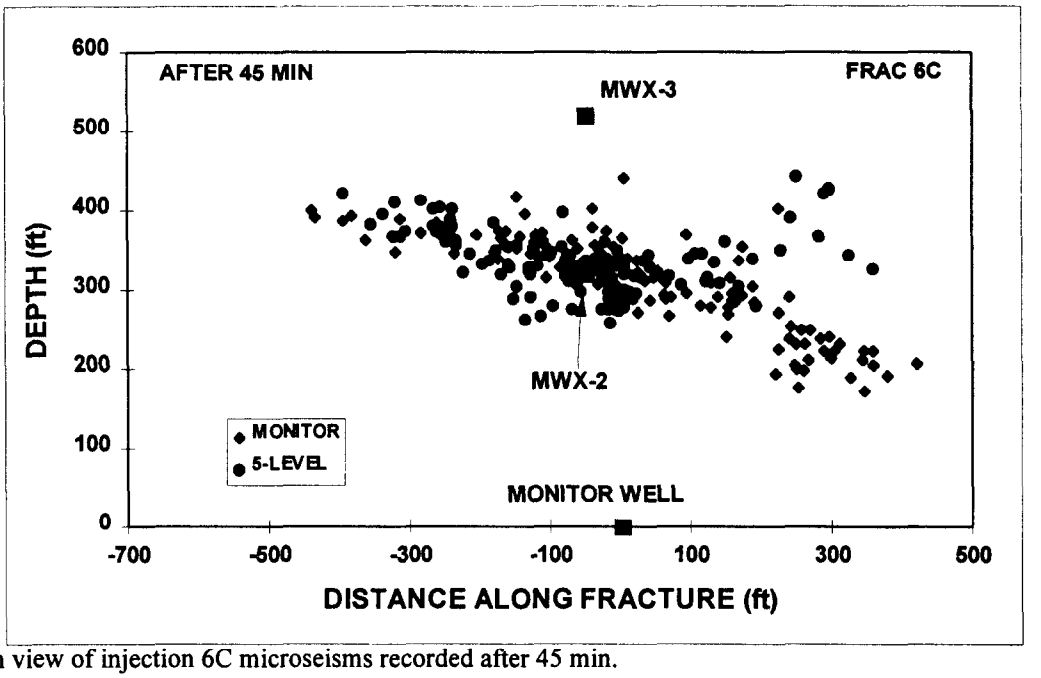

Figure 43 Plan view of injection 6C microseisms recorded after 45 min.

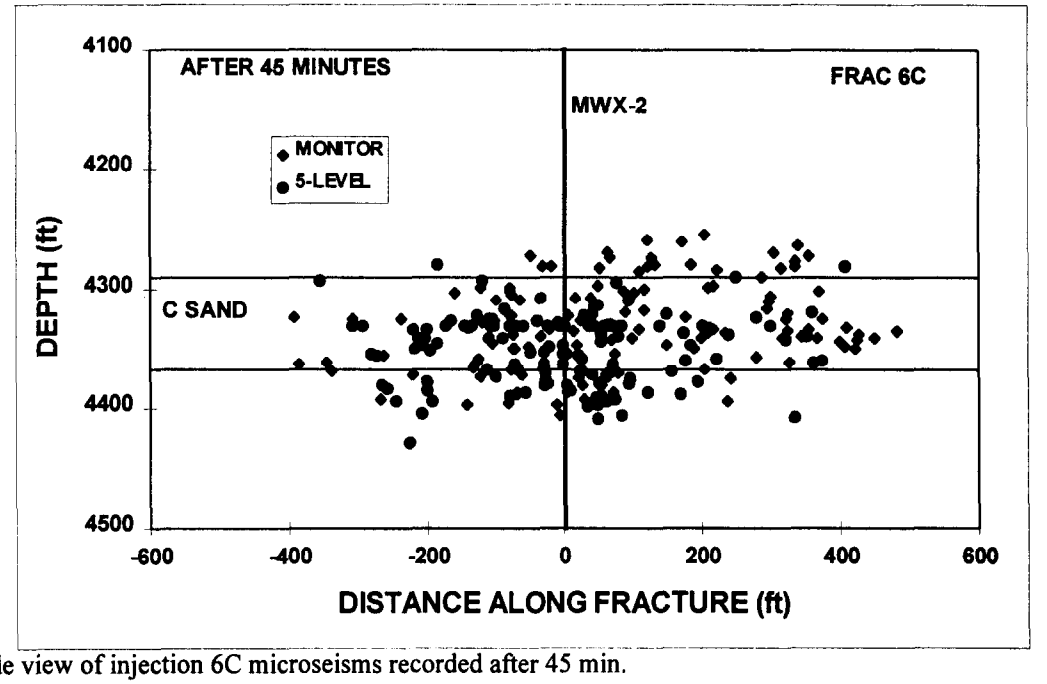

Figure 44 Side view of injection 6C microseisms recorded after 45 min.

After 60 minutes of injection, at which time the bottom-hole pressure was 4960 psi, the fracture has changed little in overall dimensions, as shown in Figures 45 and 46. However, it is beginning to shown some splaying on the southeast side which

indicates the initiation of some other complexity. Otherwise, most microseisms are occurring within the envelope of microseisms detected before 45 minutes. There is also one extreme point on the far west wing at about 600 ft from the treatment well. It is believed that single outliers such as these should be ignored, since they could occur on some very weak joint or may be mislocated due to some unknown systematic error (for example, a reflected signal).

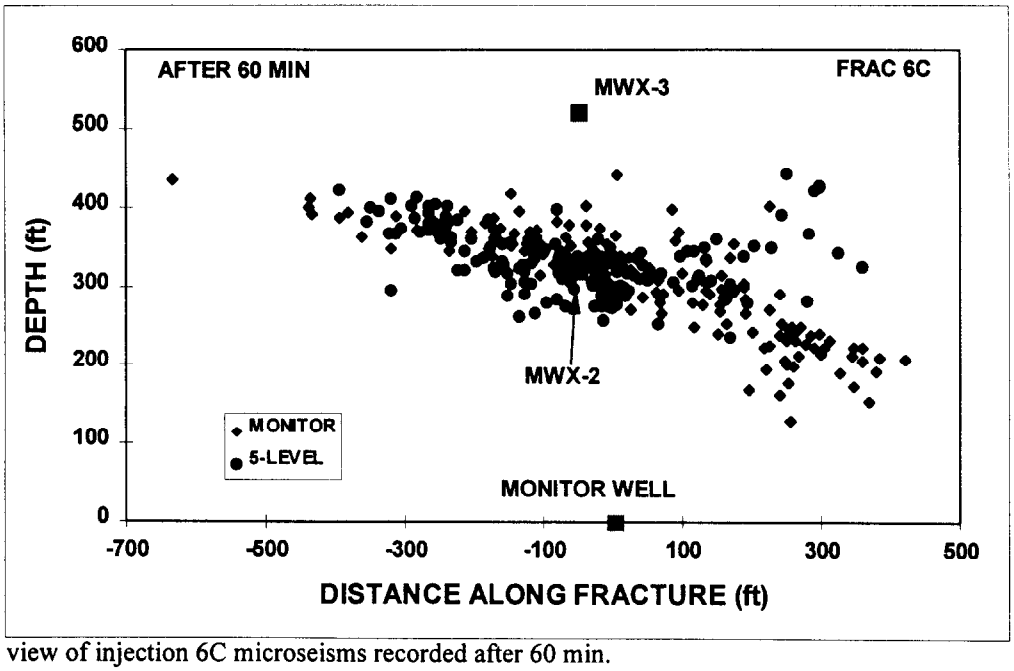

Figure 45 Plan view of injection 6C microseisms recorded after 60 min.

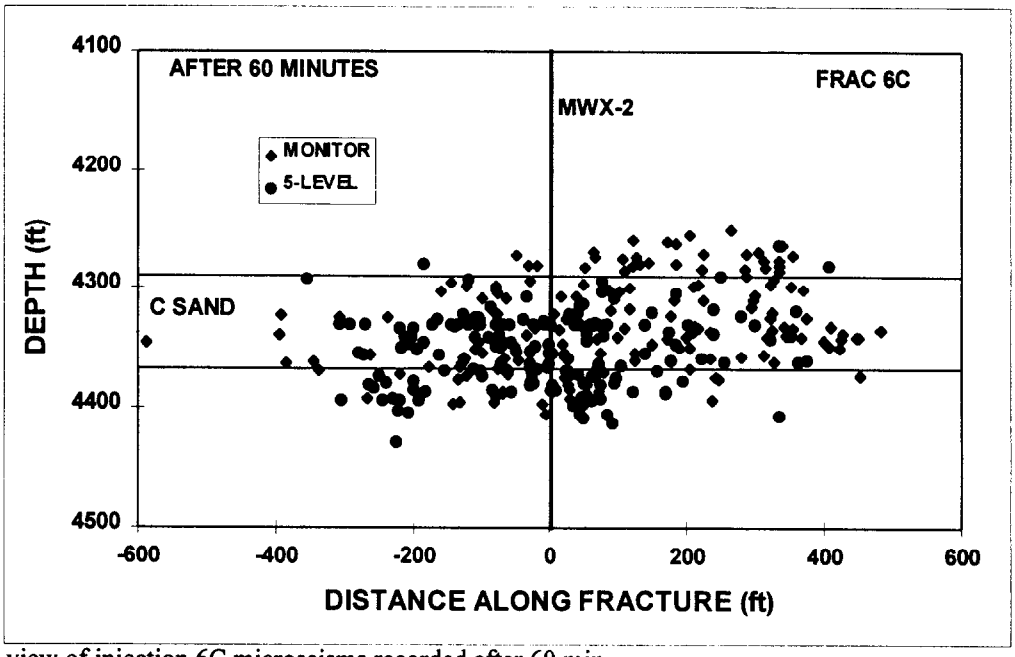

Figure 46 Side view of injection 6C microseisms recorded after 60 min.

After 75 minutes, which is 5 minutes after shut in, the microseismic plan and profile maps are shown in Figures 47 and 48. The primary change from the previous time slice has been the expansion of the southeast fracture side into a diffuse zone of

microseimic activity that extents 150 ft orthogonally from the original fracture plane. It also appears that the secondary fracture running northeast may have spawned or activated two parallel fractures rather than one.

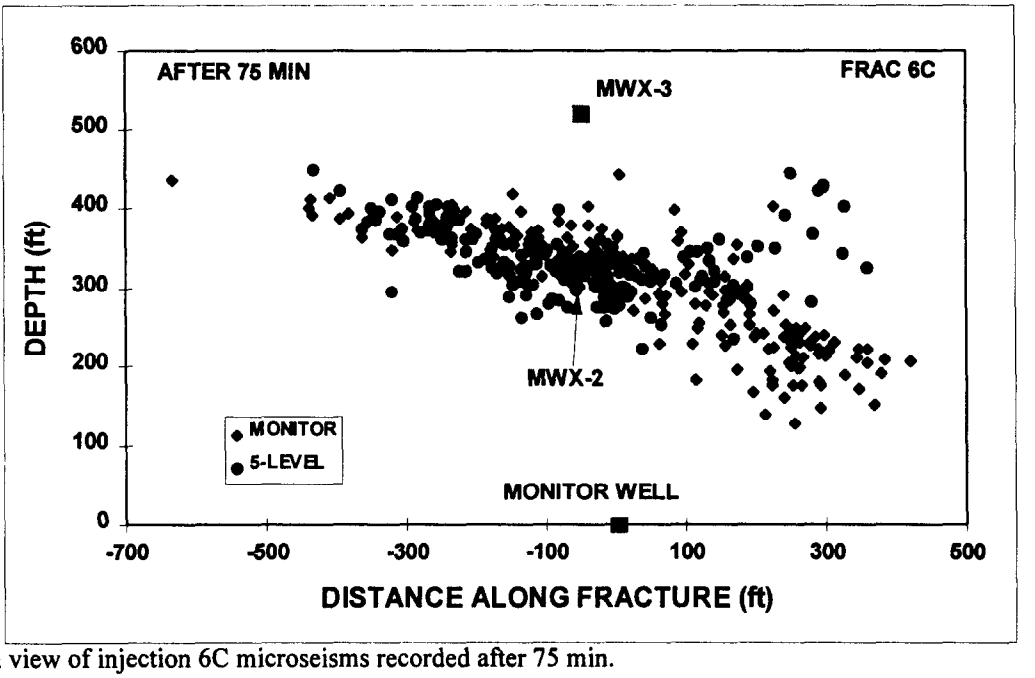

Figure 47 Plan view of injection 6C microseisms recorded after 75 min.

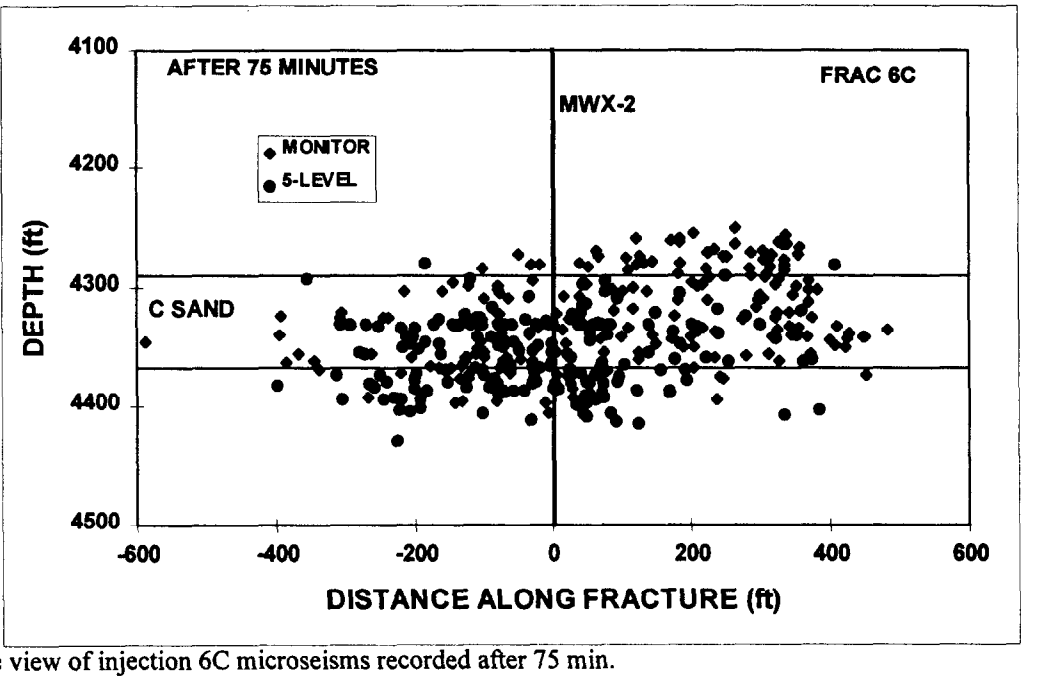

Figure 48 Side view of injection 6C microseisms recorded after 75 min.

The final microseismic images are shown in Figures 49 and 50. The final dimensions are wing lengths of about 450 and 425 ft on the east and west wings, respectively, and height growth of about 40 and 53 ft in upward and downward directions. However, the most notable new feature is the fan-like structure of microseisms on the southeast side of the fracture. This feature can be examined more carefully in an edge view (or width view) of the fracture taken from the east along the strike of the fracture. This view is shown in Figure 51 for all microseisms. It should first be noted that a normal fracture would

typically have a broad elliptical shape when seen in edge view. In Figure 51, there is a mass of microseisms in the center that maps out into such a broad ellipse. However the right side (north side) also has may other points extending to the north. These points are associated with the secondary fractures and indicate that the secondary fractures are vertical features, as there are microseisms scattered throughout the vertical section. On the other hand, the left side (south side) has most of the outlying microseisms near the top of the C sandstone. This distribution suggests that the fracture is likely to be a horizontal feature, or possibly a series of short vertical fractures confined to a limited zone near the top of the C sandstone. The most likely of these two scenarios is the horizontal fracture, as it is not clear what mechanism would confine the vertical fractures to a limited interval.

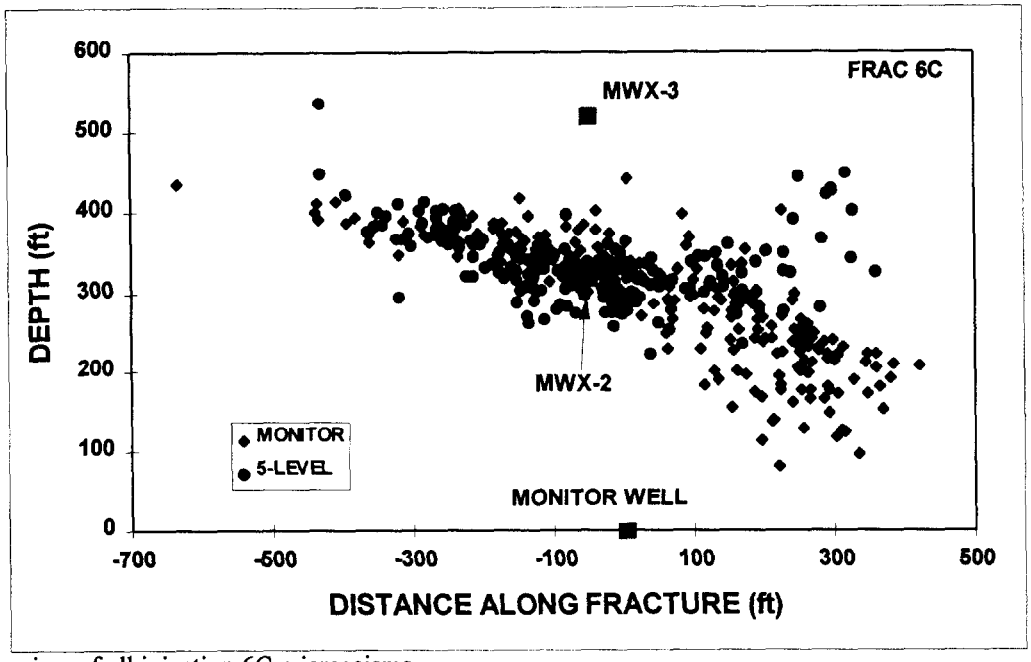

Figure 49 Plan view of all injection 6C microseisms.

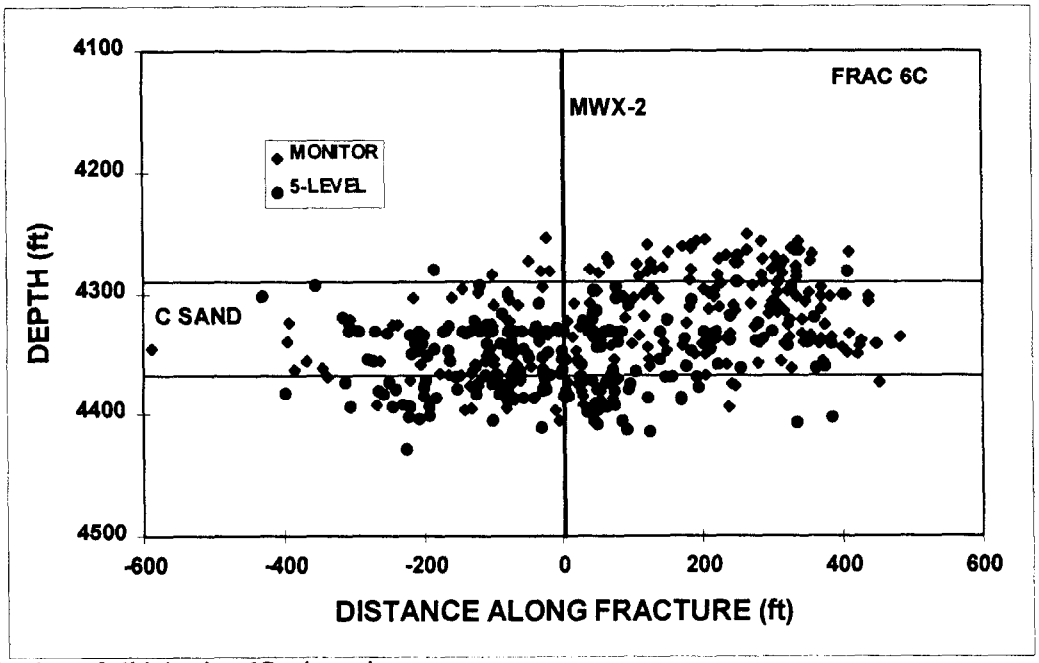

Figure 50 Side view of all injection 6C microseisms.

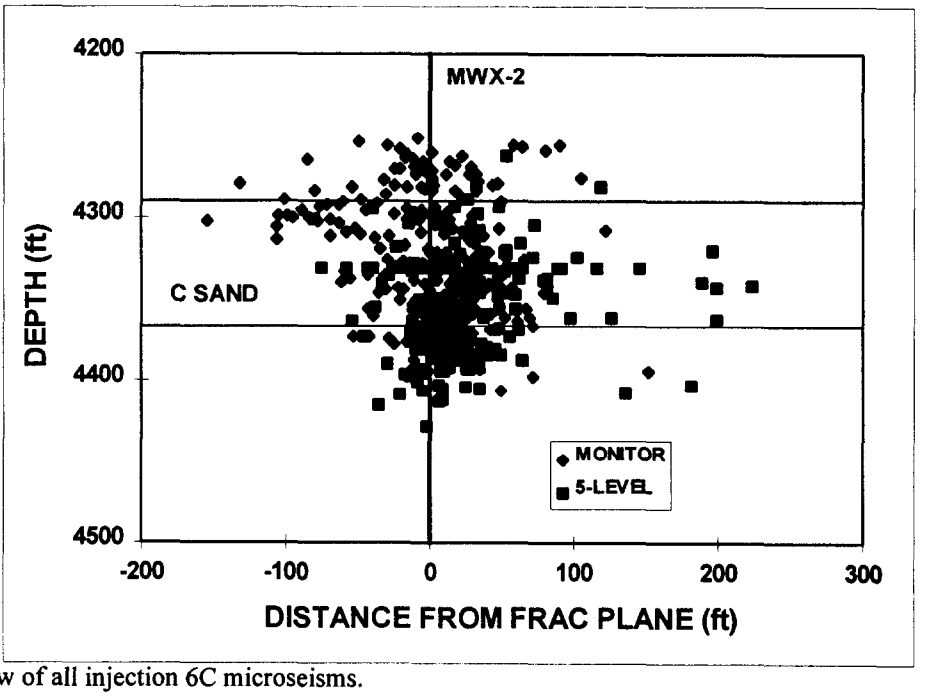

Figure 51 Edge view of all injection 6C microseisms.

In summary, the microseismic development shows a fracture that is extremely complex with clear secondary fractures and a possible horizontal fracture. The length is very short for having injected over 2000 bbl of fluid and the height shows insignificant height growth compared to the net pressures (400 psi greater than any measured or expected stress contrast). Much of the injected volume must have gone into secondary fractures, horizontal fractures, or fissure opening to account for mass balance.

What is most interesting about these results is that the net treatment pressure shows no evidence of complexity, other than the fact that the pressures are high. However, given the fact that bottom-hole pressures are not recorded on most fracture treatments, in a typical fracture treatment it is not likely that there would be any indication of such complexity from the normally acquired data.

8.4 M-Site Closure

After the completion of the C-sandstone experiments, the M-Site was closed and abandoned at the request of the site operator. No additional test can or will be performed at M-Site; however, analysis of the enormous data set is continuing.

9.0 INDUSTRY DIAGNOSTIC EXPERIMENTS

9.1 Mitchell Energy Barnett Shale Test

On May 3, 1997, a diagnostic test was conducted in the Barnett shale with Mitchell Energy Corporation. The test was originally set up to be a test of the 5-level system for monitoring microseisms induced by hydraulic fractures in the Barnett shale. However problems with the 5-level system forced us to try to use a backup 3-level system for fracture monitoring. Results obtained using the 3-level system were difficult to interpret and leave some questions about fracture behavior.

9.1.1 Original Test Design

The original test design was to employ the 5-level advanced accelerometer receiver system in the Sewell Ranch #3 well to monitor a fracture in the Sewell Ranch A#2 well, at a distance of 1120 ft. The 5-level system, leased from OYO Geospace Instruments and run by Bolt Technologies, was emplaced on May 16 and was found to function adequately. The expected fracture date was May 21 (with orientation perforations the day before), but weather problems forced a delay until later in the week. Unfortunately, on May 20, the tool began to have communication problems and eventually the entire system died. Bolt/OYO attributed the communication loss to interconnect problems caused by higher than expected temperatures. They decided that the interconnects had essentially melted and were no longer usable. Since new interconnects would require several weeks to procure and Mitchell could not afford to delay the fracture, it was decided to try to run a backup system and obtain as much data as possible.

9.1.2 Backup Test Design

The hybrid 3-level backup system consisted of one full-three-component, geophone, analog sonde, a second three-component, geophone, analog sonde in which the vertical sensor was disconnected, and a hydrophone for the third level. With 100-ft spacing between the sondes, the three level system would provide enough arrival-time data to triangulate on microseism source locations and two levels from which to measure the azimuth to the source. Only seven channels could be monitored because the data were analog and were transmitted up hole on 7-conductor wireline.

Unfortunately, even the backup system experienced problems. One of the three-component sondes failed downhole and the delay in fixing the sonde resulted in the site engineer foregoing any perforation orientation shots. Furthermore, the problem with the sonde also ruined the only 100-ft interconnect that Bolt/OYO had available. Finally, the hydrophone was unstable at the bottom-hole temperature and provided little useful data. As a result, the backup system ended up being a two-level system with only a 40-ft interconnect between the sondes, an insufficient separation to adequately triangulate on the source location.

On the positive side, many high quality microseisms were detected (at least 200). This memo details the limited information obtained from analysis of these data.

9.1.3 Example Microseism

Figure 52 shows an example microseismic trace from the top receiver and the hodogram data from this level. The two horizontal traces are shown on the lower part of the figure, in which clear p waves and s waves are observable, as well as the phase relationships. The top center of the figure shows the horizontal hodogram, indicating that the azimuth to the microseism is 38 degrees from the x axis and is well polarized (accurate azimuth). The right hand top section is the vertical hodogram and is only used as a check for head waves. Details on this level are given on the top left side of the figure.

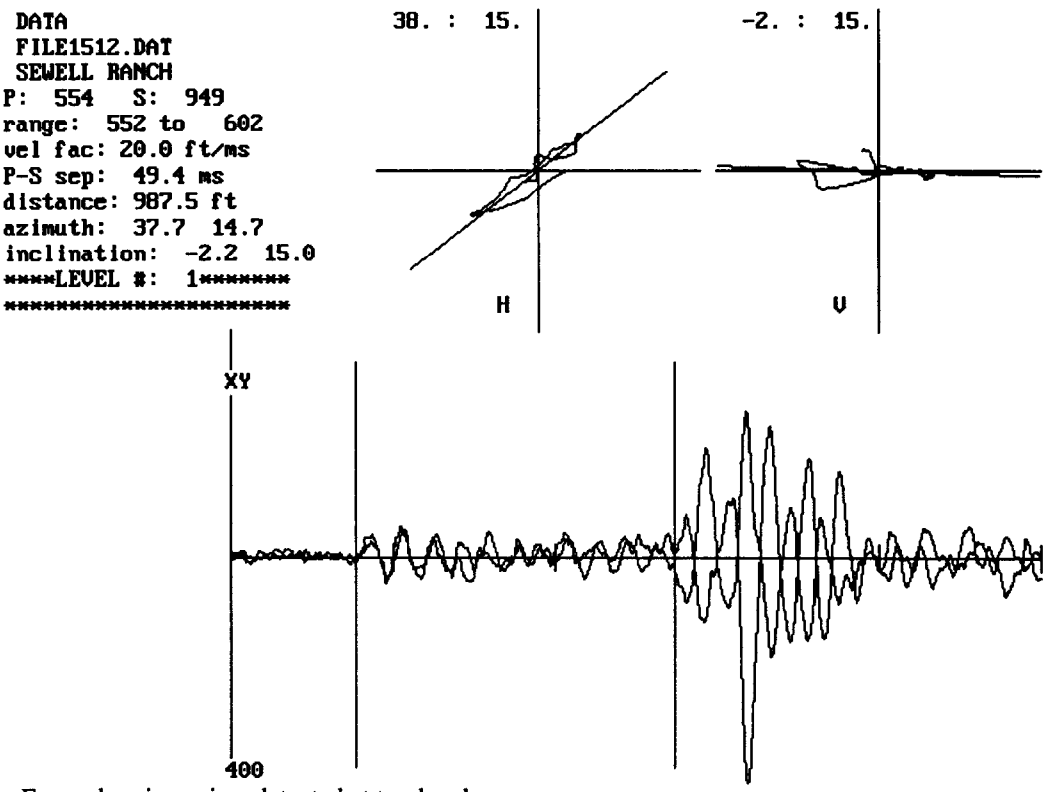

Figure 52. Example microseism detected at top level.

The same microseism was detected on the second level and is shown in Figure 53. The major difference between this level and the previous level (Figure 1) is that there is no vertical sensor and, thus, no vertical hodogram. This example also shows a good quality microseism. Most of the detected events look similar to Figures 1 and 2.

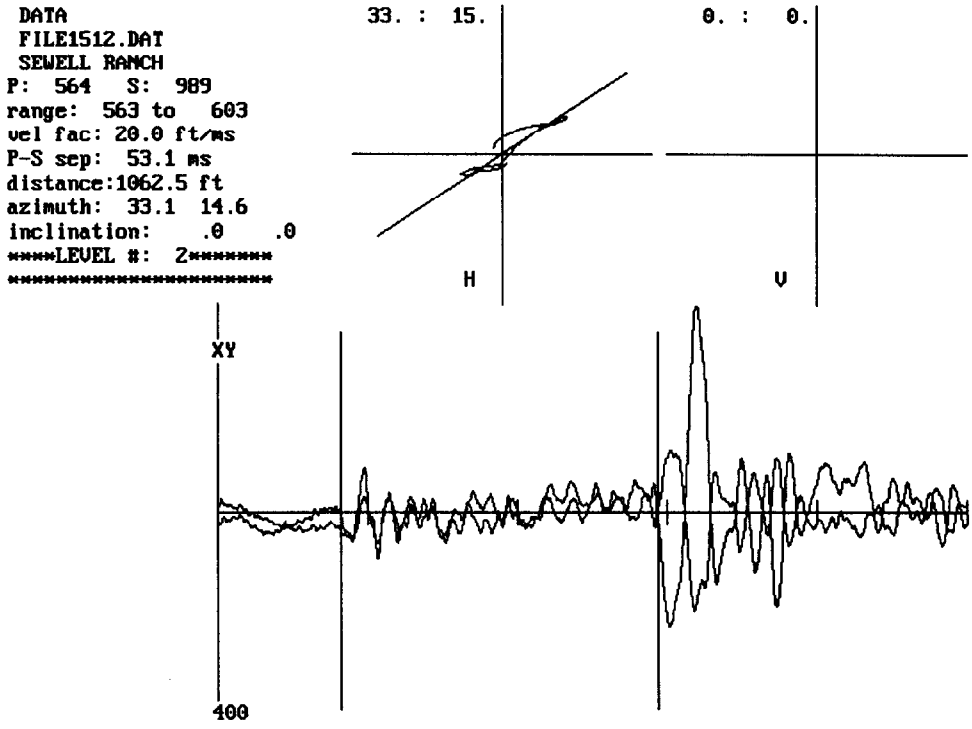

Figure 53. Example microseism detected at second level.

These microseisms can be located a number of ways, but with such close spacing between receivers, the only accurate methodology is to use the p-s arrival-time difference to calculate distance to the source and the p-wave polarization (horizontal hodogram) to determine the azimuth.

9.1.4 Microseismic Results

Having picked the best quality microseisms and determined source locations, a plan-view map of the detected events is shown in Figure 54. The A#2 well is located at (1100, -175) and the regression line has an angle of about N68°. However, this figure is not a particularly clear image of the fracture, does not show significant length extension, and does not give a statistically significant azimuth (although it is roughly aligned with an expected northeast fracture azimuth). We have re-evaluated these data several times trying to find some systematic error, but have not been able to determine any reason for such a jumbled picture of the fracture.

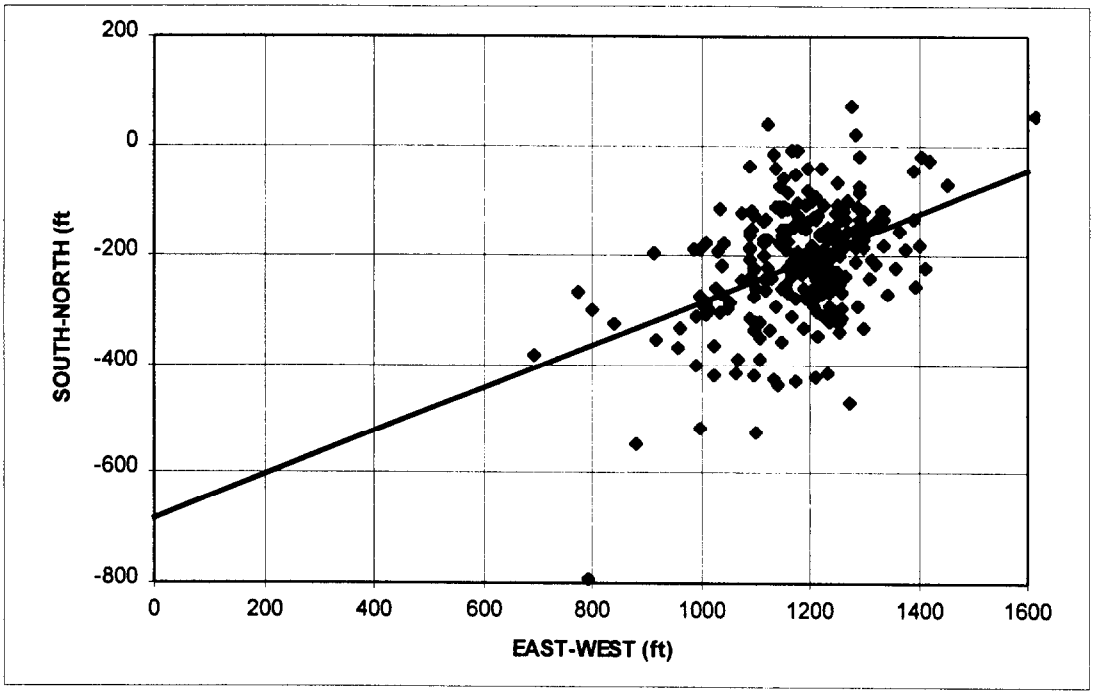

Figure 54. Map of detected microseisms relative to the monitor well (0, 0).

If an error exist, the two most likely sources are (1) our inability to determine the true elevation to the source (hence, we assume the source is horizontally straight across) causes errors in the horizontal location, as many of the microseisms may actually be much higher or lower, and(2) the lack of orientation perforations has caused a systematic error. We tried to account for the first source by examining the vertical hodogram of the top level to see if many of the events appeared to be head waves. This did not seem to be a common problem. Regarding the second possible error, we used the initial few microseisms to orient the receivers, assuming that they originated near the treatment well. If this assumption is in error, then the map could also be in error, but it is hard to see how it would result in the cloud of microseisms seen in Figure 54.

9.1.5 Post-Test Re-Evaluation of Receiver System Problems

After this test was completed, Sandia requested that BOLT send some of the "melted" wirelines to us for examination. It took a few months to obtain these materials due to changing personnel and the dropping of BOLT

as the industry partner. When received, the examination consisted of a visual inspection, a resistance check, a short check, and a capacitance check of each of the 12 conductors on two cables. Our examination found that the interconnect wirelines suffered no signs of melting and were functioning within operating parameters. The problem with the system was not due to the interconnects. This result, coupled with information from the subsequent Barrett test, led us to further investigate the causes of the problem.

Table 4 Receiver and perforation depths

RECEIVER DEPTH (203-33)	RECEIVER DEPTH (201-4)		PERFORATION DEPTH (201-4)	NUMBER OF PERFORATIONS
5640	5567		5412-14	6
5690	5617		5276-77	4
5790	5717			
5890	5817			

Figure 57 shows the traces of the deepest perforation (at 5412-14 ft) as recorded on the four-level system. Starting at the bottom, Figure 57 shows the two horizontal axes (x, y) and the vertical channel (z) for the lowest receiver and then similar data for each successively shallower receiver. This figure shows that there is an excellent response to the perforations, but the magnitude is low for 72 total grams of perforation charge. The p wave is easily visible in the figure, but the s wave is more difficult to find in this presentation (it should arrive about 1 division later).

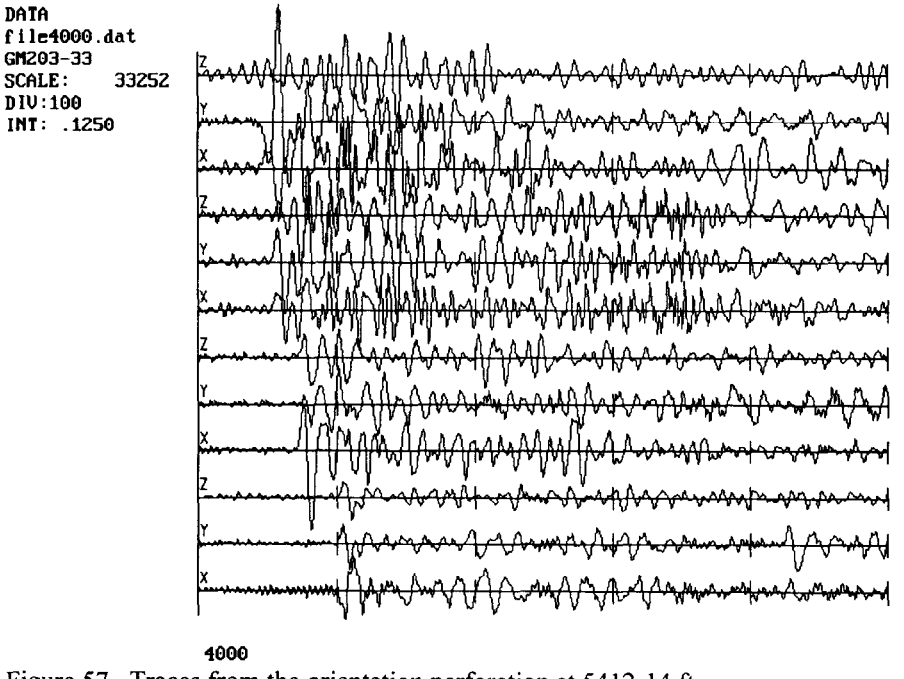

Figure 57. Traces from the orientation perforation at 5412-14 ft.

Figure 58 shows the traces from the shallowest level (5567 ft), including overlain horizontal traces (bottom plot), horizontal hodogram (top center plot), vertical hodogram (top right plot) and measured data (top left text). This figure shows that the p-wave arrival is well defined (first vertical line on lower plot) and that it is highly polarized with an orientation of -67.5° relative to the treatment well (top center hodogram plot). The vertical hodogram shows that the waves are traveling nearly horizontally (not head waves through some high velocity layer). The s-wave arrival is not entirely clear, but an s-wave is definitely present, as can be seen by the change in phase that occurs after the second vertical line on the lower plot.

The only discrepancy seen in these results is the calculated distance to the perforation (855 ft), which is significantly less than that determined by the well-deviation surveys (735 ft from the perforation to the top receiver). There could be two reasons for this discrepancy. Either the velocity factor, $V_pV_s/(V_p-V_s)$, is much lower than that measured at M-Site (22.3 ft/msec) or the s-wave arrival is in error. A velocity factor of 19 ft/msec, instead of 22 ft/msec would bring the distances into agreement, as would a 5-msec earlier s-wave arrival (which is possible here since the s-wave arrival is not particularly clear). Post-fracture examination of a dipole sonic log from the 201-4

well suggests that the 19 ft/msec velocity is probably correct (V_p=14.3 ft/msec and V_s=8.2 ft/msec), but it is not clear why the velocity structure should be so different from M-Site since both sites have the same depositional environment.

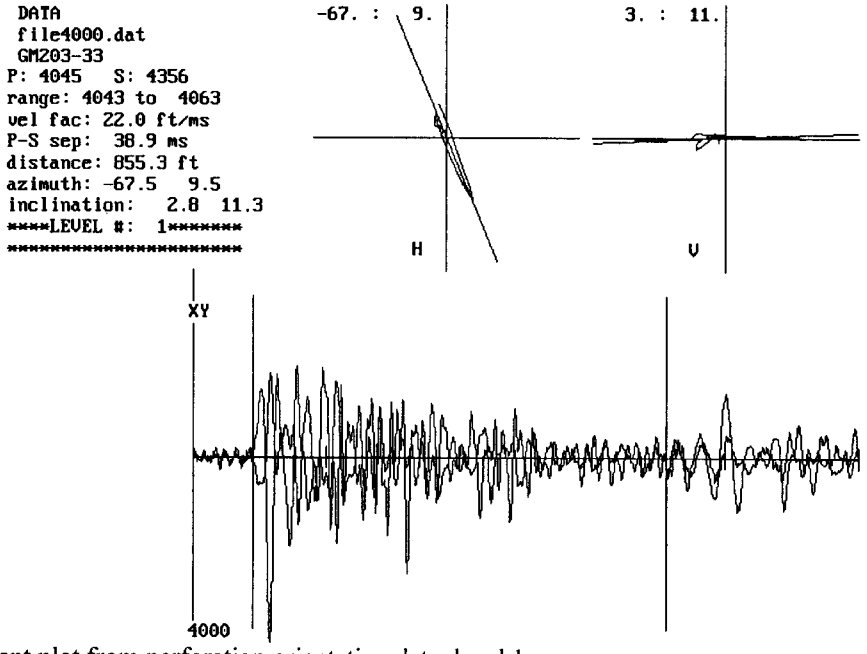

Figure 58. Resultant plot from perforation orientation data, level 1.

Similar data from level 2 are shown in Figure 59. This level has an orientation of 58.1° relative to the treatment well (each of these tools rotates differently in the wellbore, so the difference between levels 1 and 2 is not surprising). The p wave is strong with good polarization, but the s wave is again weak and difficult to use for estimating the velocity factor. Based on the arrival-time picks shown in Figure 5, a velocity factor of 18 ft/msec would be required to match the measured distance (747 ft).

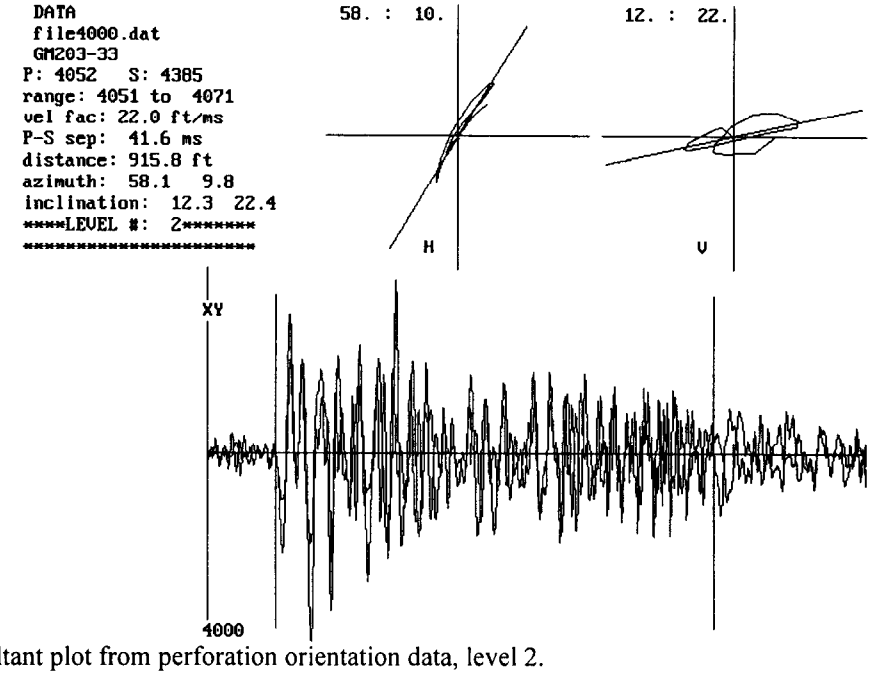

Figure 59. Resultant plot from perforation orientation data, level 2.

The same information for levels 3 and 4 are shown in Figures 60 and 61. Velocity factors of 19.9 and 20.2 would be necessary to match the actual distances to the perforation location. Based upon perforation data alone, a velocity factor of 20 appears appropriate for this location, which is not unreasonable based upon the dipole sonic data.

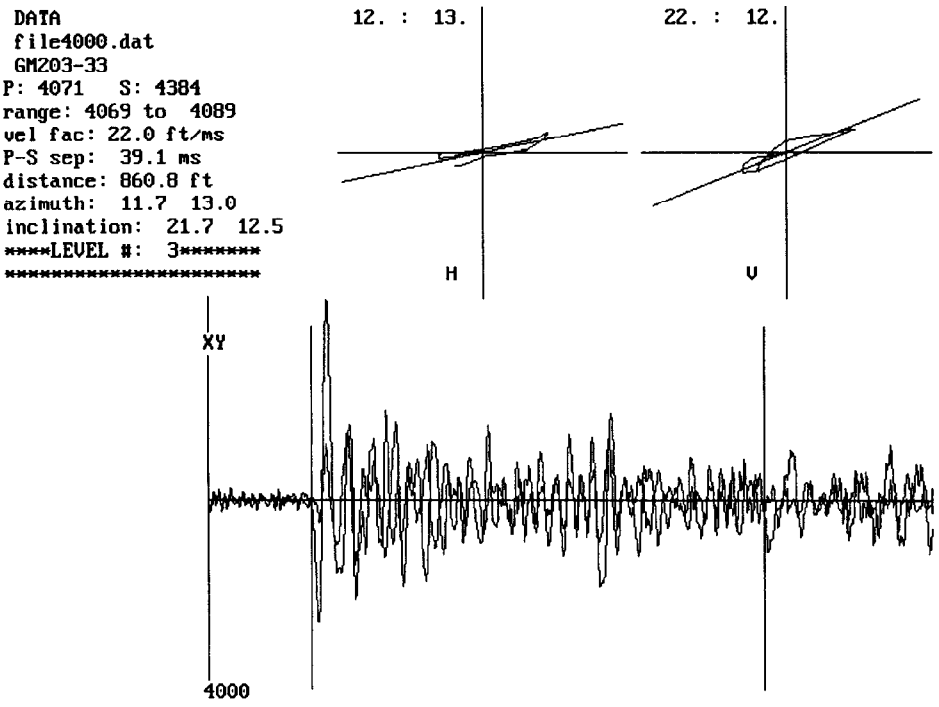

Figure 60. Resultant plot from perforation orientation data, level 3.

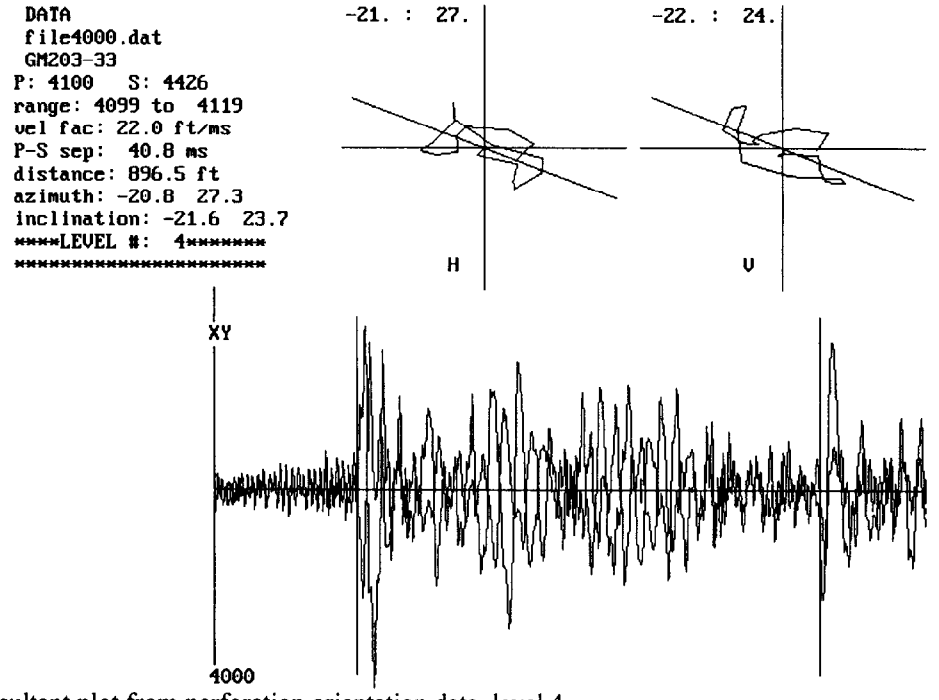

Figure 61. Resultant plot from perforation orientation data, level 4.

microseimic activity that extents 150 ft orthogonally from the original fracture plane. It also appears that the secondary fracture running northeast may have spawned or activated two parallel fractures rather than one.

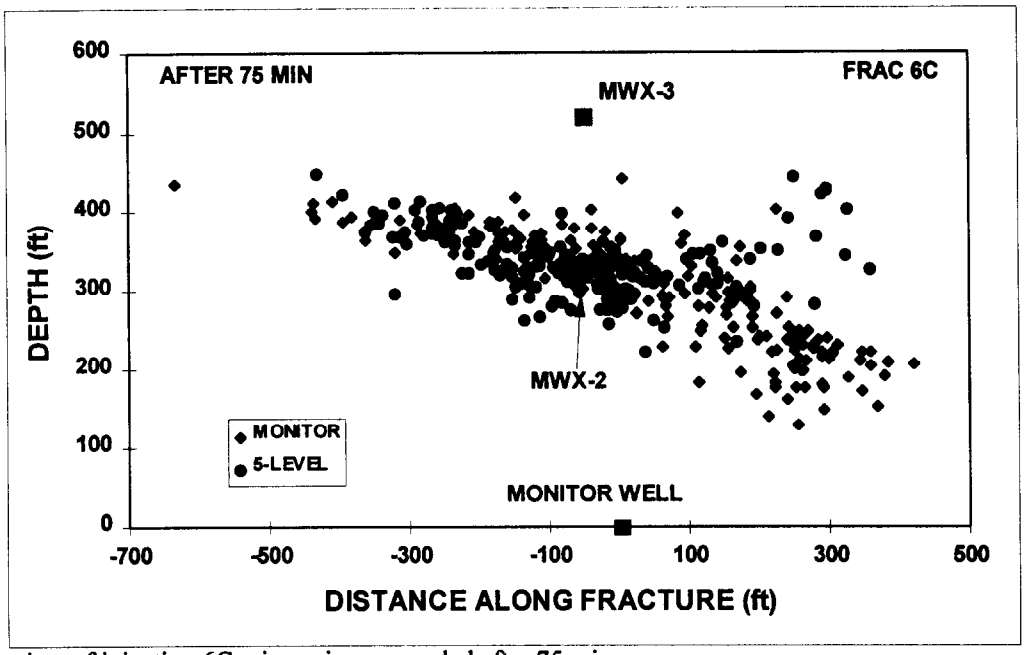

Figure 47 Plan view of injection 6C microseisms recorded after 75 min.

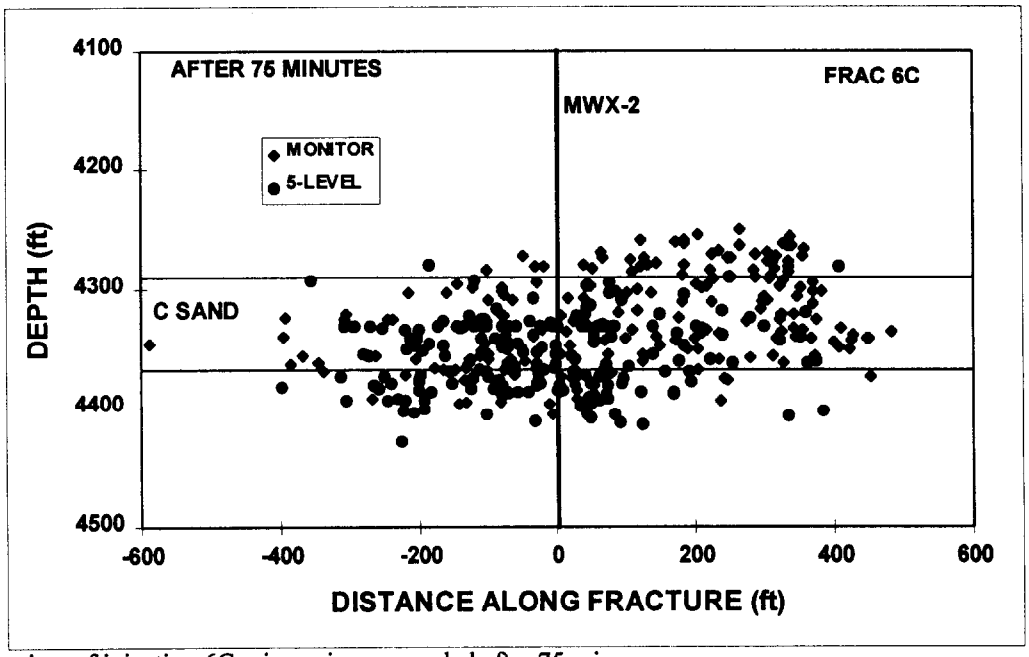

Figure 48 Side view of injection 6C microseisms recorded after 75 min.

The final microseismic images are shown in Figures 49 and 50. The final dimensions are wing lengths of about 450 and 425 ft on the east and west wings, respectively, and height growth of about 40 and 53 ft in upward and downward directions. However, the most notable new feature is the fan-like structure of microseisms on the southeast side of the fracture. This feature can be examined more carefully in an edge view (or width view) of the fracture taken from the east along the strike of the fracture. This view is shown in Figure 51 for all microseisms. It should first be noted that a normal fracture would

as the industry partner. When received, the examination consisted of a visual inspection, a resistance check, a short check, and a capacitance check of each of the 12 conductors on two cables. Our examination found that the interconnect wirelines suffered no signs of melting and were functioning within operating parameters. The problem with the system was not due to the interconnects. This result, coupled with information from the subsequent Barrett test, led us to further investigate the causes of the problem.

9.2 Barrett Resources Mesaverde Test

A joint GRI/Barrett microseismic diagnostic test was conducted in the GM203-33 well on June 17, 1997. This test consisted of a 4-level advanced seismic receiver system monitoring a fracture treatment in the nearby GM201-4 well in a zone designated MV I.

9.2.1 Experiment Design

The original design called for a 5-level diagnostic system with 100-ft spacing between interconnects to monitor the treatment from a distance of about 700 ft. Because of receiver-system problems, only a four-level system could be fielded and the spacings were 50 ft between the top two receivers and 100 ft between the 2nd and 3rd and the 3rd and 4th receivers. While four receivers is an adequate number for such diagnostic tests, the 50-ft interconnect resulted in two subtle effects which may have affected the analysis. First, the array aperture was only 250 ft, considerably less than half the distance between wells (the optimum) and less than the treatment zone thickness. Second, the data were biased toward the top of the interval where more tools were located.

The monitoring consisted of (1) data gathering during the MV I treatment (four sets of perforations between 5529 and 5840 ft) and (2) detection of perforation shots prior to the MV II treatment to orient the receivers. The treatment consisted of a short minifrac and a standard Barrett Resources Corp. stimulation, both conducted on June 17, 1997.

9.2.2 Imaging Results

Surprisingly, only a few microseisms were observed during the treatment and most of these were of very small magnitude. As a result, the test did not produce a satisfactory image of the fracture or its growth process. Figure 55 shows a plan view of the 20 or so analyzable microseisms, as seen at the midpoint of the perforations. Since both wells are somewhat deviated, this plan view shows the locations at the depth of the mid-point of the perforations in the treatment well. These data appear to show an azimuth of N79°W, with a total wing length of 250-300 ft. While there are only a limited number of points, the regression is relatively tight and appears to be oriented in the known stress direction, giving us confidence that we were, in fact, monitoring microseisms associated with the fracture treatment and not microseisms associated with production or some other mechanism.

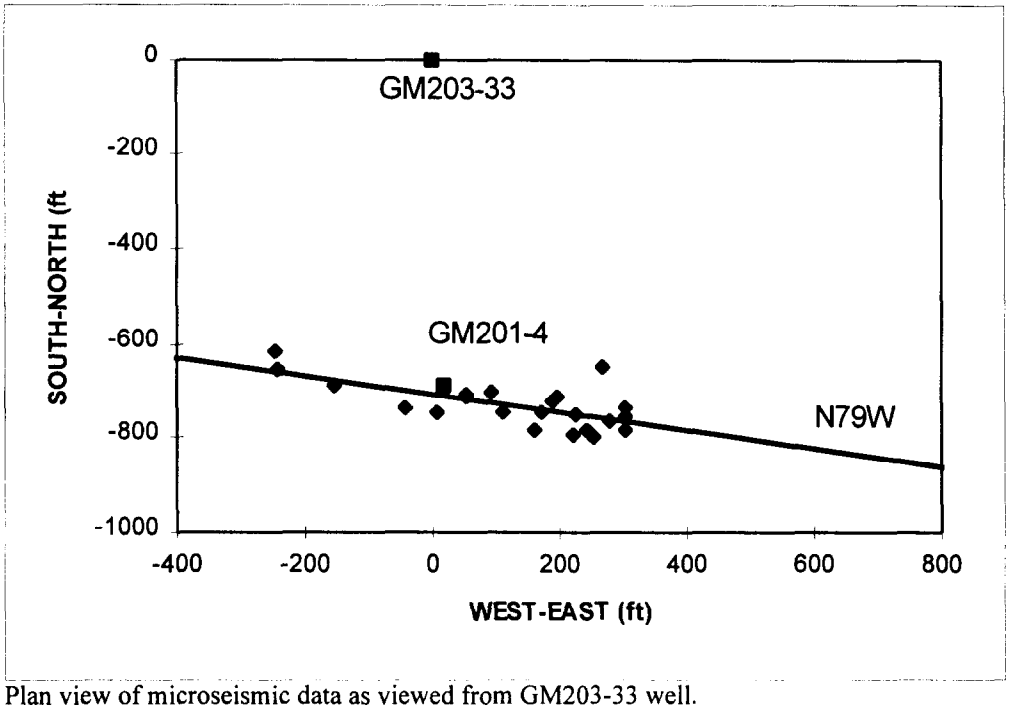

Figure 55. Plan view of microseismic data as viewed from GM203-33 well.

The side view, however, shows that the data present only a limited view of the fracture. As seen in Figure 56, the observed microseisms are primarily at or above the top perforations (perforated intervals shown as the squares on the treatment wellbore). It is possible that fracture growth is primarily upward , but there is also another explanation. Since receivers were located at 5567, 5617, 5717 and 5817 ft relative to the treatment well, there are two relatively closely spaced receivers near the top of the interval. With small microseisms, this bias in depths results in more microseisms being detected at depths where there are more receivers. This effect will be discussed in later sections.

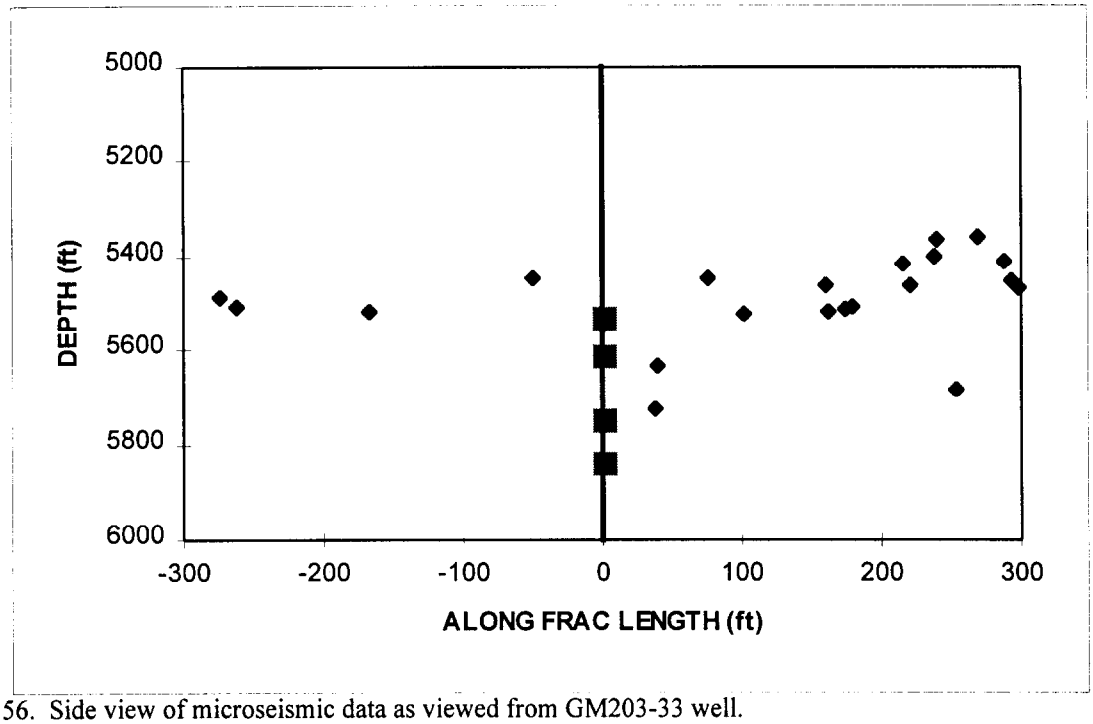

Figure 56. Side view of microseismic data as viewed from GM203-33 well.

This initial view of the microseismic data suggests that there are too few microseisms to provide anything other than an azimuth and a general tendency for the fracture to grow upward out of zone. The following sections describe how these data were obtained and some discussion of possible causes of the unusually small number of microseisms.

9.2.3 Microseismic Details

The analysis of a microseismic test involves two parts, the orientation of the receivers using perforations or some other source and the actual fracture imaging. Usually the orientation is performed first, but in this test the receiver-system problems made it impossible to orient the receivers from the MV I perforations, so instead the receivers were oriented after the test using two of the MV II perforations.

9.2.3.1 Perforations

The receiver depths and perforation depths for the MV I treatment are shown in Table 4. Note that there is a 73-ft offset between the location of the receivers in the monitor well (203-33) relative to the position in the treatment well (201-4). The lowest set of perforations is 150 ft above the top receiver and approximately 700 ft to the south of the monitor well.

Table 4 Receiver and perforation depths

RECEIVER DEPTH (203-33)	RECEIVER DEPTH (201-4)		PERFORATION DEPTH (201-4)	NUMBER OF PERFORATIONS
5640	5567		5412-14	6
5690	5617		5276-77	4
5790	5717			
5890	5817			

Figure 57 shows the traces of the deepest perforation (at 5412-14 ft) as recorded on the four-level system. Starting at the bottom, Figure 57 shows the two horizontal axes (x, y) and the vertical channel (z) for the lowest receiver and then similar data for each successively shallower receiver. This figure shows that there is an excellent response to the perforations, but the magnitude is low for 72 total grams of perforation charge. The p wave is easily visible in the figure, but the s wave is more difficult to find in this presentation (it should arrive about 1 division later).

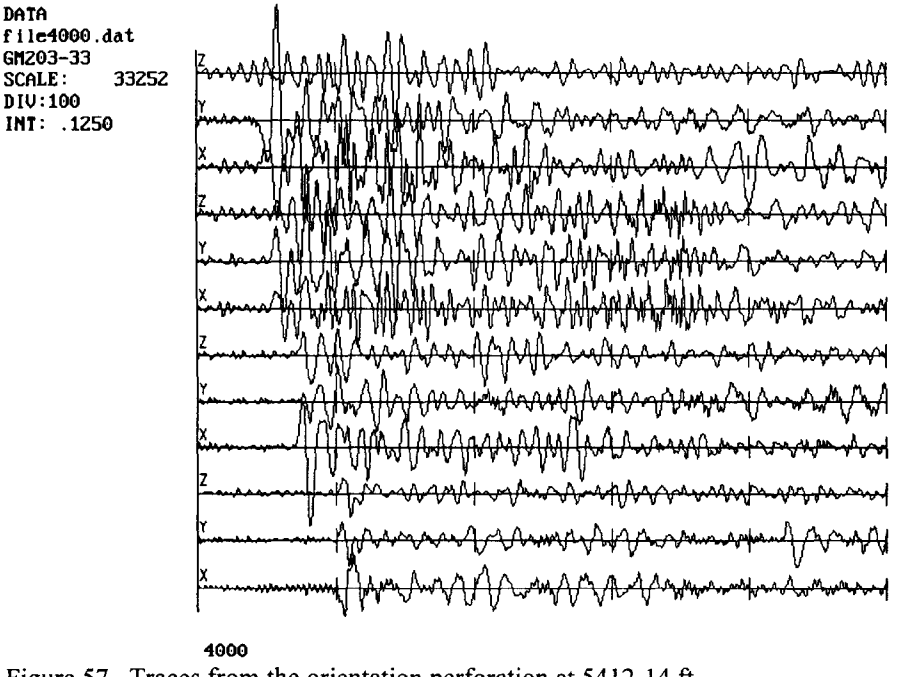

Figure 57. Traces from the orientation perforation at 5412-14 ft.

Figure 58 shows the traces from the shallowest level (5567 ft), including overlain horizontal traces (bottom plot), horizontal hodogram (top center plot), vertical hodogram (top right plot) and measured data (top left text). This figure shows that the p-wave arrival is well defined (first vertical line on lower plot) and that it is highly polarized with an orientation of -67.5° relative to the treatment well (top center hodogram plot). The vertical hodogram shows that the waves are traveling nearly horizontally (not head waves through some high velocity layer). The s-wave arrival is not entirely clear, but an s-wave is definitely present, as can be seen by the change in phase that occurs after the second vertical line on the lower plot.

The only discrepancy seen in these results is the calculated distance to the perforation (855 ft), which is significantly less than that determined by the well-deviation surveys (735 ft from the perforation to the top receiver). There could be two reasons for this discrepancy. Either the velocity factor, $V_pV_s/(V_p-V_s)$, is much lower than that measured at M-Site (22.3 ft/msec) or the s-wave arrival is in error. A velocity factor of 19 ft/msec, instead of 22 ft/msec would bring the distances into agreement, as would a 5-msec earlier s-wave arrival (which is possible here since the s-wave arrival is not particularly clear). Post-fracture examination of a dipole sonic log from the 201-4

well suggests that the 19 ft/msec velocity is probably correct (V_p=14.3 ft/msec and V_s=8.2 ft/msec), but it is not clear why the velocity structure should be so different from M-Site since both sites have the same depositional environment.

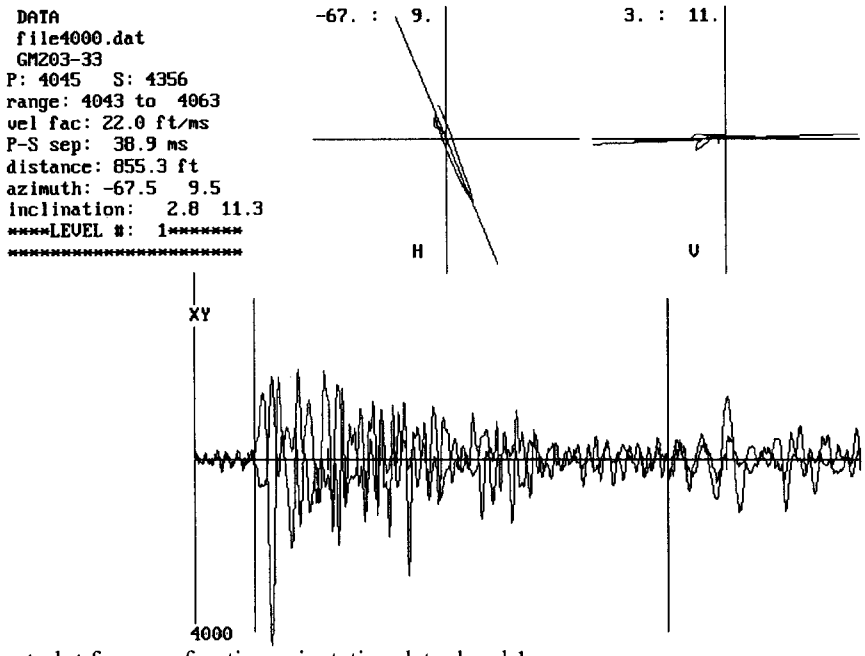

Figure 58. Resultant plot from perforation orientation data, level 1.

Similar data from level 2 are shown in Figure 59. This level has an orientation of 58.1° relative to the treatment well (each of these tools rotates differently in the wellbore, so the difference between levels 1 and 2 is not surprising). The p wave is strong with good polarization, but the s wave is again weak and difficult to use for estimating the velocity factor. Based on the arrival-time picks shown in Figure 5, a velocity factor of 18 ft/msec would be required to match the measured distance (747 ft).

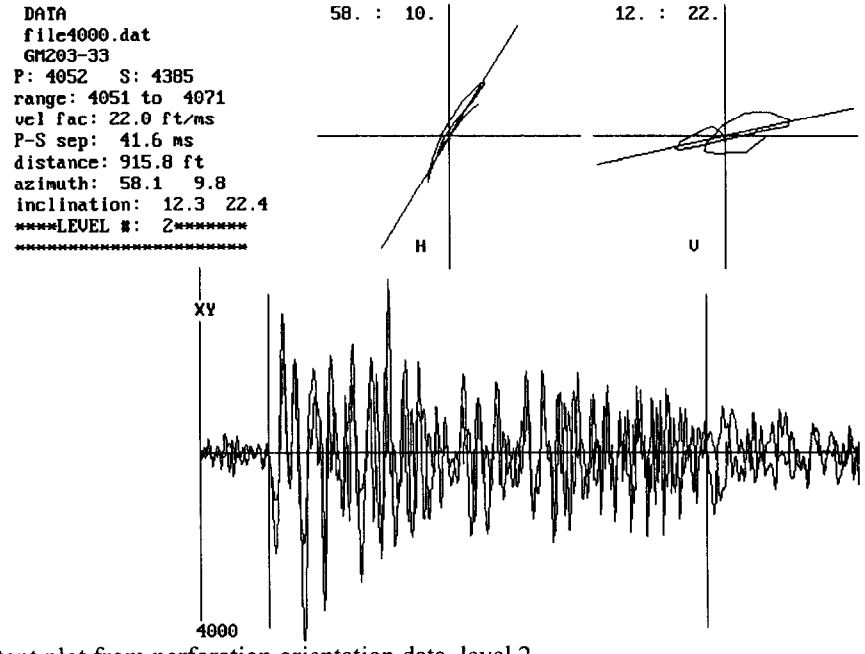

Figure 59. Resultant plot from perforation orientation data, level 2.

The same information for levels 3 and 4 are shown in Figures 60 and 61. Velocity factors of 19.9 and 20.2 would be necessary to match the actual distances to the perforation location. Based upon perforation data alone, a velocity factor of 20 appears appropriate for this location, which is not unreasonable based upon the dipole sonic data.

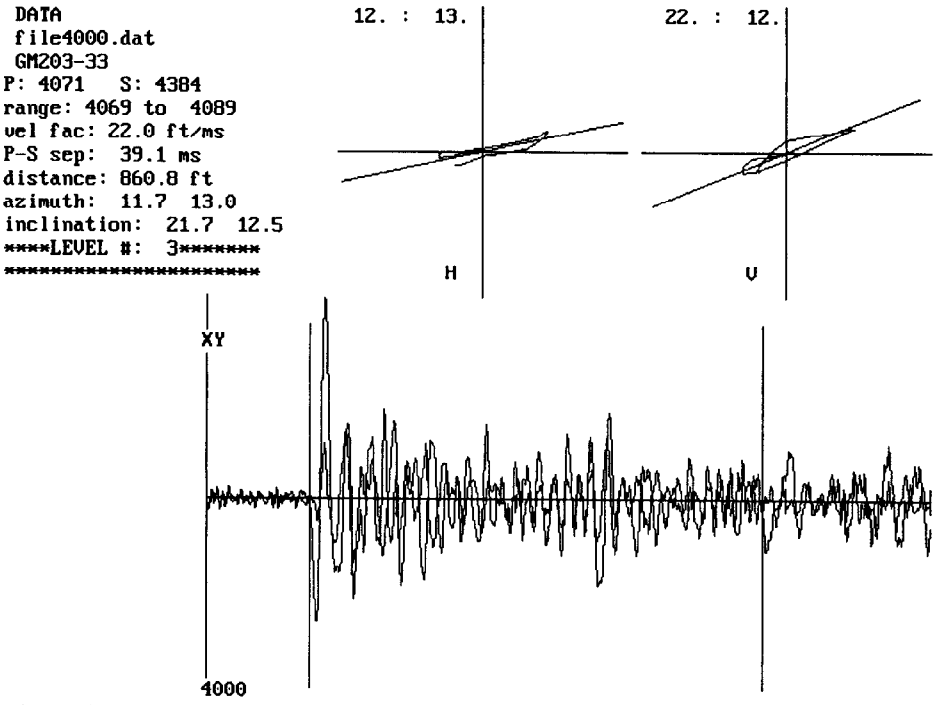

Figure 60. Resultant plot from perforation orientation data, level 3.

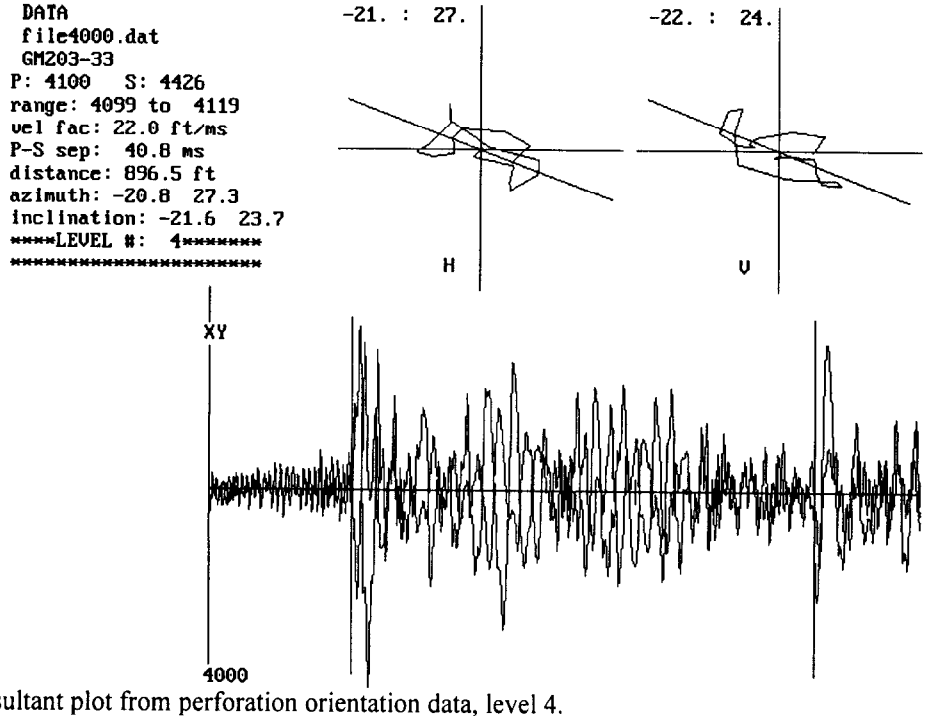

Figure 61. Resultant plot from perforation orientation data, level 4.

While the top three levels have high quality orientation hodograms, the lowest level is not well polarized and should be considered questionable for azimuth information. It was hoped that the second perforation would resolve any orientation questions, but the second perforation was barely discernible above the noise and was not used. Thus, the final parameters from the orientation data are:

velocity factor	20 ft/msec
level 1 azimuth	-67.5°
level 2 azimuth	58.1°
level 3 azimuth	11.7°
level 4 azimuth	-20.8°

From the examination of the dipole sonic log, the important parameters are:

average p-wave velocity	14.3 ft/msec
average s-wave velocity	8.2 ft/msec.

9.2.3.2 Microseisms

Figure 62 shows the traces from one of the strongest microseisms seen during the MV I fracture treatment. This microseism has a well-defined p-wave arrival (first wave, about 20% into the trace) and good s-wave arrivals on most levels (midway in the trace). It has about half the amplitude of the perforations described previously. By examining the earliest arrival traces, it is also clear that this signal is at or above the top receiver.

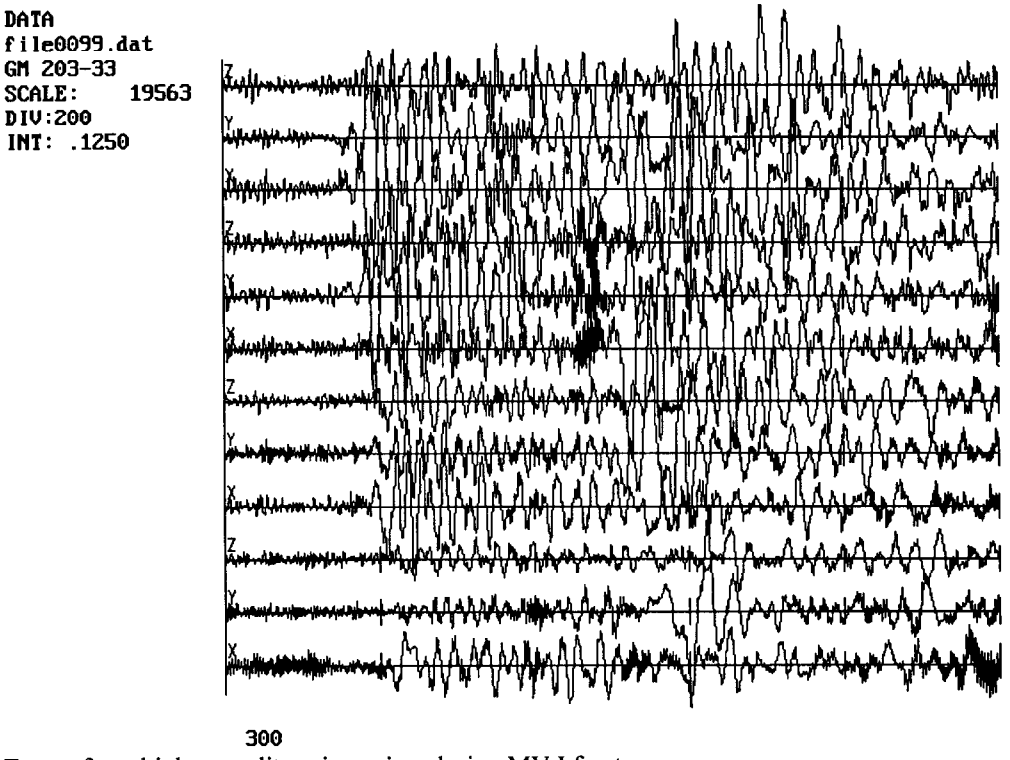

Figure 62. Traces from higher-quality microseism during MV I fracture.

Figure 63 shows a second example that is more typical of the events detected during this treatment. In this case, the s-wave arrival is relatively clear (about half way through the trace), but p waves are barely discernible relative to the noise. It is only through the phase relationships that one can be certain that there is a p wave in the data.

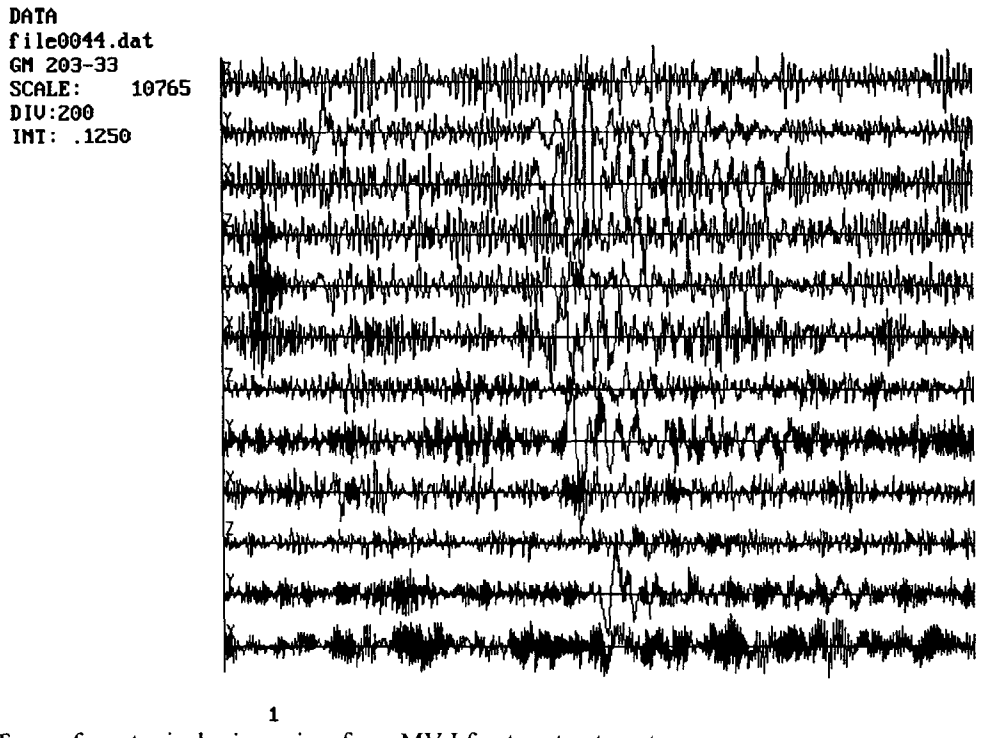

Figure 63. Traces from typical microseism from MV I fracture treatment.

Hodogram data from level 1 of the higher quality microseism are shown in Figure 64. The p-wave arrival is highly polarized and has a clear arrival time, but the s-wave arrival is uncertain and not picked here.

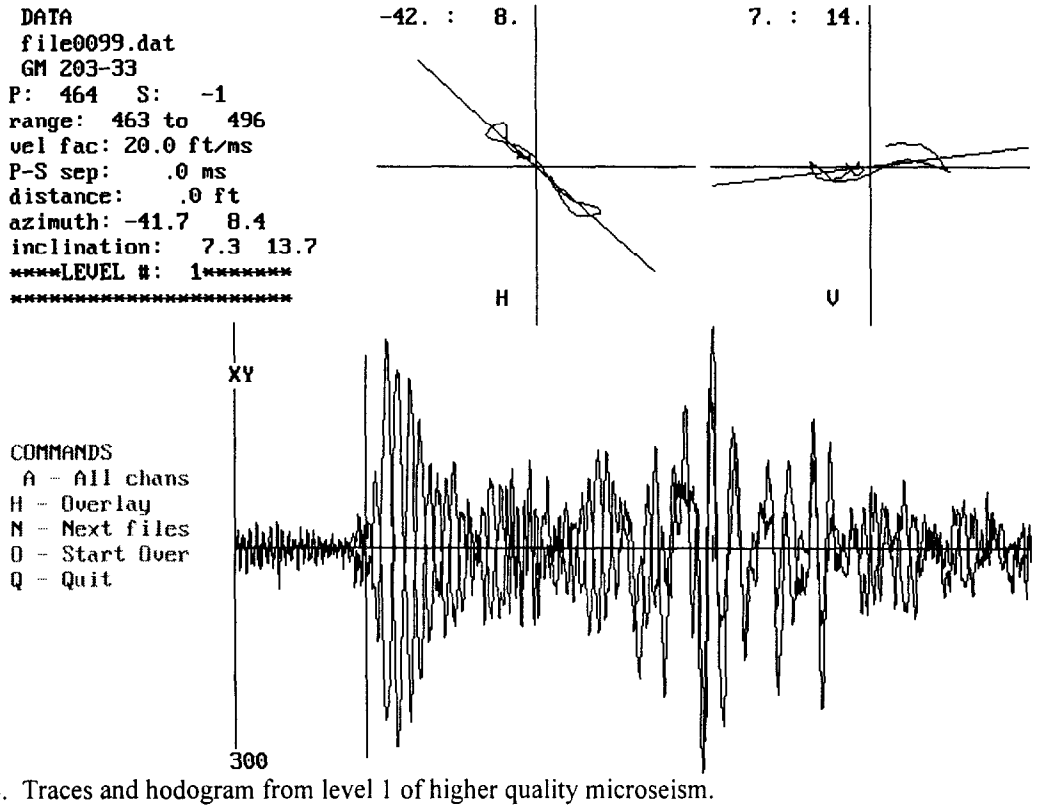

Figure 64. Traces and hodogram from level 1 of higher quality microseism.

Similar results for level 2 are shown in Figure 65. On this level, however, the s-wave arrival is clear and has been picked. The distance to this microseism is about 880 ft, based on the 20 ft/msec velocity factor.

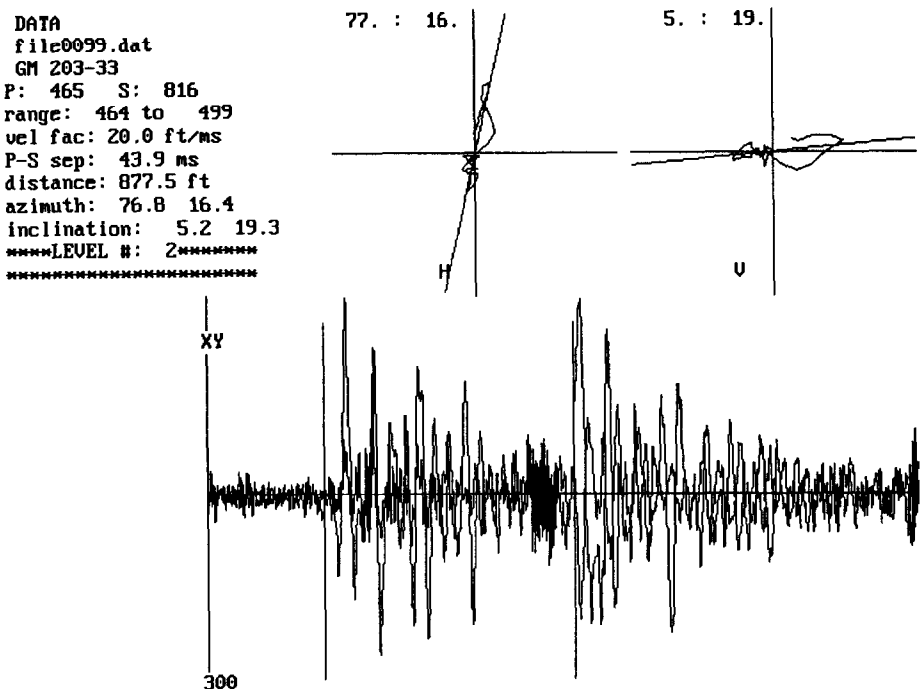

Figure 65. Traces and hodogram from level 2 of higher quality microseism.

Similar data for level 3 and level 4 are shown in Figures 66and 67. In both cases the p-wave and s-wave arrivals are relatively clear, but the p-wave hodogram for level 4 is poor and should not be used for orientation. Distances to the microseism from these levels are also around 900 ft.

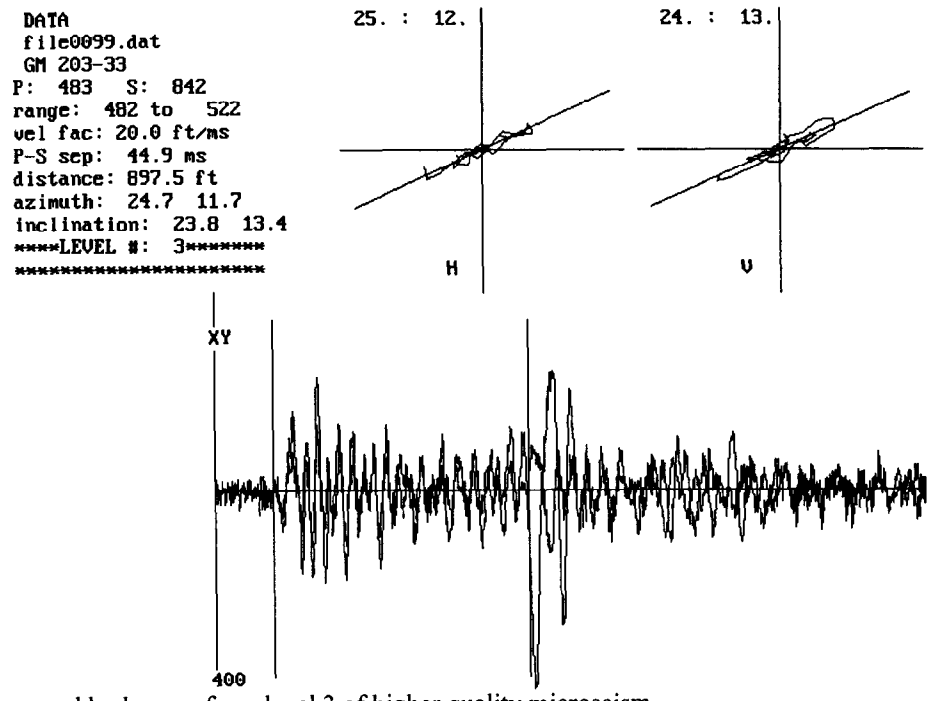

Figure 66. Traces and hodogram from level 3 of higher quality microseism.

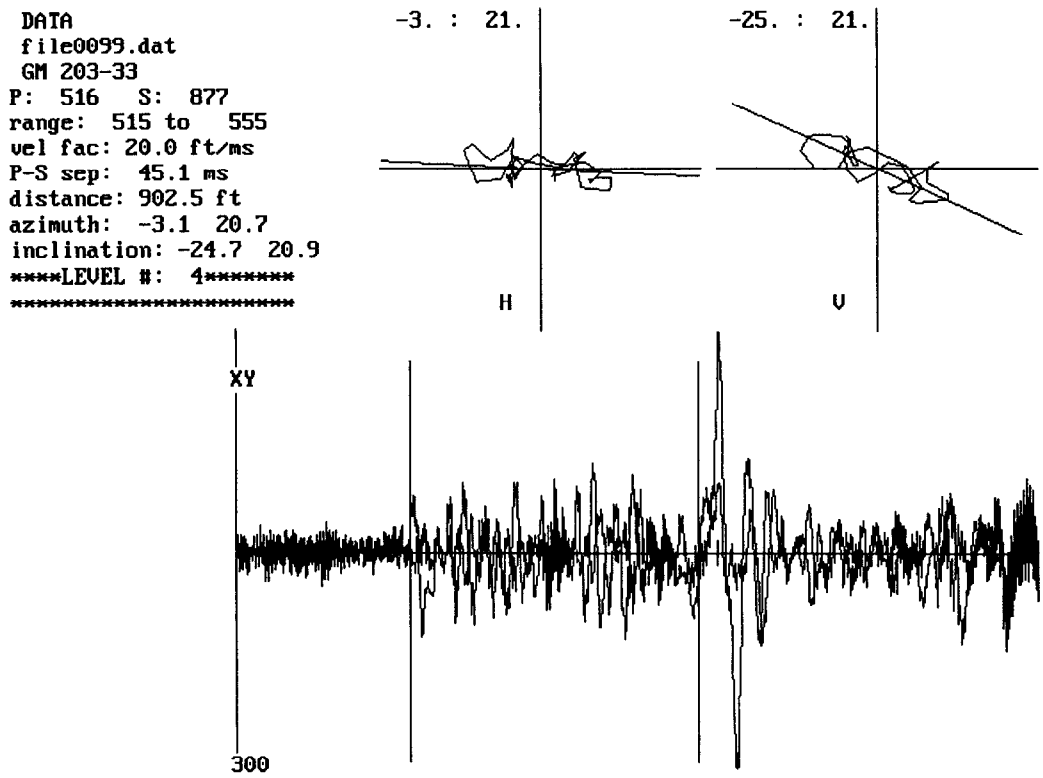

Figure 67. Traces and hodogram from level 4 of higher quality microseism.

As can be seen from the previous figures, even the largest microseisms are relatively small and may have some levels in which analysis is difficult. Many of the smaller microseisms may have observable p waves on only two levels and clear s-wave arrivals on 2 or 3 levels. Hodograms on these low-level microseisms are poor and can only be used if two or more levels show good agreement in the azimuth to the microseismic source. As a result, only about 20 microseisms were found to be of sufficient quality to attempt analysis, resulting in the data shown in Figures 55 and 56. To get these 20 microseisms, over 3000 triggered files were examined, but most were rejected as noise triggers or microseisms that were too small to analyze.

9.2.4 Discussion of Results

9.2.4.1 Low Microseismic Amplitudes

The most confusing issue associated with these tests is the absence of any large microseisms. Figure 68 shows the maximum amplitude of each of the events relative to the background noise level for this test. The amplitude scale is in bit counts of the A/D converter, so the actual magnitude is not relevant. However, only four of the events had amplitudes that compared with those seen at M-Site at a similar depth. Furthermore, this fracture injection was at least 20% greater in size than any of the injections performed at M-Site. Most analyzed microseisms at M-Site had signal-to-noise ratios of 5 and greater, compared to a typical signal-to-noise ratio here of about 3. Many of these microseisms were from 600-800 ft away, the same distance as the interwell spacing at this test.

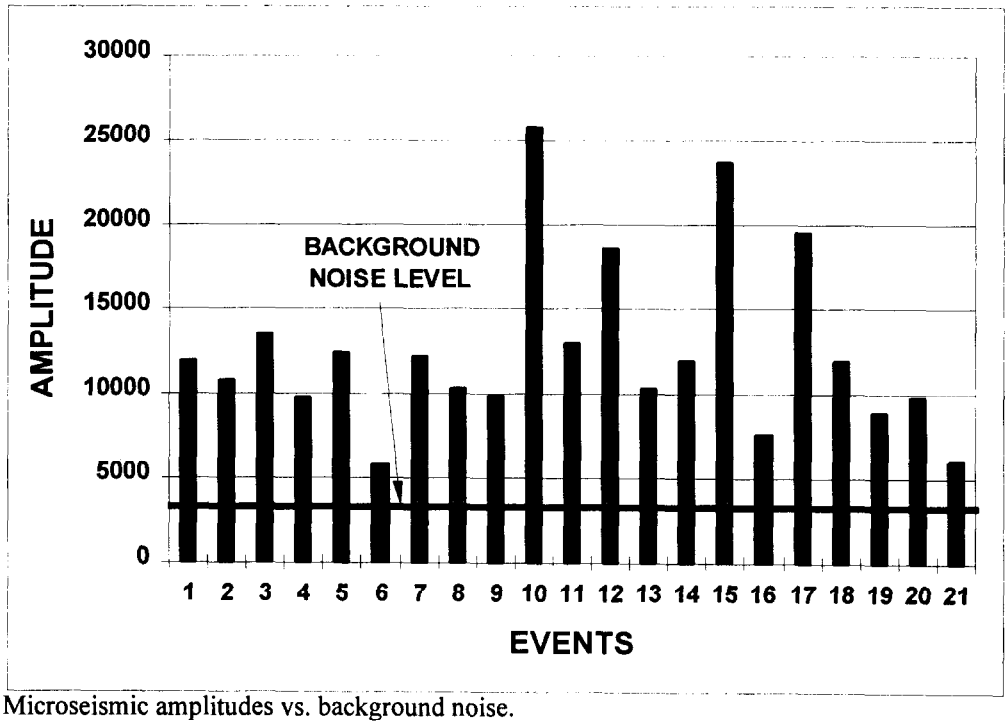

Figure 68.. Microseismic amplitudes vs. background noise.

For comparison, Figure 69 shows an example hodogram and trace plot from one of the M-Site microseisms detected at a similar distance as here. Both the p-wave arrival and the s-wave arrival are clear and have large signal-to-noise ratios.

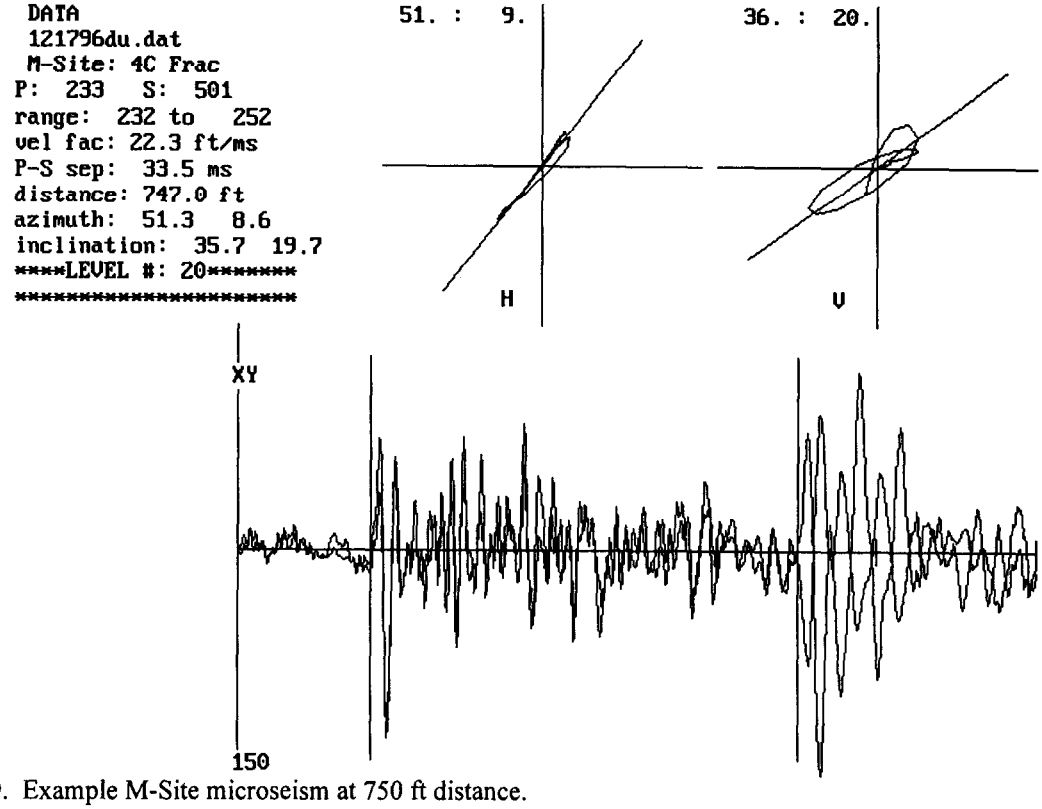

Figure 69. Example M-Site microseism at 750 ft distance.

The scarcity of large microseisms is due either to some quality of the rocks that is attenuating the microseisms or to some quality of the fracture process that is inhibiting the generation of large microseisms. Features that could attenuate, reflect, or otherwise reduce the waves traveling between the wells include faults, natural fractures, high porosity regions and high gas saturation regions. In these tight rocks, a large scale fault or a large swarm of fractures would be the most likely source of problems. Neither of these two features, however, are thought to be present in this area.

Large microseisms could be inhibited if the rocks' slippage planes are weak, effective stresses are large, or net fracture pressures are low. Most microseisms occur along pre-existing slippage planes (e.g., natural fractures, faults, bedding planes, de-watering features, etc.) when the frictional forces preventing slippage are overcome. If the slippage planes are weak, then all of the microseisms will be small amplitude because there is little energy built up before release. If the effective stresses are large or the net fracturing pressures are low, then it is not possible to generate sufficient shear stresses to overcome the frictional forces on the weakness planes. Only small or weak planes would experience slippage, thus inducing only small microseisms. Since the net pressures are relatively low (at least relative to M-Site), this explanation is a possibility.

The perforation results can provide some guidance in choosing a likely scenario. Perforation shots are very large amplitude events and can often saturate the detection system. In this test, however, the perforations were also very small (relative to the noise). Such a result suggests that the source mechanism is not the problem, but that the medium is attenuating the signals.

One other explanation exists which is related to the instrumentation itself. There have been many recent changes made to the advanced receiver system by OYO Instruments that have not been effectively relayed to those of us using this equipment. It is possible that the amplitude of the bit count has been changed by some scale factor without our knowledge. If this is the case, it could be that this particular site is actually very noisy (from production or other sources) and our difficulty stems from trying to detect microseisms (or perforations) over this high noise level. Full calibrations of the system will be made before any further tests are cunducted.

9.2.4.2 Bias Toward Upward Growth

The microseisms that were detected were clearly biased toward the upper part of the interval. While it is certainly possible that most of the activity was near the top of the fracture zone, it is also possible that the tool configuration biased the results. Figure 70 shows a schematic of the receiver and perforation locations relative to their distance apart.

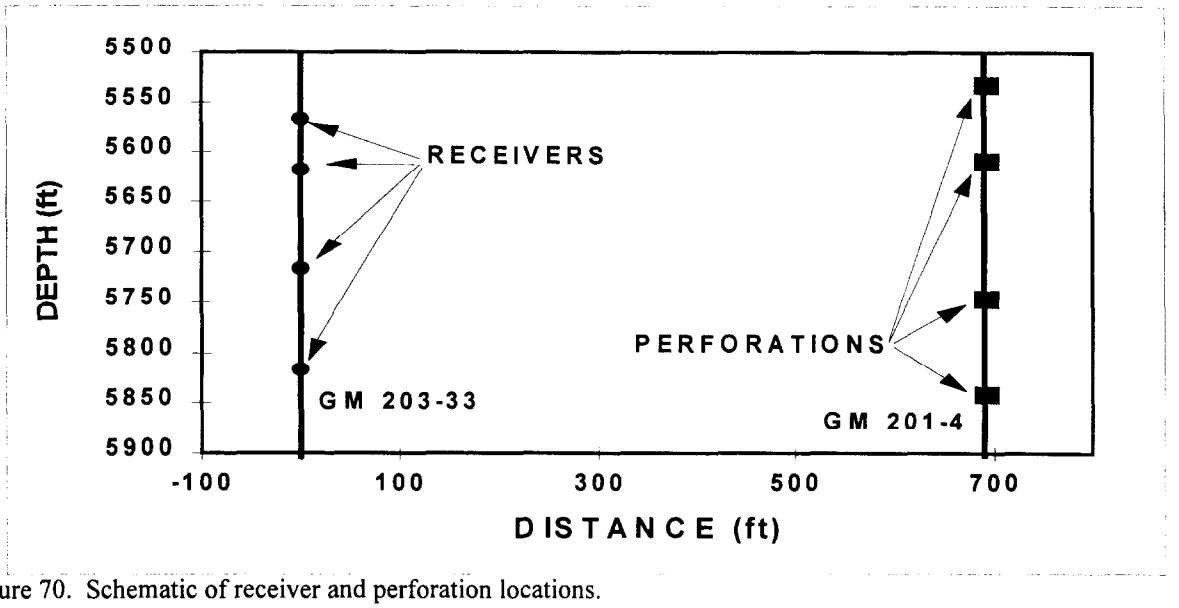

Figure 70. Schematic of receiver and perforation locations.

Because of receiver system problems, only four receivers were used and two of these had a 50-ft interconnect between them instead of the planned 100-ft interconnect. As a result, there are two relatively closely spaced receivers near the top of the interval. This placement, in itself, may not have significantly biased the results, but the triggering of microseisms requires that events occur on at least two levels. Since small microseisms are most likely to trigger on two close levels, the combination of placement and triggering offers a potential for selective detection of the microseisms.

If microseisms are large, then this spacing is immaterial and microseisms would have been detected anywhere in the interval. However, with very small microseisms, it is possible that the close spacing has worked to bias the results such that most of the analyzable microseisms are in the vicinity of the top two receivers.

9.3 Crosstimber Frontier Test

On June 24 and 25, 1997, a fracture diagnostic suitability test was conducted in the Frontier formation, Fontenelle field. The diagnostic well was the Fontenelle Federal 14-06 and the treatment well was the Fontenelle Federal 44-01. The objectives of this test were twofold:

- Determine if microseisms can be mapped at normal interwell spacing in this field.
- Determine the fracture azimuth for a full scale diagnostic test.

As this was merely a suitability test, only a single-level analog receiver was run in the 14-06 well, so there were no expectations of determining other fracture parameters (although it was a possibility that some information on length could be obtained).

Unfortunately, as given below, the results are not as clear as hoped. There is no question that many microseisms were recorded during these tests at this interwell spacing. However, most of the events were confusing, probably due to the presence of the hydraulic fracture in this well.

9.3.1 Receiver Placement

The receiver consisted of a tri-axial accelerometer array clamped in place with a piston drive system for high fidelity seismic monitoring. It was run on a Halliburton seven conductor wireline and eventually clamped in place at about 8700 ft in the 14-06 well. Prior to clamp-in, it was also tested at 8600 ft, 8645 ft, and 8730 ft to find the quietest location. This position was about 54 ft below the perforated interval in this well (8626-8646 ft) and approximately 70 ft from TD. This well had also been previously hydraulically fractured and then killed for diagnostic use, and there was little indication of any gas bubbling noise.

Figure 71 shows a plan view of the well layout and a side view of the configuration in the 14-06 well. The wells are about 978 ft apart at the surface, but deviations of the individual wells are unknown. The velocity structure in this region was taken from a sonic log obtained in the Anderson Canyon 3-17 well. In this well, the p velocity is about 11,100 ft/sec, the s wave is about 7700 ft/sec and the velocity factor (V_pV_s/V_p-V_s) is about 25 ft/msec.

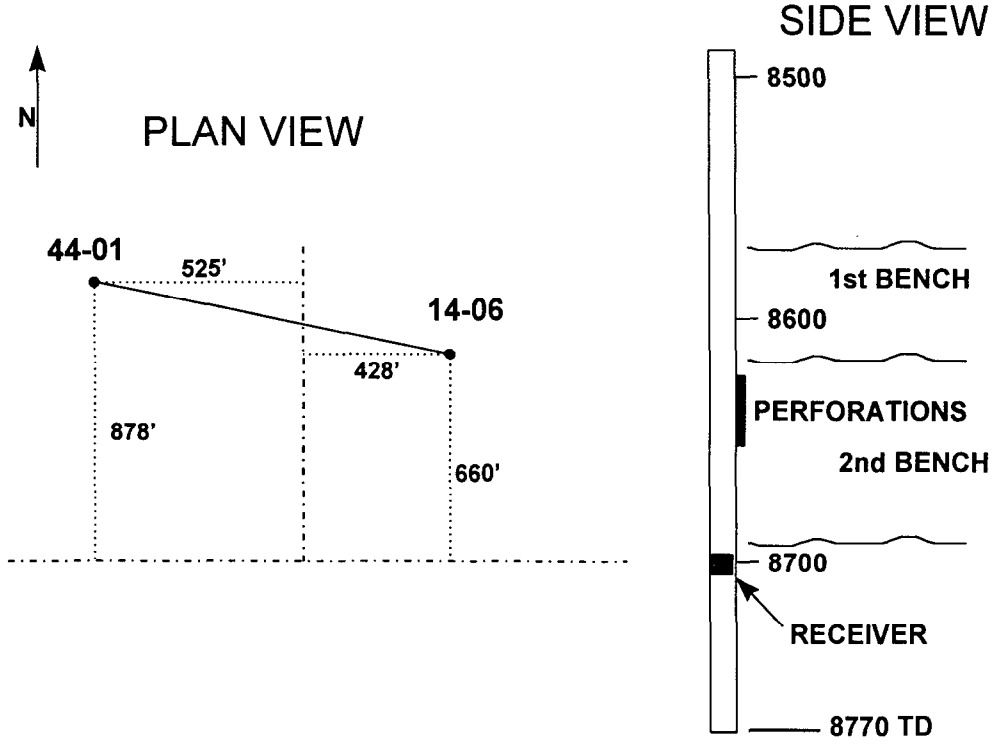

Figure 71. Well layout and receiver placement in the 14-06 well.

9.3.2 Perforations

After clamping, four perforation shots in the 44-01 well were monitored with the seismic receiver. There was also an attempt to capture the exact time of the perforation (for formation velocity) using the firing signal as a time stamp, as well as a geophone attached to the perforation gun. For some unknown reason, the perforations were not easily detected and could not be directly correlated with the time stamp. No perforation events were found for the second and fourth perforations. An event, most likely the perforation, was observed at a time relatively close to the time stamp of the first perforation shot and this event is treated as the perforation for this analysis. Another event, possibly the third perforation, was detected in the general time frame of the third perforation, but was not directly correlatable with any time stamp (which could occur if there was a false trigger).

Figure 72 shows a data summary of the event associated with the first perforation shot. This figure shows the two horizontal traces on the bottom plot, a horizontal hodogram plot in the top center, a vertical hodogram plot in the top right, and appropriate data in the top left section. The amplitude of this event is relatively small with a signal-to-noise ratio of about 6:1. The top center plot shows that the event is well polarized with an incident azimuth of 33° relative to the x axis of the receiver. Assuming that this is the perforation in the 44-01 well, then the absolute azimuth of the x axis is 44° west of north. Note also in the vertical hodogram plot that the incident wave is coming from either above or below, probably traveling mostly in the high-velocity sandstone located above. There appears to be a later wave which could possibly be the s wave. If it is the s wave, then this event only locates at 550 ft from the receiver well, which could only be possible if the wells are more deviated than expected or the velocity structure is much different than expected from the sonic log. As will be seen later, this second wave is not the s wave.

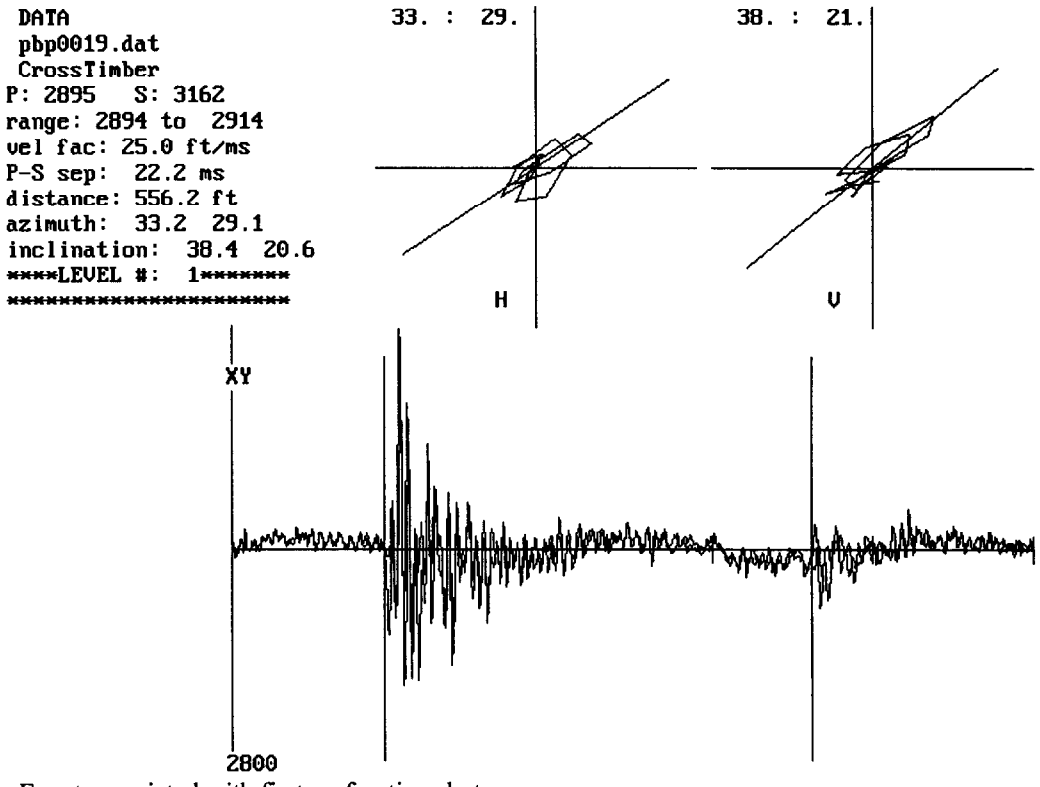

Figure 72. Event associated with first perforation shot.

Figure 73 shows the possible third perforation. This event plots out at the same azimuth and inclination as the event associated with perforation number one, so it is quite likely that this is the perforation. Note also that there is a weak second wave (chosen as an s wave here) that comes in about 22 msec behind the first event. As will be discussed later, almost all signals (microseisms and perforations) have a second wave that appears about 22 msec

after the primary wave. It is unlikely that this wave is the s wave, as the constant timing is improbable and the phase and frequency relationships typical of s waves are not seen in these data.

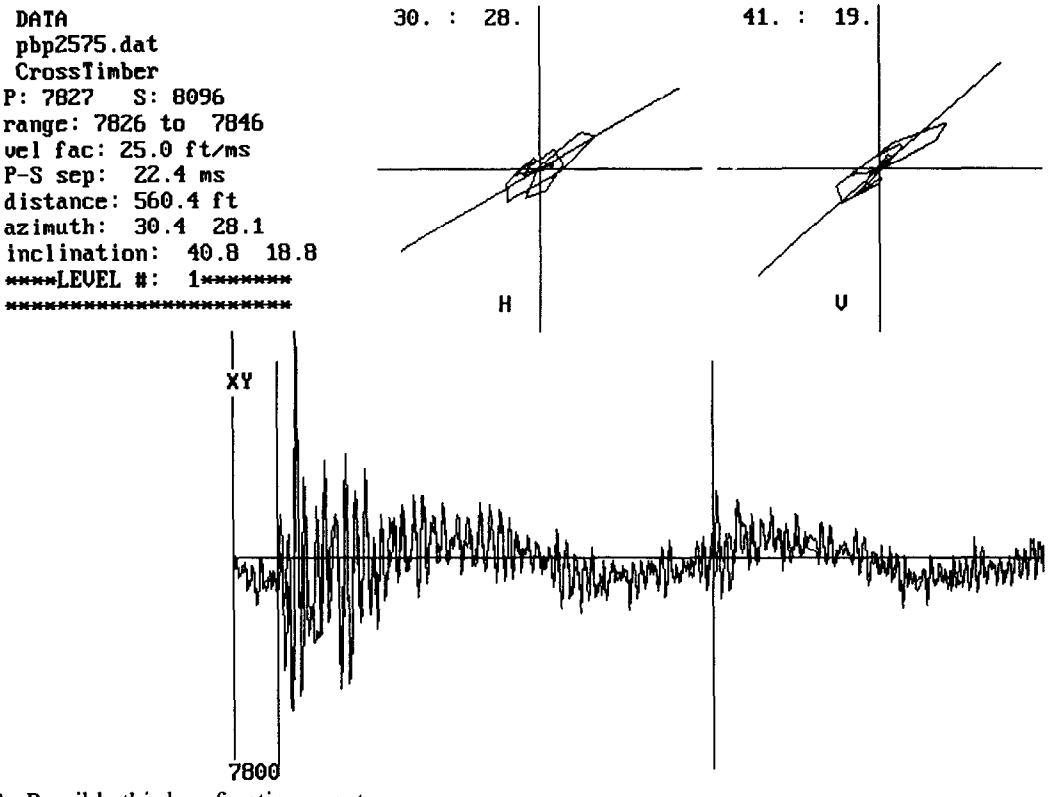

Figure 73. Possible third perforation event.

In summary, there are two events which are logically associated with the perforations, both of which provide the same orientation for the receiver. However, no true s wave was observed and no events were observed for the second and fourth perforation shots. It is not clear why the perforation shot were not easily seen, given that fact that each perforation shot was composed of several perforations. There are two possible explanations that we can envision. First, it is possible that the 0° phase perforations were pointing the wrong direction, i.e., 90° off from the 14-06 azimuth. If this occurred, the 14-06 well would be in the null of the p-wave radiation pattern. In the past we have mainly used 90°or 120° phasing, but there were also many tests at M-Site where single perforation shots were used and these were always seen from all monitor wells. A second explanation is that the hydraulic fracture in the 14-06 is affecting the incident waves in some unknown manner. As will be seen in the next section, this is a credible hypothesis based upon the microseismic data.

9.3.3 Microseismic Results

The microseismic monitoring consisted of continuous recording of the microseisms from the minifrac on the afternoon of June 24 and the main fracture on the morning of June 25. In both cases, full recording was made to a DAT tape while an A/D system on a computer was also creating digitized files of the data in SEG2 format. After each test, these digitized files were then processed through an event detection routine to obtain events with amplitudes greater than about 2.5:1. These events were subsequently analyzed individually to determine p and s arrivals and hodogram information. During the minifracs, 145 events were detected, while 318 were detected during the main treatment. From all of these events, 38 analyzable microseisms were found during the minifrac and 123 analyzable microseisms were found during the main stimulation.

Figure 74 shows a histogram of the microseisms during the minifrac and Figure 75 shows a similar plot for the main fracture treatment. Also shown is the background level of events as determined during monitoring around the time that perforations were being shot. Each bar shows the number of events in a ten minute window compared to the average background level of just under 5 events. While Figure 74 may not show enough events to convincingly demonstrate that the microseisms are associated with the fracture injections, the level of microseisms detected during the much larger propped stimulation (Figure 75) clearly indicate that microseismicity increased dramatically during injection.

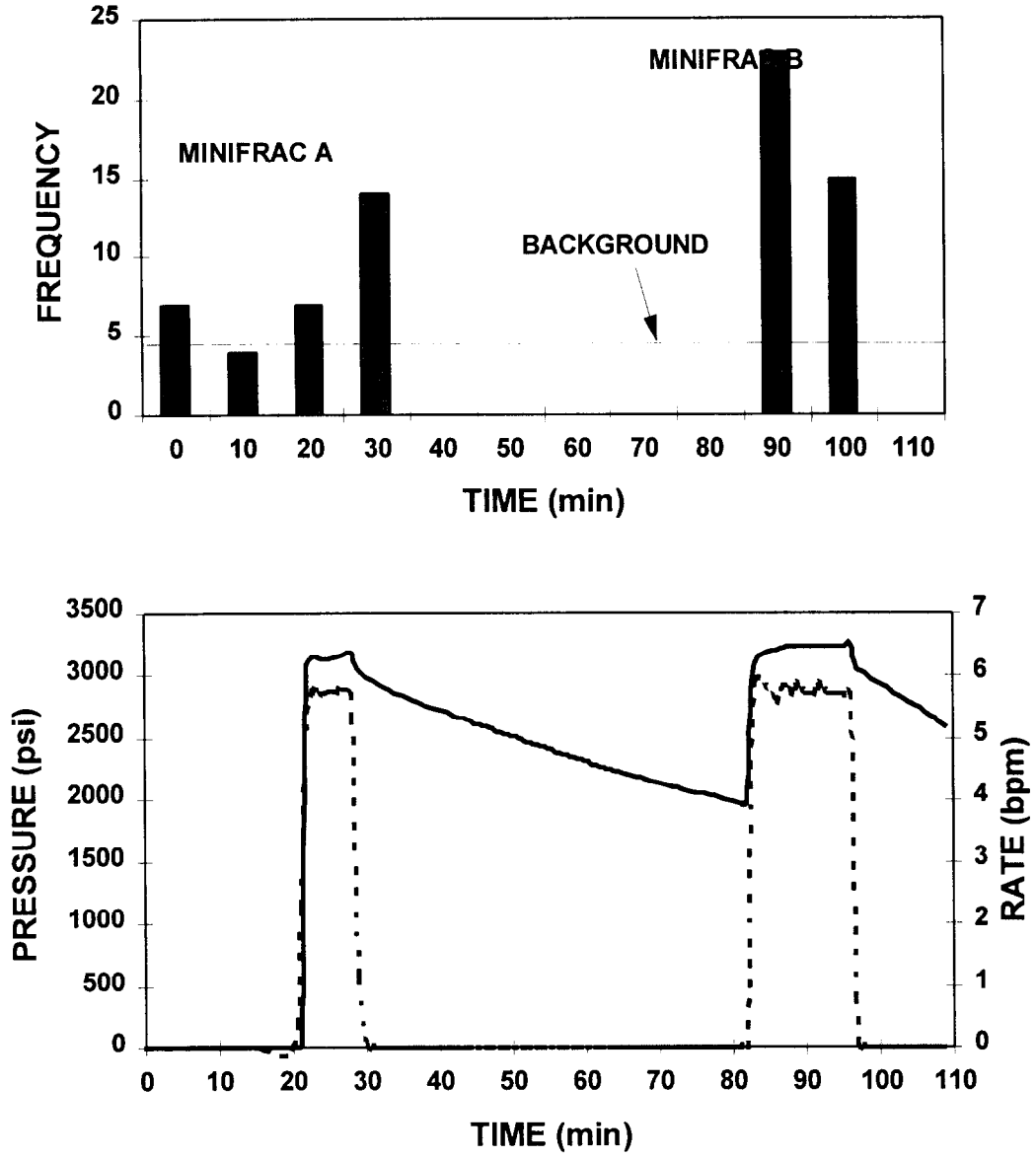

Figure 74. Histogram of events during minifrac correlated with pressure (solid line) and rate (dotted line).

In addition to the number of events detected, there was also an increase in the magnitude of the events. Background events were typically at signal-to-noise levels of 3:1 - 4:1. During the minifrac, levels increased to 10:1 with many events in the 6:1 range. During the main fracture treatment, levels increased to 25:1 with many events in the 6:1 to 15:1 range.

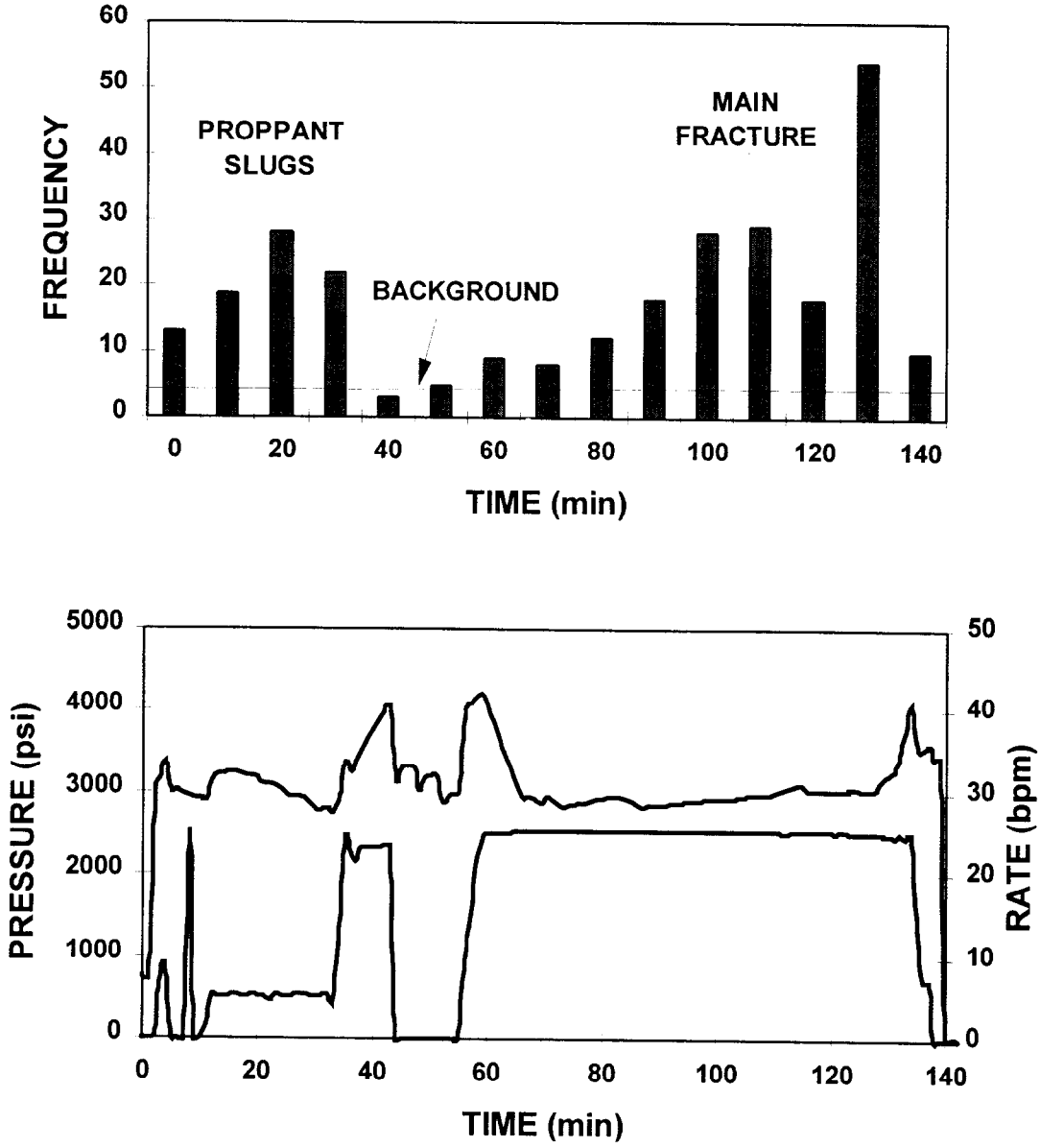

Figure 75. Histogram of events during main fracture treatment correleated with pressure and rate (bottom line).

Unfortunately, while the number and size of of the events increased, the interpretation became more difficult. Figure 76 shows an example event that is typical of 95% of the recorded microseisms. This event has a signal-to-noise ratio that is about 11:1, is highly polarized, and shows a second wave coming in at about 22 msec after the p wave. Like the perforations it is also coming in at an azimuth of 30°and at a large vertical angle.

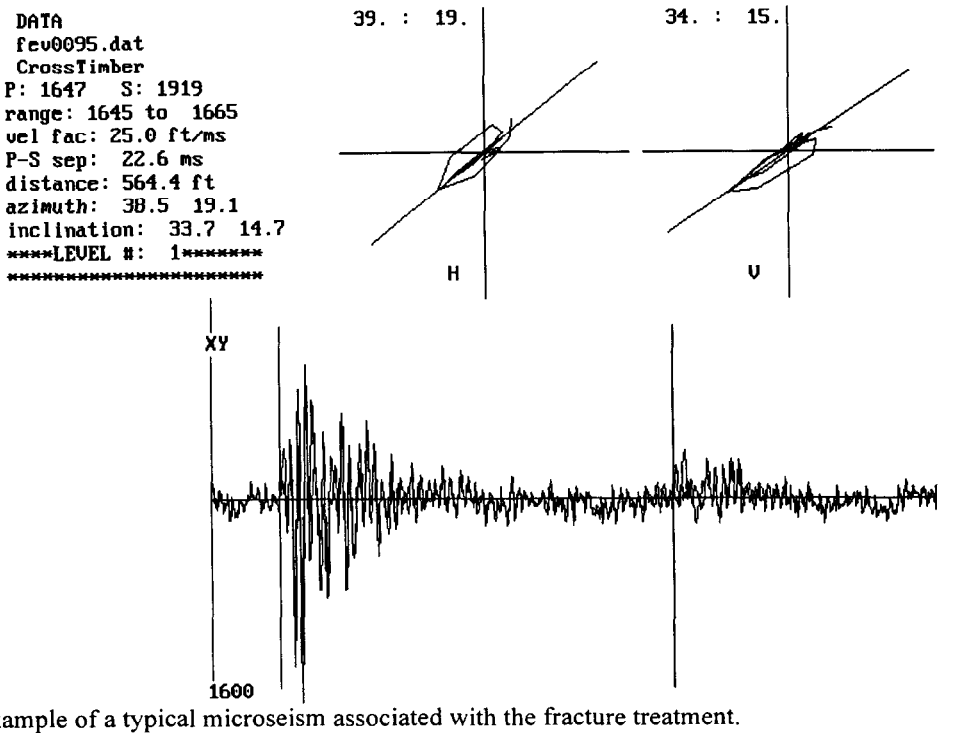

Figure 76. Example of a typical microseism associated with the fracture treatment.

Figure 77 shows another similar event, this one with a signal-to-noise ratio of about 18:1 and a much clearer secondary wave. The azimuth for this event is directed 10°different than the perforations (20°) and also has a large vertical angle. As in previous events, the second wave appears about 22 msec after the first wave.

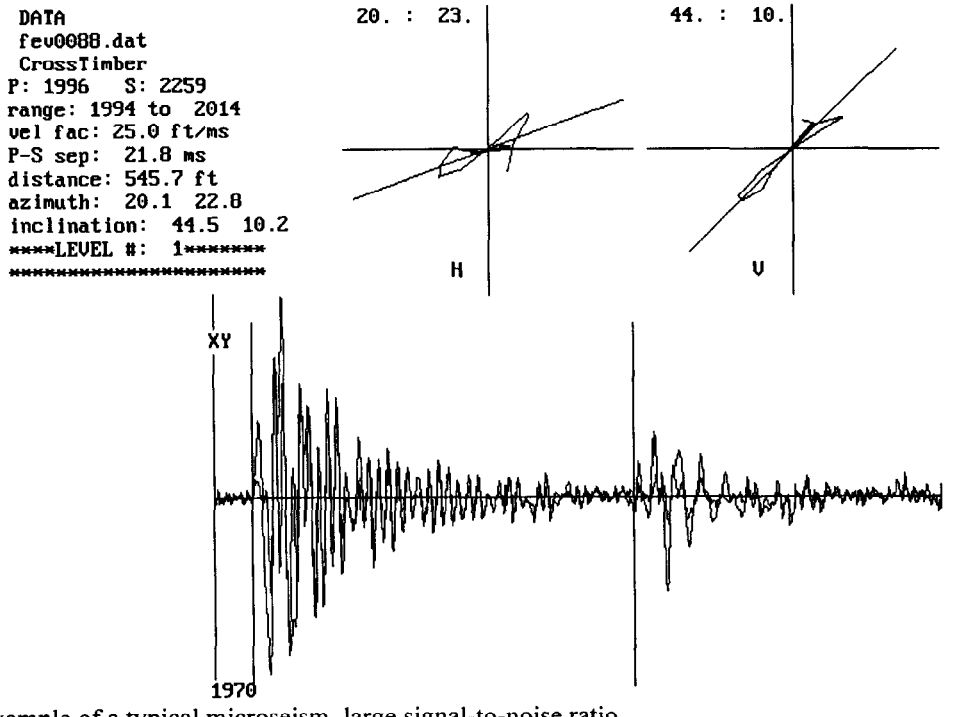

Figure 77. Example of a typical microseism, large signal-to-noise ratio.

As noted previously, about 95% of the events have a secondary wave (initially taken to be the s wave) which appears about 22 msec after the first wave. If all of the microseisms are plotted out, they appear to occur in a radial arc about 550 ft from the diagnostic well, as shown in Figure 78. This is obviously not a true representation of the fracture and secondary interpretations of the data are needed. Since the 22 msec time interval between the two waves is so consistent, it is most likely due to some feature of the diagnostic well. A 22 msec interval is consistent with a tube wave traveling a total distance of 110 ft, or a one way distance of 55 ft. Since this is approximately the distance from the receiver to TD (recall also that the receiver depth is only approximate), it suggests that the second wave is a tube wave reflecting off the bottom of the well. If this is the case, then all of the points in the radial arc are meaningless.

In some of the larger microseisms there was a third wave which appeared and this wave was 44 msec behind the first wave and plots out to about 1100 ft away. Three of these points are shown in Figure 78, but these are most likely the second reflection of the tube wave, after it bounced off the large diameter receiver and back towards the bottom again. Thus, all that we are left with are a few microseisms that have a wave appearing earlier than the tube wave, of which there are 11, and one microseism which locates well past the tube wave distance (see Figure 8). Unfortunately, these events are probably associated with the hydraulic fracture in the 14-06 well, probably because of the changes in the stress field due to the fracturing of the 44-01 well. These data are relatively scattered, but they suggest that the hydraulic fracture in well 14-06 is oriented just north of west.

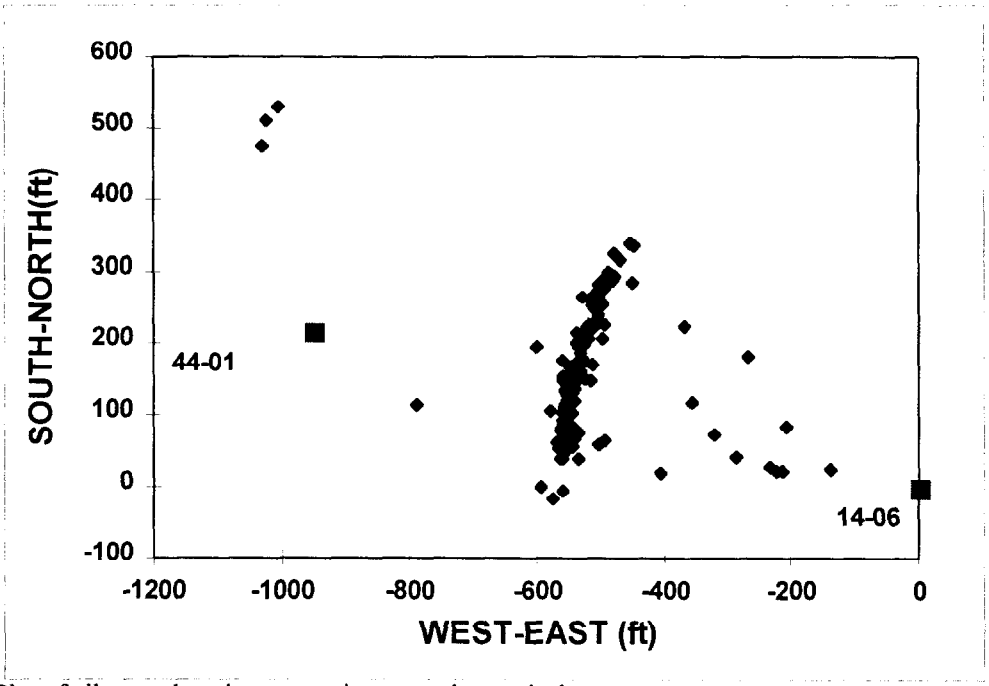

Figure 78. Plot of all event locations assuming second wave is the s wave.

Given that the second wave is not the s wave, then the 95% of the events that have this feature do not have any observable s wave and so their distance cannot be determined. The only way to analyze such data is to use the hodogram information (directionality) and make some geometrical arguments, although these are often tenuous. Figure 79 shows the angular geometry associated with all the events from these tests along with some extrapolated fracture positions. If we assume that we would have seen all microseisms associated with the fracture (even from the far wing), then two rays can be drawn from the 14-06 well that encompass the direction to all microseisms (dashed lines). If one assumes that both wings are the same length (admittedly, a questionable assumption), then many lines can be drawn through the well, but only one will intersect both rays. As shown in the figure, a fracture which is directed north of east would fit the geometry, while any others would pass over or not reach the rays.

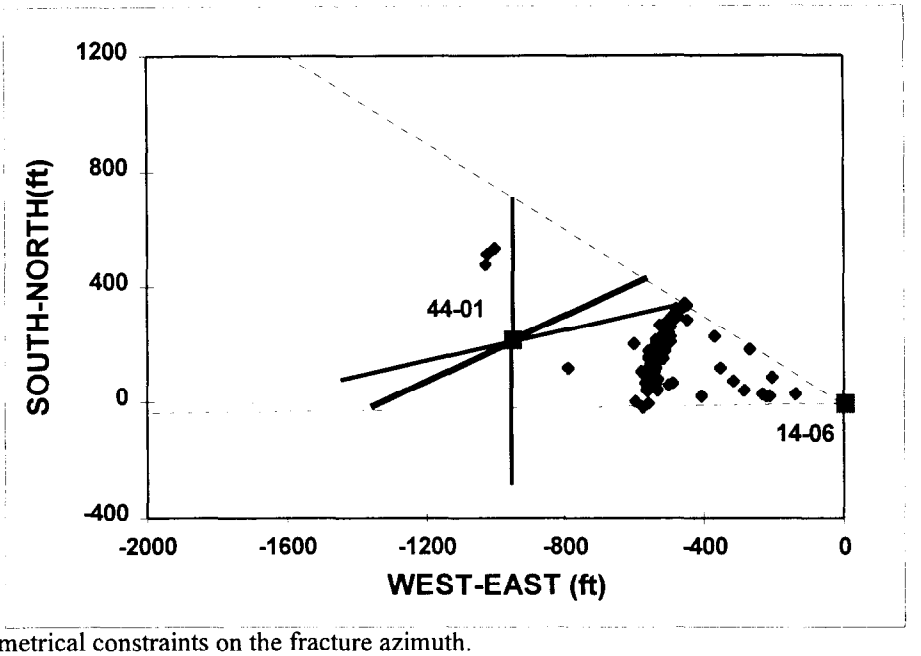

Figure 79. Geometrical constraints on the fracture azimuth.

Perhaps a more compelling argument for an approximately east-west fracture azimuth is the fact that something extinguished all of the s waves from the fracture in the 44-01 well. The most likely feature to do this is the pre-existing fracture in the 14-06 well, which could only affect the s waves if it was in between the two wells. It would not be in a position to interfere if the hydraulic fracture was north-south, so a logical conclusion is that it must be directed in some approximately east-west orientation.

As far as the remaining few microseisms, Figure 80 shows an example of a microseism which apparently has a good s wave. This event has an azimuth which is 18° different from the perforations and a p-s time separation much less than 22 msec. As noted earlier, this microseism is probably associated with the pre-existing fracture in the 14-06 well and is due to the increased stress from the nearby fracture.

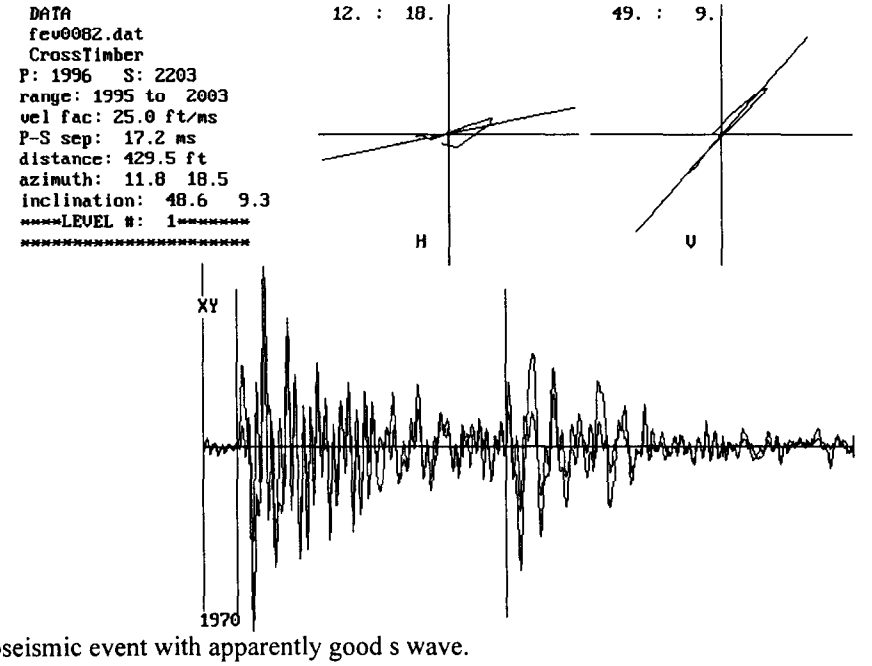

Figure 80. Microseismic event with apparently good s wave.

9.3.4 Discussion And Conclusions

There is a considerable amount of uncertainty associated with all aspects of the tests. Those factors which are most important are:

- What if the perforation events were not the actual perforations?
- If some pre-existing feature was perturbing the s waves, is there any certainty that we actually saw a p wave?
- What do these results mean for a full five-level diagnostic test?
- What is the most likely azimuth?

Even if the events which we interpreted as perforations were some other spurious events, the data would be little changed. Using the direction of the first 10 or 20 microseisms as a best guess direction to the 44-01 well, we would arrive at nearly the same perforation orientation. Thus, the uncertainty in the perforations has little effect on any measured microseism. However, it still is important because it is not clear why the perforations were so small and difficult to detect. If there is some effect due to the pre-existing hydraulic fracture in the monitor well, it has important implications for future work.

For the s waves, there are many features within the earth that could stop their transmission, as lateral stiffness (a finite shear modulus) is required to propagate shear waves. P waves, on the other hand, can be transmitted through fluid filled cracks or voids, although reflections and refractions could alter the waveform characteristics. Thus, it is highly probable that a pre-existing inter-well feature could extinguish the s waves and allow p-wave propagation. In fact, such a mechanism is the basis for a seismic fracture diagnostic technique called shear-wave shadowing. One other possibility is that the wave we are recording is the s wave and the p wave is too small to be seen. Based on all of the microseisms we have ever observed, however, this is not likely because of the clear polarization of our microseisms. P waves can remain polarized for many cycles, but s waves typically break out at a different orientation and then show little coherency in their polarizations. In our case, the waves remain polarized for 5-10 cycles and are most likely the p waves.

Although these results are not as clear as hoped, it is also a good demonstration of why we have chosen to use a multi-level array for microseismic testing. Single-well results can often lead to an ambiguous map, as found in this test. With a 5-level array, we could have triangulated on the p-wave arrival times to obtain the distance, and we would also have been able to look through, down, and up, possibly avoiding the interfering effects of the pre-existing fracture on one or more levels. The fact that many microseisms were seen at a distance of nearly 1000 ft is very encouraging for future work in the Frontier formation, but care must be taken when re-entering old wells.

The azimuth of the fracture is still in question, but all evidence points to an east-west direction. If the few close microseisms are associated with the 14-06 hydraulic fracture, then its orientation is approximately east-west. Using geometric constraints on just the directionality of the microseisms also suggests that the hydraulic fracture is east-west, although such arguments would have it about 30° north of east (absolute azimuth of N60°E). Finally, if the pre-existing hydraulic fracture in the 14-06 well is responsible for extinguishing the s waves, then the fracture must be oriented in a generally east-west direction. These results are also consistent with the geologic structure (nearby western overthrust) which would suggest an east-west orientation with some possible modification on the Moxa arch.

9.4 Chevron Packenham Test

During the week of October 13, 1997, a field test of the multi-level diagnostic system was attempted in the Chevron Packenham field in west Texas. As seen in Figure 81, the fracture and treatment wells were separated by a distance of 1685 ft at depth. The purpose of this test was to determine if fractures created in the Wolfcamp formation could be microseismically imaged at these typical interwell distances.

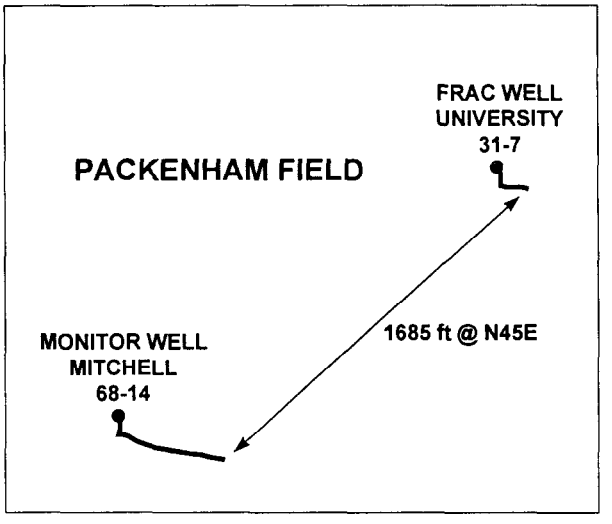

Figure 81. Plan view of well layout for Packenham diagnostic test.

The Packenham test was the first test of the receiver system after purchase of the equipment from OYO Geospace, Inc., who previously had been leasing the tools. Unfortunately, two of the tools had failures in the motor shaft seals and needed to be pulled from the well. The final configuration of the receivers is shown in Figure 82, with a three receiver geometry straddling the Wolfcamp.

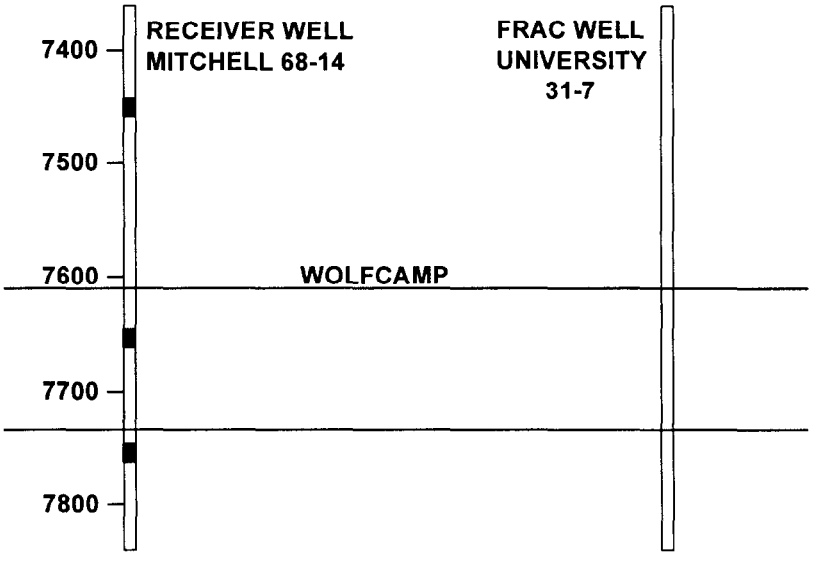

Figure 82. Side view of wellbore and receiver layout for Packenham diagnostic test.

The tools were inserted and clamped in place on October 15, 1997 and some perforations were shot in the University 31-7 well. Initially, 10 small perforations were run through tubing and fired at the same time. These

perforations could not be seen with the receivers. We tried again using 3.2 gm perforations in three sets (1, 2 & 4), but these could not be seen either. However, the receivers did monitor some background microseismic activity during October 15 and into the 16th. The fracture treatment was conducted on October 16th, consisting of 300,000 lbs of sand and 1100 bbls of CO_2 foam. During the fracture treatment, no microseisms were observed in the monitor well on any receivers. The full data set has been recorded on tape and will be played back when repairs are made to the data acquisition system (it crashed during the initial playback of the data), but we are not very hopeful that anything can be obtained.

The reason for the inability to detect microseisms is unclear, but is probably due to attenuation characteristics of the Wolfcamp or some intervening feature (e.g., a fault) which did not permit event energy to be transmitted between wells. Clearly, 1600-ft spacing is too great for fracture monitoring at this field.

9.5 Carthage Cotton Valley Diagnostic Experiment

The Carthage diagnostic experiment was an industry consortium test of microseismic fracture diagnostics in the Cotton Valley formation. Three fracture experiments were conducted between 8000 and 10,000 ft using diagnostic information obtained from two monitoring wells. However, because of problems in installing one of the monitor wells, the deepest fracture experiment essentially had microseismic data from a single monitor well. The two shallower injections had microseismic data in both monitor wells and could be accurately analyzed using the ARCO two-well approach.

With only single-well information available, there was some question whether the consortium Taylor-sand analysis was accurate. To check the consortium results, the Taylor sand fracture was re-analyzed using particle-motion information to locate the events in 3-D space.

In addition to the Taylor sand re-analysis, the microseismic data obtained in the shallowest experiment provided a data set from which to

- check geophone data compared to accelerometers
- extract a 5-level data set from which SMART5 could be used to analyze the data, and
- get microseismic information from a new reservoir and basin.

This extraction analysis was started in late 1997.

9.5.1 Single-Well Reanalysis of Taylor Sand Fracture

The objective of this re-analysis was to examine the microseismic data from the Taylor sand hydraulic fracture injections[1] using a different methodology than that provided by ARCO.[2] The ARCO approach typically uses two-well data so that only arrival time information are needed to locate microseismic origins. In the Taylor sand injections (perforated interval: 9620-9640), data were obtained in only one well (CGU-22-09). To locate the points, ARCO assumed a fracture azimuth and located microseisms near that azimuth line. This is a reasonable approach, given the good azimuth information from the two higher injections where two-well data were available, but there is a small possibility that some unusual behavior might have occurred which would not be observed if the azimuth were assumed.

This re-analysis uses a single-well approach where p-wave particle motion is used to determine the azimuthal direction to the microseismic origin and p-wave and s-wave arrivals are used to determine the distance and the elevation of the microseism. The drawback of this method is that high quality p-waves must be obtained to get good azimuthal information. As a result, this approach cannot "see" as far as the ARCO approach, but should at least confirm the behavior on the near wing.

It was originally intended that data be extracted to produce an equivalent 5-level system (e.g., analogous to that used in the GRI M-Site project) that would mimic the measured response if a 5-level wireline array were employed in a single well. As will be seen, the data quality (at least in the Taylor sand) are not sufficient to allow a suitable 5-level system to be extracted, and all usable levels were ultimately examined to provide an adequate analysis.

9.5.1.1 Single-Well Approach

The single-well approach uses data from a single vertical array of tri-axial receivers to locate microseisms. It requires that relatively clear p waves be detected, as the particle motion of the p-waves is used to determine the azimuthal direction to the microseism. Thus, the assumption is that the particle motion is in the direction of travel of the wave and it points directly back to the source, irrespective of any layering or heterogeneities. The distance to the microseism and its elevation are calculated using a joint p-wave and s-wave regression of the distance equations, assuming constant p-wave and s-wave velocities throughout the medium. However, a more detailed layered analysis can also be performed if the data are of sufficiently high quality that advanced analyses would provide more accurate results.

To perform the analysis, it is necessary that the receivers be oriented and that both x and y (the two horizontal) geophones be functioning and amplitude-balanced on numerous levels. Hodograms of the p-wave particle motion over 1-2 cycles are performed to extract the azimuth at each level. Numerous levels must be used because individual hodograms may be in error by several degrees and some statistics are required to improve confidence levels. In this case, orientation of the receivers was performed using a RA tag and a Rotoscan log. Additionally, the crosswell survey data are also useful for verifying the Rotoscan data and the functionality of the receivers.

To extract accurate distance and elevation data, a reasonable estimate of the velocity must be made. Velocities were obtained from both sonic logs and from the crosswell survey.

9.5.1.2 Receiver Orientation

It is assumed that the Rotoscan survey provides an accurate receiver orientation, but a check using crosswell data is always a good idea because it turns up problems that might not be otherwise noticed. To perform these checks, three primacord shots performed on April 7, 1997 were analyzed for orientation. These particular three were chosen because they were located at the bottom, top, and middle of the receiver vertical span. Files analyzed included "upr02_2_9515.segy" located at 9515 ft, "upr03_2_7856.segy", located at 7856 ft, and "upr04_2_8400.segy", located at 8400 ft. The orientations of these shots, relative to the Rotoscan, are shown in Figure 83. In general, the agreement is good, particularly in the center of the array. Several of the upper levels show considerable discrepancy, but this may be due to the distance to most of the shots. The most important feature of this plot is the large disagreement seen on four of the levels, which suggests that these levels may have been cross wired. These levels are at 7619 ft (level 7), 8069 ft (level 16), 8215 ft (level 19) and 8521 ft (level 25). The cross wiring is also suspected from examination of the microseismic data for changes in phase relationships from level to level. Tabular results from these tests are shown in Table 5. Missing data are indicative of broken channels or of shots that are too far from the receiver to be adequately analyzed. Standard deviations of 5° or less are usually indicative of a good orientation result. Many of these levels show greater standard deviations, but these could probably be improved by analyzing more of the primacord shots.

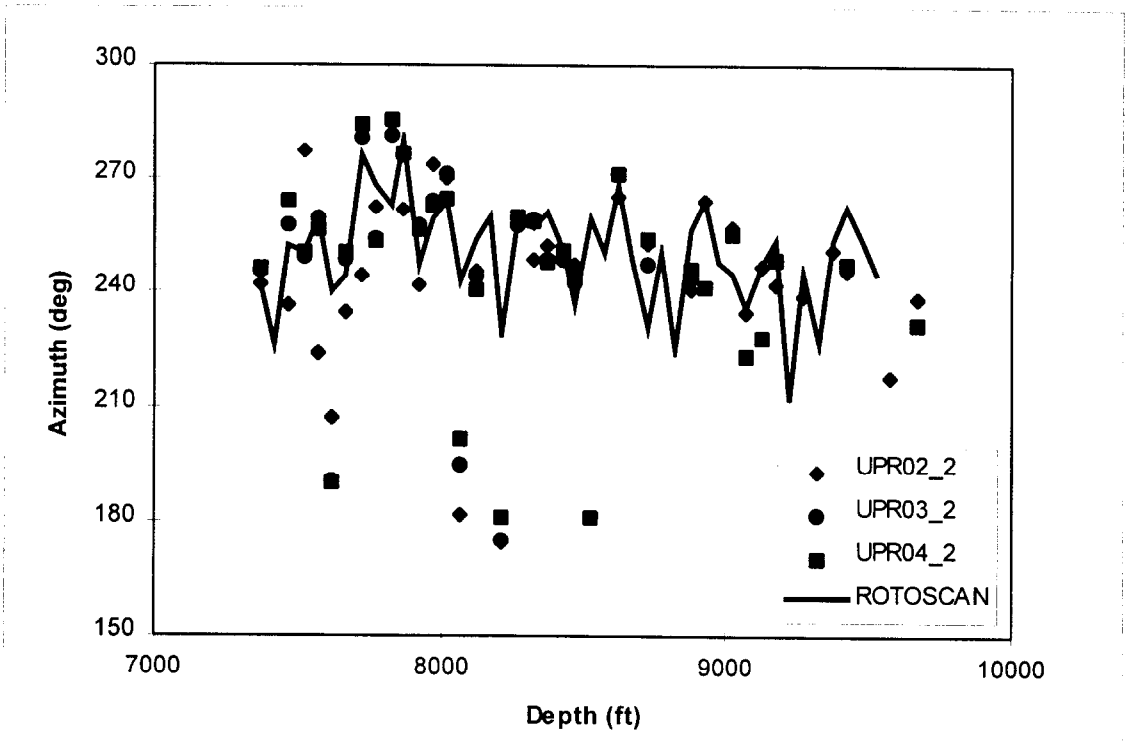

Figure 83. Comparison of primacord hodograms and Rotoscan orientations.

Table 5 Hodogram results for three primacord shots

Depth	upr02-2 azimuth	upr03-2 azimuth	upr04-2 azimuth	AVG	STD
7318					
7368	241.77	245.24	245.75	244.2533	2.165695
7418					
7468	236.62	257.38	263.74	252.58	14.18286
7519	277.23	249.18	249.97	258.7933	15.97151
7569	223.61	259.04	256.32	246.3233	19.71728
7619	206.81	190.91	190.38	196.0333	9.336629
7669	234.75	248.44	250.04	244.41	8.403969
7719	244.05	280.98	284.22	269.75	22.31573
7769	262.41	253.85	253.29	256.5167	5.111451
7823	281.86	281.36	285.9	283.04	2.489418
7870	261.69	275.99	276.89	271.5233	8.527798
7920	241.85	257.58	256.44	251.9567	8.771171
7970	273.77	264.07	262.66	266.8333	6.048556
8019	270.18	270.98	264.64	268.6	3.452709
8069	181.79	195.29	201.36	192.8133	10.01732
8119	245.56	244.36	240.3	243.4067	2.756544
8171					
8215	174.85	175.23	181.03	177.0367	3.463543
8271	257.46	257.7	259.8	258.32	1.287323
8321	248.52	259.17	258.43	255.3733	5.946683
8371	251.97	248.66	248.08	249.57	2.098595
8431	250.92	248.47	250.54	249.9767	1.318572
8471	247.21	242.39	243.4	244.3333	2.541935
8521			181.24	181.24	
8571					
8621	265.43	270.95	271.34	269.24	3.305314
8671					
8722	252.64	247.5	253.95	251.3633	3.409257
8773					
8823					
8873	240.78	243.7	245.9	243.46	2.568424
8923	264.01		241.01	252.51	16.26346
8973					
9023	256.91		255	255.955	1.350574
9073	234.82		223.27	229.045	8.167083
9123	246.74		227.86	237.3	13.35018
9173	241.73		248.5	245.115	4.787113
9223					
9274	238.79			238.79	
9324					
9374	250.86			250.86	
9425	245.17		247.18	246.175	1.421285
9475					
9525					
9575	217.73			217.73	
9625					
9675	238.42		231.49	234.955	4.90025

9.5.1.3 Velocity Structure

Accurate microseism location relies on accurate knowledge of the formation velocities. For this test, velocities were obtained from both a dipole sonic log and a crosswell survey produced by John Fairborn from the primacord and vibrator shots.[3] Table 6 lists estimated sonic-log velocities taken over limited intervals. Given that the microseismic analyses require average velocities, these data yield an average p-wave velocity of 14,500 ft/sec and an average s-wave velocity of 8,400 ft/sec.

Table 6 Estimated interval velocities from sonic log

Depths (ft)	Compressional Velocity (ft/sec)	Shear Velocity (ft/sec)
9265-9330	15,400	10,000
9330-9365	13,300	7,700
9365-9400	14,300	8,500
9400-9512	13,300	7,400
9512-9540	16,700	9,100
9540-9570	14,300	8,000
9570-9660	15,400	9,100
9660->	13,300	7,100

Generally, a crosswell survey yields better velocity estimates because it is conducted at frequencies more representative of the microseisms and it samples a larger section of the formation. Based upon the crosswell results, the average p-wave velocity is 15,100 ft/sec and the average s-wave velocity is 9,000 ft/sec. The velocities from the crosswell survey are approximately 600 ft/sec faster than that obtained from the log.

9.5.1.4 Receiver Characteristics

Upon examination of crosswell primacord shots and subsequent microseismic data, it was found that a number of the receiver levels had some problems that limited their usefulness. Table 7 shows a listing of the levels, their depths, the Rotoscan azimuths, the observed problems, and levels at which hodograms could be accurately made. Of particular interest for the Taylor sand operations is the bottom of the array, as these receivers are closest to the microseisms and the energy will travel through the fewest layers to reach the receivers. Unfortunately, the bottom of the array has very few levels which are responding adequately. There is only one level in the vicinity of the Taylor sand on which good hodograms can be obtained. The next closest level is 350 ft above, and the next hodogram level is an additional 200 ft above. In general, the best hodogram data are obtained from p-waves which are traveling within the horizontal layers. As a result, the hodogram information for this test will have a relatively large uncertainty.

Table 7 Receiver level characteristics

LEVEL	DEPTH	ROTOSCAN	PROBLEMS	HODOGRAMS
1	7318	148	NO X	
2	7368	242	NOZ	HODOGRAM
3	7418	226	NO X,Z	
4	7468	252		HODOGRAM
5	7519	250		HODOGRAM
6	7569	259		HODOGRAM
7	7619	240	POOR X,Y	
8	7669	244		HODOGRAM
9	7719	276		HODOGRAM
10	7769	268	BROKE	
11	7823	263		HODOGRAM
12	7870	280		HODOGRAM
13	7920	247	BROKE	
14	7970	259	BROKE	
15	8019	264	NO X	
16	8069	243	CROSS WIRED	
17	8119	254	NO Z	HODOGRAM
18	8171	260	NO X,Z	
19	8215	229	CROSS WIRED	
20	8271	259		HODOGRAM
21	8321	257		HODOGRAM
22	8371	261		HODOGRAM
23	8431	251		HODOGRAM
24	8471	237		HODOGRAM
25	8521	259	BROKE	
26	8571	250	BROKE	
27	8621	268	BROKE	
28	8671	249	BROKE	
29	8722	231	BROKE	
30	8773	250	NO Z	HODOGRAM
31	8823	225	BROKE	
32	8873	256	BROKE	
33	8923	264		HODOGRAM
34	8973	248	NO Z	HODOGRAM
35	9023	245	NO Y	
36	9073	236	NO X,Y	
37	9123	247	BROKE	
38	9173	253		HODOGRAM
39	9223	212	BROKE	
40	9274	245	BROKE	
41	9324	227	BROKE	
42	9374	253	BROKE	
43	9425	262	NO X,Z	
44	9475	253	BROKE	
45	9525	245	NO Z	HODOGRAM
46	9575		POOR X,Y	
47	9625		BROKE	
48	9675		NO X	

9.5.1.5 Microseism Characteristics

The general characteristics of the microseisms were that they had large, easily visible s waves on most levels (although they were often obscured on the lowest levels), but easily visible p waves only on the lower levels. Typically, p waves that were observable on the upper levels had considerable scatter in their hodogram azimuths and consequently were seldom used.

The spectral content of most of the microseisms were relatively broad band, as seen in both the p-wave example in Figure 84 and the s-wave example in Figure 85. This behavior suggests that there were no internal resonances with the receiver or transducer (as would be expected since they were grouted in place), but also suggests that there may be considerable energy at higher frequencies which could not be captured with the 1 msec sampling rate. As can be seen from the amplitude relationships, the receivers were generally oriented with the y axis pointing toward the microseisms. There are large amplitudes on the y axis of the p wave and the large amplitudes on the x axis of the s wave.

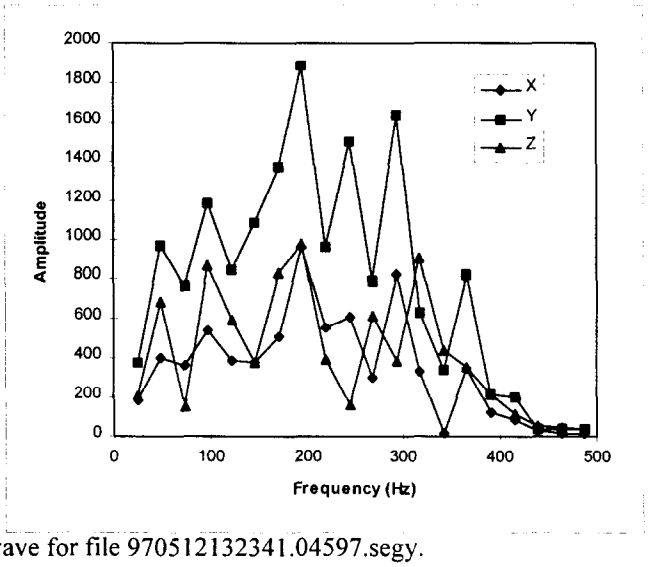

Figure 84. Spectrum of p wave for file 970512132341.04597.segy.

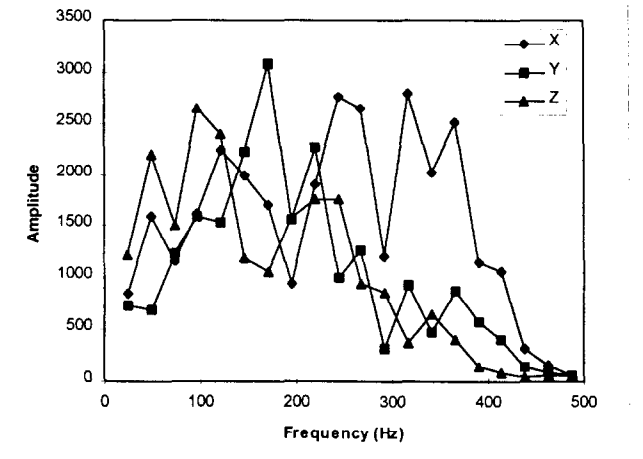

Figure 85. Spectrum of s wave for file 970512132341.04597.segy.

Table 8 shows an example data set taken from one of the microseisms. This suite of data, which starts at level 16 (few p-waves could be observed above 8000 ft), is relatively sparse, particularly at the 9600 ft interval (the frac interval). Only eight usable hodograms have been extracted, with considerable scatter in the absolute azimuth. The hodogram azimuth on level 46 is referenced to the crosswell orientations, as there was no Rotoscan data for the

bottom three levels. Thus, the discrepancy in absolute angle between it and higher levels may be due to orientation errors. Note also that there are fewer hodograms in Table 8 than possible (e.g., Table 7) because some levels may not provide sufficiently clear p waves to produce good quality hodograms.

Table 8. Example microseism data set

Depth	Orientation	Level	Azimuth	Inclination	P-Arrival	S-Arrival	Abs Azimuth
8069	243	16			450	526	
8119	254	17				521	
8171	260	18				519	
8215	229	19				513	
8271	259	20	-28.58	24.64	433	510	50.42
8321	257	21					
8371	261	22	-19.8	25.68	424	501	61.2
8431	251	23	-22.16	47.08	429	495	48.84
8471	237	24	-9.37	18.79	427	494	47.63
8521	259	25					
8571	250	26					
8621	268	27					
8671	249	28					
8722	231	29					
8773	250	30					
8823	225	31					
8873	256	32					
8923	264	33	-45.88	25.36	403	462	38.12
8973	248	34	-17.55	11.19	401	461	50.45
9023	245	35			401	461	
9073	236	36			399	461	
9123	247	37					
9173	253	38	-24.5	27.14	396	454	48.5
9223	212	39					
9274	245	40					
9324	227	41					
9374	253	42					
9425	262	43					
9475	253	44					
9525	245	45					
9575	218	46	-3.53	0.03	388	447	34.47
9625	226	47					
9675	235	48			390	452	

9.5.1.6 Results

Sixty eight microseisms were found to be locatable using the single-well approach. Minimum requirements for analysis were two hodogram azimuths and at least one p-wave arrival (if there were also several s-wave arrivals) or at least one s-wave arrival (if there were also several p-wave arrivals). Using the velocities derived from the averaging of the crosswell survey, Figures 86 and 87 show plan view and side view maps of the analyzed microseisms. These data are very similar to the ARCO results, yielding a long, well-contained fracture whose azimuth is N80°E. However, there are some differences in the scatter and the lack of intersection of the microseisms with the fracture well. Even more significant differences arise when one considers the effect of the velocity uncertainty.

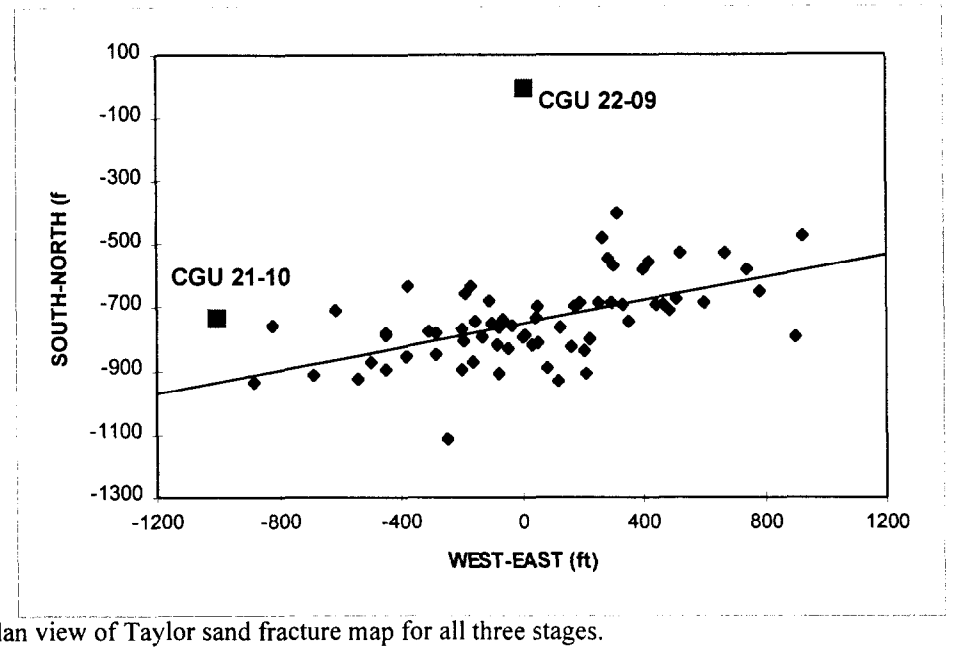

Figure 86. Plan view of Taylor sand fracture map for all three stages.

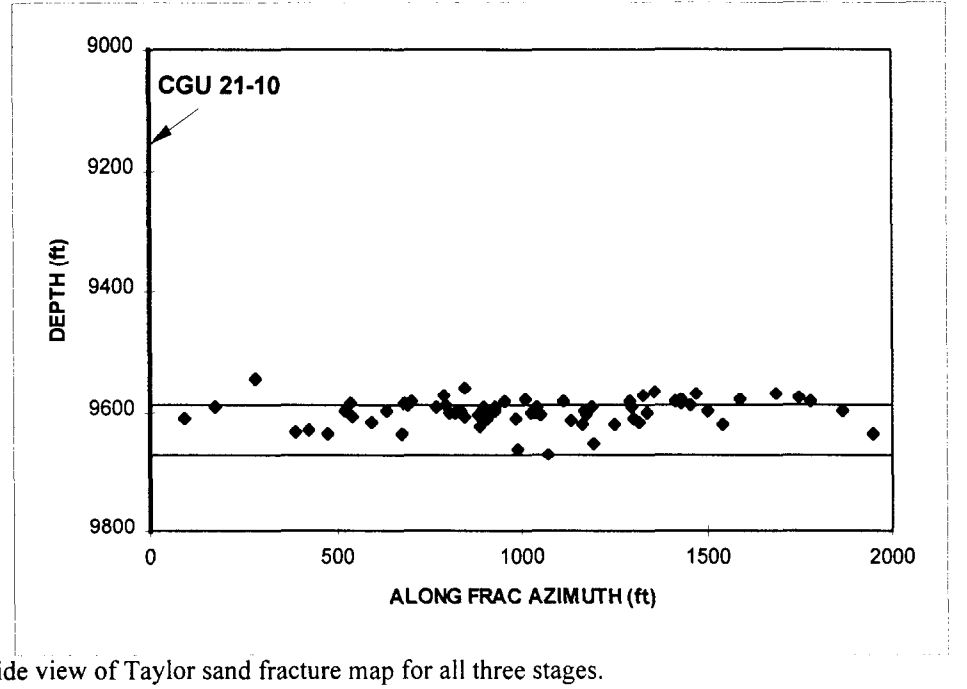

Figure 87. Side view of Taylor sand fracture map for all three stages.

Because of the array configuration (no receivers below the frac interval and few usable receivers across from the frac interval), small changes in velocity result in significant changes in the map. For example, Figures 88 and 89 show the maps that would result if the log-derived velocities were used. In this case, the plan view map appears to more closely intercept the fracture well, but all of the microseisms are now located about 100 ft above the Taylor sand.

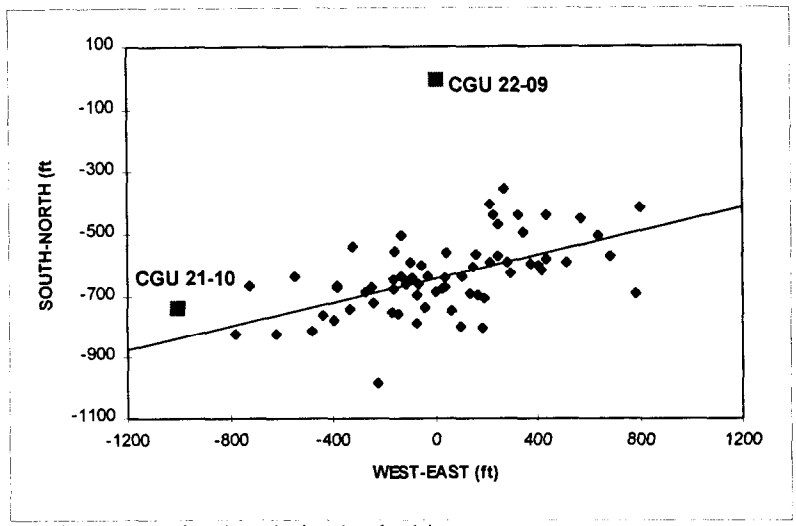

Figure 88. Revised plan view map using log-derived velocities.

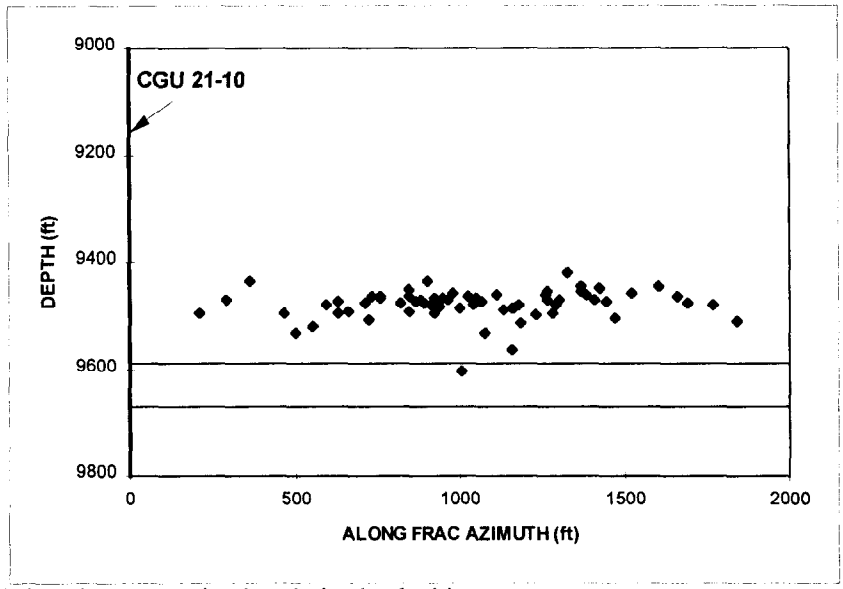

Figure 89. Revised side view map using log-derived velocities.

If velocities more typical of ARCO's (p=16,500 ft/sec; s=10,000 ft/sec; without anisotropy) are used, then the points locate approximately 100 ft below the Taylor sand. As ARCO has shown, anisotropic velocities can remedy the problem and bring the points back into the sand and have the plan view image intersect the fracture well.

At this time, it is believed that the data in Figures 86 and 87 represent the best image of this data set that can be obtained from the single-well approach. A listing of the data points are shown in Tables 9 and 10 for stages 1-2 and 3, respectively. The east and north locations are relative to the monitor well, the "result" is the projection of the location on the azimuth regression line, and the depth is relative to the monitor well. The last three columns are more interesting, as they provide uncertainty data taken from the joint p-s regression and the hodogram statistics. Generally, the height uncertainty is small because of the large number of receivers in the vertical plane, but this uncertainty assumes that the velocity structure is correct. Velocity uncertainties have a further effect on the uncertainty. The distance uncertainty is also relatively small because of the large number of receivers, with the same caveats relative to the velocity structure. The largest error is associated with the azimuth, primarily because

there are so few receivers laterally adjacent to the fracture interval. Angular uncertainties of 10° at 1000 ft result in lateral uncertainties of 173 ft and angular uncertainties of 20° at 1000 ft work out to 340 ft. These uncertainties are not large enough to affect the overall results, but they do demonstrate how important it is (1) to have high quality receivers and data acquisition and (2) to have the array strategically placed.

Table 9. Listing of Taylor sand microseismic locations and uncertainty data - Stage 1 & 2

east	north	result	depth	Height sd	Dist sd	Angle sd
-448.88	-892.28	521.31	9598.32	8.41	47.57	12.53
-500.17	-871.00	474.66	9634.88	6.67	29.43	7.31
-687.39	-911.90	283.15	9546.19	16.07	37.21	11.65
-542.74	-924.66	423.17	9629.40	14.45	30.77	7.75
-824.24	-757.14	176.27	9592.98	12.10	53.76	8.15
-879.72	-932.62	90.22	9611.43	9.65	41.21	9.14
-161.94	-871.51	807.32	9600.65	10.90	59.03	15.74
-285.15	-779.65	702.58	9582.89	6.90	41.84	10.20
-79.31	-905.17	882.57	9604.61	9.63	54.46	13.28
-383.09	-854.46	592.81	9617.78	7.92	46.63	12.12
-195.53	-768.90	792.68	9588.63	5.23	36.20	11.72
-191.03	-806.17	790.42	9573.67	7.29	38.25	13.82
-134.05	-796.77	848.16	9606.37	6.12	38.74	10.00
-80.03	-817.51	897.58	9593.21	10.58	67.96	11.48
-152.75	-749.03	838.33	9597.53	10.77	72.46	20.59
-106.85	-682.66	895.39	9594.37	7.20	50.08	15.74
-77.53	-764.56	909.55	9609.57	5.37	38.51	12.62
5.13	-794.57	985.48	9610.45	5.12	33.07	8.04
-9.84	-737.57	979.57	9598.29	4.42	25.86	15.44
-32.85	-757.05	954.84	9583.25	11.25	63.38	12.08
-281.46	-848.05	693.94	9590.10	8.00	44.47	10.19
-165.34	-633.74	846.61	9559.89	8.17	59.38	21.60
-44.69	-830.43	930.04	9593.20	6.75	38.37	6.25
174.51	-702.37	1168.65	9598.71	5.20	28.96	5.79
127.32	-766.51	1110.73	9581.58	6.44	42.31	12.41
-100.51	-751.30	889.31	9625.02	4.60	32.52	4.77
116.08	-931.33	1070.11	9670.12	16.26	108.27	7.11
254.37	-687.66	1249.85	9621.63	5.86	32.50	8.67
45.13	-738.19	1034.94	9602.54	5.58	34.35	16.35
162.28	-823.57	1134.88	9613.16	6.94	32.18	13.58
-63.32	-738.98	928.11	9599.52	3.54	23.98	9.78

Table 10. Listing of Taylor sand microseismic locations and uncertainty data - Stage 3

east	north	result	depth	Height sd	Dist sd	Angle sd
-196.80	-893.10	769.15	9590.70	6.28	22.83	18.29
53.99	-699.66	1050.57	9605.35	3.33	23.88	9.41
208.89	-905.02	1166.12	9621.69	23.97	52.52	4.94
-186.07	-660.40	821.44	9602.44	15.35	102.69	11.46
49.43	-813.27	1025.71	9601.63	4.49	26.44	14.57
193.93	-688.15	1190.31	9592.74	5.92	26.86	17.25
-446.39	-783.40	543.28	9606.73	5.94	26.24	9.18
282.75	-549.00	1302.64	9609.93	7.30	45.88	9.29
-447.52	-790.76	540.85	9585.71	6.66	35.85	8.56
402.55	-581.70	1414.63	9582.51	5.50	36.79	12.23
6.56	-788.03	988.06	9660.69	9.93	19.14	5.60
353.44	-745.93	1336.87	9602.44	4.30	23.53	13.51
79.91	-887.68	1042.35	9591.26	6.73	34.20	12.11
220.09	-801.64	1195.69	9652.79	6.29	24.08	15.22
312.46	-406.40	1357.45	9567.15	10.68	81.88	10.43
-615.38	-711.69	389.89	9633.06	8.28	35.21	18.88
466.56	-695.26	1457.24	9588.52	4.31	26.17	11.36
33.15	-816.91	1009.04	9580.89	4.07	23.74	4.14
598.64	-685.89	1588.86	9580.15	3.60	18.31	12.35
-308.13	-777.19	680.42	9585.60	3.37	23.43	8.21
334.27	-696.83	1326.81	9573.64	5.82	26.54	14.97
-249.79	-1113.73	677.46	9636.72	10.18	35.24	7.01
415.38	-557.60	1431.58	9580.29	3.37	21.62	7.51
440.69	-696.56	1431.56	9585.45	3.65	20.48	9.92
669.27	-526.91	1686.86	9568.76	5.85	33.34	4.93
785.55	-653.84	1778.48	9583.84	6.47	20.89	9.24
203.74	-836.86	1173.29	9603.59	12.70	58.33	10.89
304.02	-571.10	1319.61	9618.43	7.00	43.82	20.81
509.88	-677.15	1503.10	9599.41	6.35	31.27	12.72
487.22	-713.95	1474.21	9569.28	8.74	47.34	6.48
740.44	-582.22	1746.95	9576.96	7.94	31.12	18.78
262.88	-481.69	1295.17	9592.41	3.84	32.02	7.57
524.87	-528.74	1544.47	9619.74	5.32	27.18	13.58
927.99	-476.96	1950.34	9636.78	5.37	24.43	7.41
901.48	-794.95	1867.23	9599.03	7.73	32.59	13.33
298.27	-685.81	1293.37	9584.16	3.66	22.23	1.88

9.5.1.7 Discussion

We find that there is no unique solution to calculating the microseismic locations for this array geometry (single well, all receivers above the interval, sparse data set) because of the uncertainty in the velocity structure and the sparse array at the fracture depth. The two later fracture experiments, with receivers in two wells and both above and below the fracture interval, provide much more constraint and limit most uncertainty due to velocity structure.

A major issue associated with these maps is the lack of any microseisms on the far wing of the fracture. Given that this single-well analysis requires a number of clear p waves for accurate location, it is not believed that any microseisms of the magnitudes seen here could have been observed at distances greater than the wellbore location (about 1200-1300 ft horizontally). Other analyses - such as ARCO's - which do not need polarization information can extract locations from greater distances, and may be able to observe microseisms of the strengths found here at distances representative of the far wing. Such is not true for these single-well approaches. The subsequent Imaging Project fracture experiments, however, have much larger amplitude microseisms and it may be possible to detect them from as far away as the opposite wing using this approach.

Since (1) the microseismic data have relatively low-level amplitudes, (2) the receivers are poorly distributed relative to the fracture's vertical location, and (3) there is considerable uncertainty in the velocity structure, advanced analyses of the microseismic locations using a layered medium do not appear warranted. Such an analysis would account for the layering and its effect on the ray paths.

Although it was originally intended to to extract 5-level data from this data set for comparison calculations, the quality of the data and the limited receivers at the depth of the fracture make this a futile exercise. However, the uppermost fracture interval is suitably placed relative to the working receivers to make that test a good comparison case. This analysis will be done at a later time.

9.5.1.8 Conclusions

- This re-analysis of the Taylor sand microseismic data shows general agreement with the ARCO analysis using a different analysis approach.
- The fracture appears to be about 2000 ft long on the east wing with a well-contained height and an azimuth of N80°E. However, some uncertainties remain because of the limited velocity structure information and the skewed receiver array. This length is considerably longer than the ARCO analysis (1400 ft).
- Using this approach, it appears that no microseisms could be observed on the far wing of the fracture unless they were much stronger than those generally observed in this test.
- No further analyses of the Taylor sand data appears reasonable at this time.
- Additional analyses of the upper fracture will be performed at a later time.

9.5.2 Extraction of 5-Level Data

It was originally intended that 5-level data be extracted from each of the three injections at Carthage. However, because many of the receivers had failed (particularly the deep ones), the only injection from which quality 5-level data could be extracted was the last injection. The deeper injections had no good tri-axial receivers below the fracture interval to constrain the height of the fracture. As a result, extraction analyses will only be performed on the final injection.

To process the information, it was necessary to write two codes to convert the data. Since GRI data is fully taken and processed on PC platforms, the SEG2 disk data format is used for all GRI software. ARCO, however, wrote the data in SEGD format (a tape format), and this needed to be converted to SEG2 for further processing. Once in SEG2 format, a second code was written to extract appropriate 5-level data from the complete microseismic data set. This was considerably more complicated than it should have been because ARCO's format did not have channels in sequence, but rather scattered throughout the data set. These two codes were completed in 1997 and some initial data from the first minifrac of the third injection was extracted and analyzed using SMART5. The full data set will be extracted and processed in 1998.

10.0 TILTMETER STUDIES

Tiltmeter studies have included three primary topics dealing with modeling and instrumentation. First, finite element analyses of the M-Site tiltmeter data were completed. Second, analytic models have been developed for analyzing downhole tiltmeter data and these results are being continually refined with the addition of new features (e.g., dip, parallel axis analyses). Third, some limited work on tiltmeter instrumentation which could be employed in tandem with the microseismic receivers is being conducted. During 1997, a topical report on the finite-element analyses of the B-sand experiments was completed. This report is titled "Hydraulic Fracture Imaging Using Inclinometers at M-Site: Finite Element Analyses of the B-Sandstone Experiments," and was authored by Engler and Warpinski.

10.1 M-Site Finite Element Analyses of C-Sand Inclinometer Data

Only a limited number of finite element calculations were performed for the C sandstone data because the inclinometers were degrading and two of them were apparently not functioning properly. One of these was the inclinometer in the C sandstone, which is an important data point for correctly centering the fracture. Nevertheless, some of the fracture injections provided sufficiently high quality data that finite-element calculations could be appropriately applied. In all cases, only 2-D finite-element calculations were performed; full 3-D calculations did not appear warranted given the degraded data.

10.1.1 Injection 1C

Figure 90 shows a comparison of the actual 1C inclinometer data with two finite-element calculations performed at net pressures of 1000 psi and heights of 87 and 107 ft (with only height growth upward in the 107-ft height case). The 87-ft fracture corresponds to a fracture confined to the C sandstone with only slight growth into the shales to provide containment. In this case, the data do not match, as the measured inclinations are much lower than the calculated values for the measured net pressure of the injection. The reason for the mismatch, however, is most likely due to the short length of this breakdown injection. For the 2-D models to give accurate results, the length must be in excess of 400 ft and preferably as much as 600 ft. This result is based on analytic calculations using a flat 3-D elliptic crack model for the position of the monitor well relative to the fracture at M-Site. If the instrumented well is in a different position, the appropriate length will be different.

For the 1C injection, the microseismic height was approximately 120 ft, but the wing length was only 200 ft. Based on the elliptic results, this length is too short to be adequately modeled with using the 2-D approximation, thus resulting in an overestimate of the amplitudes.

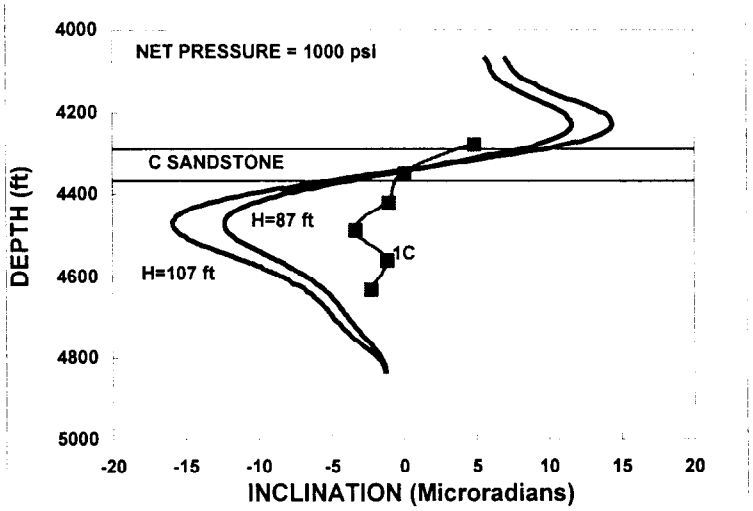

Figure 90 Finite-element model of the 1C injection compared to measured data.

10.1.2 Injection 2C

Injection 2C finite element calculations are discussed with the 3C data, as both injections had similar net pressures.

10.1.3 Injection 3C

A comparison of the 2C and 3C injection data with an 87-ft tall fracture for a net pressure of 800 psi is shown in Figure 91. In this case, the lengths of the two fractures are greater than 400 ft and heights are approximately 80 ft for injection 2C and about 100 ft for injection 3C on the east wing where the inclinations are being measured. The comparison is interesting, as the model shows good agreement with the upper levels, but underestimates the response for the lower levels. These data could be fit closer with a smaller height, assuming the fracture only propagated through the upper section of the C sandstone.

In fact, the microseismic results suggest that most of the 2C and 3C injections were confined to the top of the C sandstone. Furthermore, the data also suggest that the C sandstone may have an upper channel starting about 150-200 ft on the east wing, further causing the fracture results to be shifted upward. To appropriately model such complexity would require using a 3-D finite-element model, breaking the C sandstone into several intervals, and confining the fracture to only a part of the C sandstone. This level of effort was not deemed warranted based on the uncertain quality of some of the inclinometer data. A sufficient result from the inclinometer data is the recognition that there was little height growth upward and probably minimal penetration of the bottom part of the C sandstone.

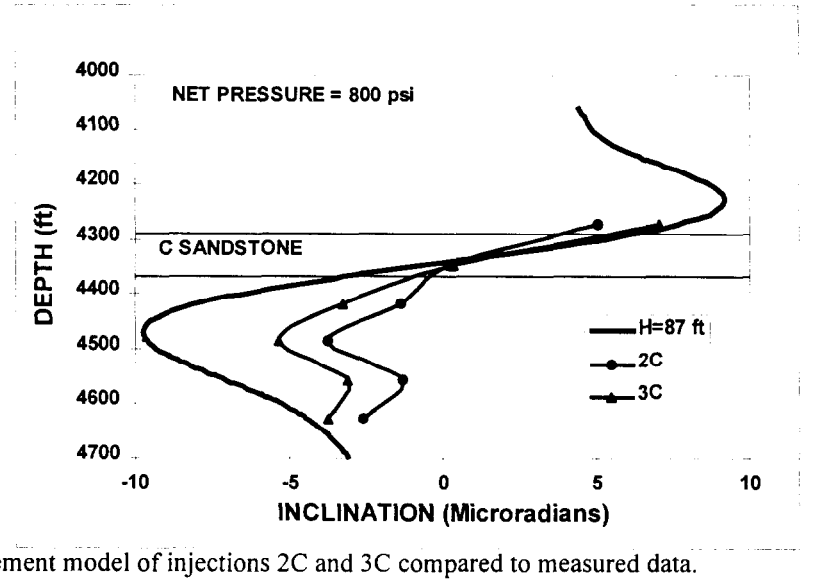

Figure 91 Finite-element model of injections 2C and 3C compared to measured data.

10.1.4 Injection 4C

Figure 92 shows the comparison of the injection 4C inclinometer data with three finite-element calculations, all having net pressures of 1200 psi. Cases are shown for heights of 87, 107 and 137 ft, with only height growth upward. Also note that the inclinometer which was second from the bottom is no longer shown in the data set since it stopped responding entirely. In this comparison, the upper inclinations overshoot all model runs, while the lower inclinations fit somewhere in between the various calculations. Based on the microseisms, the east wing length is on the order of 650 ft, so the 2-D model should be an excellent approximation. Based upon the undershoot on one side and overshoot on the other, it appears that the 137-ft height is a reasonable representation, although it is clear that modulus or other effects have significantly perturbed the actual inclinations. The 137-ft case was modeled because it is the height observed from microseisms in the 4C injection, and these data support that result.

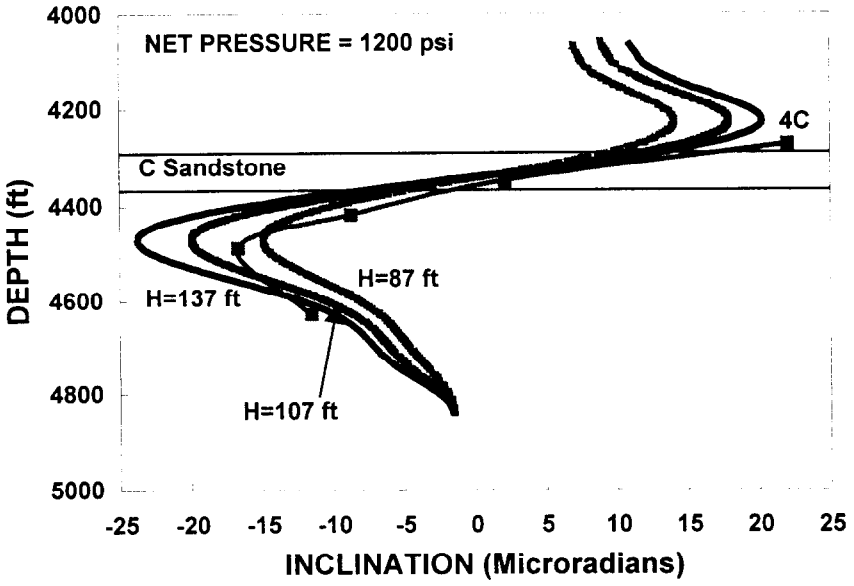

Figure 92 Finite-element model of injection 4C compared to measured data.

10.1.5 Injection 5C

Figure 93 shows the comparison of the injection 5C inclinometer data with three finite-element calculations, all having net pressures of 1400 psi. Cases are shown for heights of 87, 107 and 137 ft, with only height growth upward. As with the 4C injection data, the inclinometer which was second from the bottom is no longer shown in the data set since it stopped responding entirely. Based on the microseisms, the east wing length is on the order of 500 ft, so the 2-D model should be an excellent approximation. These data basically fit the case of an 87-ft fracture, although the lower peak match suggests that the fracture height may even be somewhat less than 87 ft. This result is in agreement with the microseismic data which shows a reasonably contained fracture for this injection.

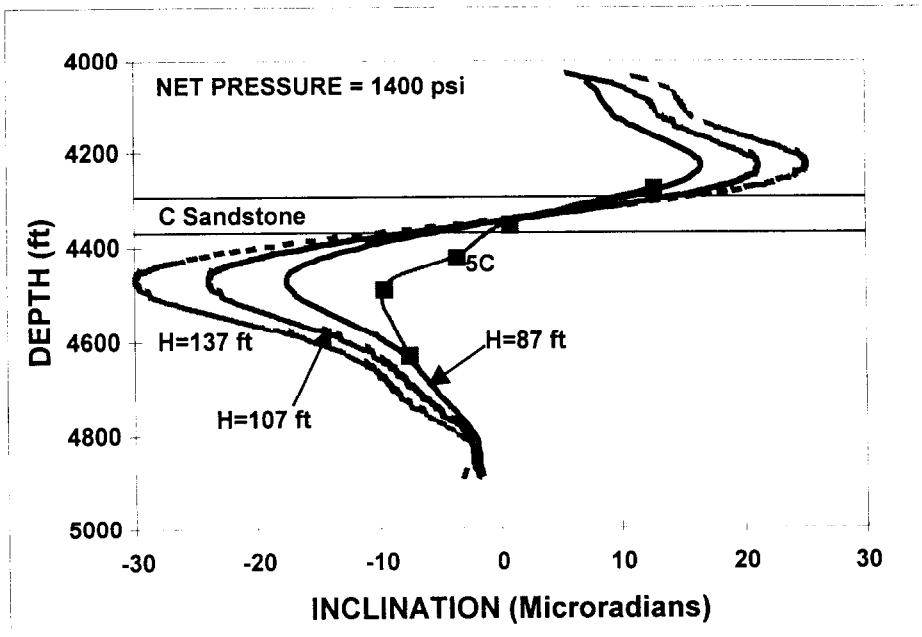

Figure 93 Finite-element model of injection 5C compared to measured data.

10.1.6 Injection 6C

Figure 94 shows the comparison of the injection 6C inclinometer data with two finite-element calculations, each having net pressures of 2000 psi. Cases are shown for heights of 87 and 127 ft, with symmetric height growth in the 127 ft height case. As with the 4C and 5C injection data, the inclinometer which was second from the bottom is no longer shown in the data set since it stopped responding entirely. Based on the microseisms, the east wing length is on the order of 450 ft, so the 2-D model should be an acceptable approximation. These data basically fit the case of a fracture with a height less than 127 ft, primarily because the high net treatment pressure induces very large tilts even for a short-height fracture. If the treatment pressure is less in the fracture extremities, then additional height would be needed to induce the measured tilts. As before, the somewhat degraded condition of the tiltmeters makes it unwarranted to perform any additional detailed analyses. It suffices to note that the tiltmeter data suggest that there is no extensive height growth, in agreement with the microseismic data.

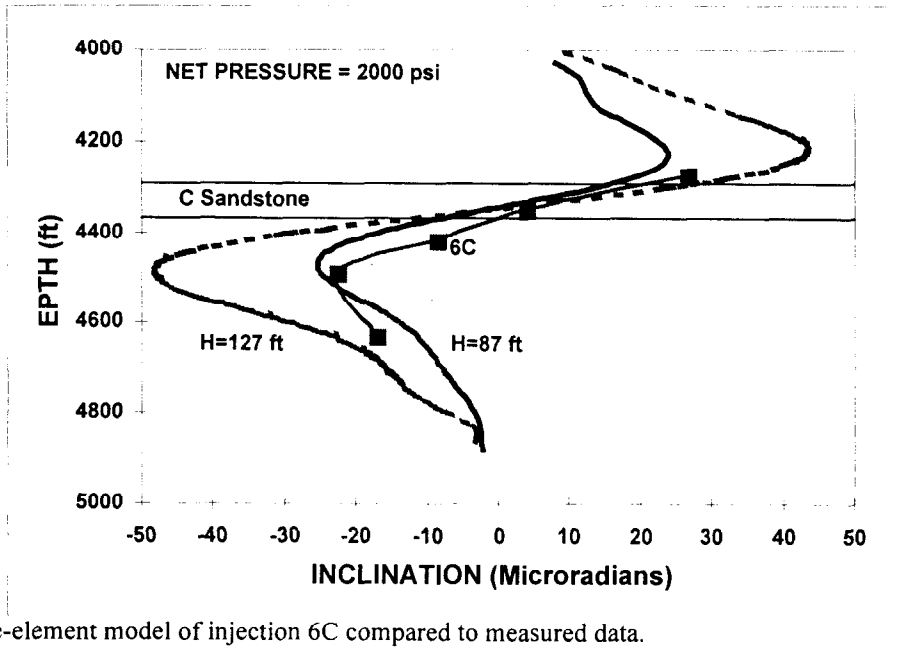

Figure 94 Finite-element model of injection 6C compared to measured data.

10.2 Analytic Models

Although too detailed to be given here, the downhole tiltmeter analysis for a flat 3-D elliptic crack (Green and Sneddon) has been extended to account for fractures that are taller than they are wide and have a dip associated with them. These additions required the calculation of all strain gradients and appropriate geometric combinations of those gradients to extract the correct tilt field.

10.2 Tiltmeter Instrumentation

Some initial work has been performed on non-bubble type tiltmeters that could be easily applied to fracture diagnostics by incorporating them in the current microseismic receiver system. One particular technology has been found to be promising and this technology will be examined further as time permits.

11.0 TECHNOLOGY TRANSFER

11.1 Papers and Reports Prepared During 1997

Several papers and reports were prepared during 1997. These include:

- Warpinski, N.R., Uhl, J.E., and Engler, B.P., "Review of Hydraulic Fracture Mapping Using Advanced Accelerometer-Based Receiver Systems," Proceedings, US DOE Natural Gas Conference, Houston, TX, March 24-27, 1997.
- Warpinski, N.R. Uhl, J.E., Engler, B.P., Lorenz, J.C. and Young, C.J., "Development of Stimulation Diagnostics," GRI Annual Report GRI-97/1327, June 1997.
- Warpinski, N.R., Branagan, P.T., Engler, B.P., Wilmer, R., and Wolhart, S.L.: "Evaluation of a Downhole Tiltmeter Array for Monitoring Hydraulic Fractures", Proc. 36th U.S. Rock Mechanics Symposium, Columbia University, NY, June 29 - July 2, 1997.
- Warpinski, N.R., Branagan, P.T., Peterson, R.E., Fix, J.E., Uhl, J.E., Engler, B.P. and Wilmer, R., "Microseismic and Deformation Imaging of Hydraulic Fracture Growth and Geometry in the C Sand Interval, GRI/DOE M-Site Project," SPE 38573, 1997 SPE Annual Technical Conference and Exhibition, San Antonio, TX, October 5-8.
- Branagan, P.T., Warpinski, N.R., Peterson, R.E., Hill, R.E., and Wolhart, S.L.: "Propagation of a Hydraulic Fracture into a Remote Observation Wellbore: Results of C-Sand Experimentation at the GRI/DOE M-Site Project", SPE 38574, 1997 SPE ATCE, San Antonio, TX, Oct. 5-8.
- Warpinski, N.R., Branagan, P.T., Peterson, R.E. and Wolhart, S.L., "An Interpretation of M-Site Hydraulic Fracture Diagnostic Results," SPE 39950, 1998 Rocky Mountain Regional/Low Permeability Reservoirs Symposium and Exhibition, Denver, CO, April 5-8.
- Warpinski, N.R., Branagan, P.T., Peterson, R.E., Wolhart, S.L. and Uhl, J.E., "Mapping Hydraulic Fracture Growth and Geometry Using Microseismic Events Detected by a Wireline Retrievable Accelerometer Array," SPE40014, 1998 Gas Technology Symposium, Calgary, Alberta, Canada, March 15-18.
- Engler, B.P. and Warpinski, N.R., "Hydraulic Fracture Imaging Using Inclinometers at M-Site: Finite-Element Analyses of the B-Sandstone Experiments," GRI Topical Report, GRI-97/0361, December 1997.

11.2 Workshops and Seminars

Technology transfer is an essential element of this work. Although technology transfer is often effectively carried out through reports and papers, workshops and seminars are an equally important method. Technical workshops and seminars conducted in 1997 include full or partial participation in:

February 1997 - M-Site Fracturing Results (Marathon Oil Company Presentation, Tyler, TX)
A presentation of the M-Site microseismic, inclinometer, and core-through fracture results for local Marathon engineers as part of a GRI Technology Transfer Workshop.

February 1997 - M-Site Technology Transfer Workshop (GRI Workshop, Dallas)
A full day workshop on M-Site results and implications, including all aspects of microseismics, inclinometers, core-throughs, fracture modeling, and other results.

April 1997 - M-Site Fracture Diagnostics Workshop (GRI Workshop, Tulsa)
A full day workshop on M-Site results and implications, including all aspects of microseismics, inclinometers, core-throughs, fracture modeling, and other results.

April 1997 - M-Site Microseismic Diagnostic Results (Chevron USA Workshop, Houston)
A full day internal Chevron workshop on fracture diagnostics, with the Sandia presentation focusing on the microseismic results from M-Site.

May 1997 - M-Site Microseismic Diagnostic Results (Crosstimber Oil Co. Workshop, Fort Worth)

A full day internal Crosstimber workshop on fracture diagnostics, with the Sandia presentation focusing on the microseismic results from M-Site.

May 1997 - M-Site Fracture Diagnostics Workshop (SPE Workshop, Casper)
A full day workshop on M-Site results and implications, including all aspects of microseismics, inclinometers, core-throughs, fracture modeling, and other results.

June 1997 - M-Site Microseismic Diagnostic Results (Chevron USA Workshop, Midland)
A presentation to the local Chevron engineers on the M-site diagnostic results and how they might be used in Chevron's applications.

June 1997 - M-Site Fracture Diagnostic Results (Enron Oil Co. Workshop, Corpus Christi)
A presentation of M-site diagnostic results at a full day internal Enron workshop on hydraulic fracturing.

July 1997 - Microseismic Diagnostics (Western Atlas, Houston)
A presentation of the microseismic diagnostic technology to Western Atlas for the purpose of inviting them to apply to be a commercial diagnostic partner.

July 1997 - Microseismic Diagnostics (Schlumberger, Houston)
A presentation of the microseismic diagnostic technology to Schlumberger for the purpose of inviting them to apply to be a commercial diagnostic partner.

July 1997 - Microseismic Diagnostics (Pinnacle Technologies, Inc., Houston)
A presentation of the microseismic diagnostic technology to Pinnacle for the purpose of inviting them to apply to be a commercial diagnostic partner.

August 1997 - Microseismic Diagnostics (Protechnics, Houston)
A presentation of the microseismic diagnostic technology to Protechnics for the purpose of inviting them to apply to be a commercial diagnostic partner.

August 1997 - Microseismic Diagnostics (Halliburton, Houston)
A presentation of the microseismic diagnostic technology to Halliburton for the purpose of inviting them to apply to be a commercial diagnostic partner.

September 1997 - Fracture Growth and Complexity (Hydraulic Fracture Mech. Workshop, Houston)
A presentation of fracture diagnostic results showing fracture complexity at a GRI/Shell sponsored workshop of fracturing.

September 1997 - Microseismic Imaging of Hydraulic Fractures (GRI Forum, Houston)
A presentation of microseismic diagnostics at a GRI lunch-time brown-bag forum.

October 1997 - M-Site and Microseismic Imaging (GRI Project Advisors Group, Austin)
A presentation to the GRI PAG on M-Site final results and the status of microseismic imaging.

November 1997 - Microseismic Fracture Imaging (Greater Green River Basin Symposium, Denver)
A presentation of microseismic imaging and M-Site results at a workshop on advanced technologies.

12.0 REFERENCES

1. Warpinski, N.R., Teufel, L.W., Lorenz, J.C. and Holcomb, D.J., "Core Based Stress Measurements: A Guide to Their Application," GRI-93/0270, June 1993.
2. Hill, R.E, Peterson, R.E., Warpinski, N.R., Lorenz, J. and Teufel, L.W., "Techniques for Determining Subsurface Stress Direction and Assessing Hydraulic Fracture Azimuth," GRI-93/0429, November 1993.
3. Warpinski, Z.A. Moschovidis, C.D. Parker and I.S. Abou-Sayed, "Comparison Study of Hydraulic Fracturing Models: Test Case - GRI Staged Field Experiment No. 3," SPE Production and Facilities, Vol. 9 pp.7-12, February 1994.
4. Warpinski, N.R., Abou-Sayed, I.S., Moschovidis, Z. and Parker, C., "Hydraulic Fracture Model Comparison Study: Complete Results," GRI-93/0109, Gas Research Institute Report, February 1993.
5. Lorenz, J.C. and Laubach, S.E., "Description and Interpretation of Natural Fracture Patterns in Sandstones of the Frontier Formation along the Hogsback, Southwestern Wyoming," GRI-94/0020, January 1994.
6. Lorenz, J.C., Arguello, J.G., Stone, C.M., Harstad, H., Tuefel, L.W., and Brown, S.R., "Predictions of Fracture and Stress Orientations: Subsurface Frontier Formation, Green River Basin," GRI-95/0151, April 1995.
7. Sleefe, G.E., Warpinski, N.R. and Engler, B.P., "The Use of Broadband Microseisms for Hydraulic Fracture Mapping," *SPE Form Eval.*, Dec. 1995, 233-239.
8. Middlebrook, M., Peterson, R., Warpinski, N.R., Engler, B., Sleefe, G., Cleary, M, Wright, T. and Branagan, P., "Multi-Site Project Seismic Verification Experiment and Assessment of Site Suitability," GRI Topical Report, GRI-93/0050, Feb. 1993.
9. Warpinski, N.R., "Interpretation of Hydraulic Fracture Mapping Experiments," SPE 27985, Proceedings, Tulsa Centennial Petroleum Engineering Symposium, Tulsa, OK, pp. 291-300, August 1994.
10. Warpinski, N.R., Engler, B.P., Young, C.J., Peterson, R.E., Branagan, P.T. and Fix, J.E., "Microseismic Mapping of Hydraulic Fractures Using Multi-Level Wireline Receivers," SPE 30507, Proceedings, SPE Annual Technical Conference, Dallas, TX, October 22-25, 1995.
11. Peterson, R.E., Warpinski, N.R., Wright, T.B., Branagan, P.T. and Fix, J.E., "Results of M-Site Experimentation in the A-Sand Interval: Fracture Diagnostics, Fracture Modeling and Crosswell Tomography," GRI-95/0046, February 1995.
12. Branagan, P.T., Peterson, R., Warpinski, N.R. and Wright, T.B., "The Characterization of Remotely Intersected Set of Hydraulic Fractures: Results of Intersection Well No. 1: GRI/DOE Multi-Site Project," SPE 36452, SPE Annual Tech. Conf. & Exhibition, Denver, CO, Oct. 6-9, 1996.
13. Branagan, P.T., Warpinski, N.R., Engler, B.P., Wilmer, R., "Measuring the Hydraulic Fracture-Induced Deformation of Reservoir and Adjacent Rocks Employing a Deeply Buried Inclinometer Array: GRI/DOE Multi-Site Project," SPE 36451, SPE Annual Tech. Conf. & Exhibition, Denver, CO, Oct. 6-9, 1996.
14. Peterson, R.E., Wolhart, S.L., Frohne, K.-H., Warpinski, N.R., Branagan, P.T. and Wright, T.B., "Fracture Diagnostics Research at the GRI/DOE Multi-Site Project: Overview of the Concept and Results," SPE 36449, proceedings, 1996 SPE Annual Tech. Conf. and Exhibition, Denver, CO, October 6-9, 1996.
15. Warpinski, N.R., Wright, T.B., Uhl, J.E., Engler, B.P., Drozda, P.M. and Peterson, R.E., "Microseismic Monitoring of the B-Sand Hydraulic Fracture Experiment at the DOE/GRI Multi-Site Project," SPE 36450, proceedings, 1996 SPE Annual Tech. Conf. and Exhibition, Denver, CO, October 6-9, 1996.
16. Nelson, G.D. and Vidale, J.E., "Earthquake Locations by 3D Finite Difference Travel Times," *Bull. of the Seismological Society of America*, **80**, April 1990, 395.
17. Vidale, J.E., "Finite Difference Calculation of Travel Times," *Bull. of the. Seismological Society of America*, **78**, 1988, 2062.
18. Green, A.E. and Sneddon, I.N., "The Distribution of Stress in the Neighbourhood of a Flat Elliptic Crack in an Elastic Solid," *Proc. Camb. Phil. Soc.*, **46**, 159-163, 1950.
19. Nolte, K.G. and Smith, M.B., "Interpretation of Fracturing Pressures," *JPT*, **33**, 1767-1775, Sept. 1981.
20. Warpinski, N.R. and Teufel, L.W., "In Situ Stresses in Low-Permeability Nonmarine Rocks," *JPT* **41**, 405-414, April 1989.
21. Gulrajani, S., "An Assessment of Hydraulic Fracture Modeling and Diagnostic Practices," M-Site forum, personal communication, Houston, TX, Nov. 5-6, 1997.
22. Nolte, K.G., "Fracturing Pressure Analysis: Deviations from Ideal Assumptions," SPE20704, 65th SPE ATCE, New Orleans, LA, Sept. 23-26, 1990.

23. Warpinski, N.R., "Dual Leakoff Behavior in Hydraulic Fracturing of Tight, Lenticular Gas Sands," SPE 18259, 63rd SPE ATCE, Houston, TX, Oct. 2-5, 1988.
24. Warpinski, N.R., Uhl, J.E., and Engler, B.P., "Review of Hydraulic Fracture Mapping Using Advanced Accelerometer-Based Receiver Systems," Proceedings, US DOE Natural Gas Conference, Houston, TX, March 24-27, 1997.
25. Warpinski, N.R. Uhl, J.E., Engler, B.P., Lorenz, J.C. and Young, C.J., "Development of Stimulation Diagnostics," GRI Annual Report GRI-97/1327, June 1997.
26. Warpinski, N.R., Branagan, P.T., Engler, B.P., Wilmer, R., and Wolhart, S.L.: "Evaluation of a Downhole Tiltmeter Array for Monitoring Hydraulic Fractures", Proc. 36th U.S. Rock Mechanics Symposium, Columbia University, NY, June 29 - July 2, 1997.
27. Warpinski, N.R., Branagan, P.T., Peterson, R.E., Fix, J.E., Uhl, J.E., Engler, B.P. and Wilmer, R., "Microseismic and Deformation Imaging of Hydraulic Fracture Growth and Geometry in the C Sand Interval, GRI/DOE M-Site Project," SPE 38573, 1997 SPE Annual Technical Conference and Exhibition, San Antonio, TX, October 5-8.
28. Branagan, P.T., Warpinski, N.R., Peterson, R.E., Hill, R.E., and Wolhart, S.L.: "Propagation of a Hydraulic Fracture into a Remote Observation Wellbore: Results of C-Sand Experimentation at the GRI/DOE M-Site Project", SPE 38574, 1997 SPE ATCE, San Antonio, TX, Oct. 5-8.
29. Warpinski, N.R., Branagan, P.T., Peterson, R.E. and Wolhart, S.L., "An Interpretation of M-Site Hydraulic Fracture Diagnostic Results," SPE 39950, 1998 Rocky Mountain Regional/Low Permeability Reservoirs Symposium and Exhibition, Denver, CO, April 5-8.
30. Warpinski, N.R., Branagan, P.T., Peterson, R.E., Wolhart, S.L. and Uhl, J.E., "Mapping Hydraulic Fracture Growth and Geometry Using Microseismic Events Detected by a Wireline Retrievable Accelerometer Array," SPE40014, 1998 Gas Technology Symposium, Calgary, Alberta, Canada, March 15-18.
31. Engler, B.P. and Warpinski, N.R., "Hydraulic Fracture Imaging Using Inclinometers at M-Site: Finite-Element Analyses of the B-Sandstone Experiments," GRI Topical Report, GRI-97/0361, December 1997.

13.0 MAJOR ACHIEVEMENTS

Major achievements include:

The completion of all M-Site results. Of particular importance was the completion of M-Site microseismic analyses for injection 5C and 6C, completion of finite-element analyses of the inclinometer results from the C-sand injections, detailed modeling of the implications of the M-Site results, and the validation of microseismic diagnostics based on the M-Site suite of diagnostic results.

Preparations of papers and reports on the C-sand results, the finite-element tiltmeter results, implications of the M-Site results, the microseismic methodolgy, and others.

The completion of microseismic surveys for Mitchell, Barrett, Crosstimber, and Chevron. While none of these these tests was completely successful in imaging fractures, they were important tests for evaluating and improving the receiver system (the early problems led to purchase of the equipment by a GRI contractor) and for determining if various reservoirs are suitable for microseismic imaging. For example, microseismic signals could be observed at large distances in the Barnett shale (>1500 ft), intermediate distances in the Frontier at Fontanelle (>1000 ft), moderate distances in the coastal Mesaverde at Grand Valley (<800 ft), and could not be observed at long distances (1600 ft) in the Wolfcamp formation at Packenham field.

A re-analysis of the Carthage Cotton Valley Diagnostic Experiment Taylor-sand fracture showing greater lengths than originally thought, and clearly showing the importance of having accurate velocity data when the receivers are either all above the fracture interval or below the fracture interval.

Continued refurbishing of the current 5-level system to upgrade its performance and improve reliability for industry tests.

Initiation of design activities for a new-generation receiver system for wider application.

Development of the SMART5 code into a fully usable real-time event detection code for microseismic imaging and the full porting of the Vidale/Nelson algorithms for use on the PC.

14.0 MAJOR PROBLEMS

The major problems which occurred in 1997 all dealt with problems with the receiver hardware due to minimal maintenance and questionable changes and operations. These problems were being corrected as fast as they could be identified.

15.0 CONCLUSIONS

The M-Site experiments, which were documented in numerous SPE papers, showed that microseismic analyses provide accurate information on fracture height, length and azimuth. All of these geometric parameters were validated using other independent techniques. Fracture height was validated with downhole inclinometers, which measure the deformation of the rock mass in response to the fracture (the mechanical response). Fracture azimuth was verified by intersecting the fracture with a deviated well. Fracture length was validated by fracturing into a pre-drilled deviated lateral well and finding the microseismic length at the time of intersection.

The M-Site experiments have demonstrated a considerable degree of complexity associated with fracture propagation that is not accounted for in most fracture design models. Types of complexity include multiple fractures, secondary and T-shaped fractures, unexpected containment, large pressure drops down fractures, and unexpectedly small created fracture surface areas. Plausible explanations for each of the mechanisms have been postulated, providing a post-evaluation explanation. The difficulty is in predicting these mechanisms a priori so that they can be factored into the design process. It is hoped that continual exercising of the diagnostic techniques developed and evaluated at M-Site will begin to provide the understanding needed to accomplish such predictions.

Field tests of the wireline-retrievable receiver system has shown a considerable number of problems associated with its operation due to poor maintenance, questionable changes, and initial design deficiencies. To make the hardware a reliable system for performing fracture diagnostics, GRI purchased the receiver string through Branagan & Assoc., and Sandia, in cooperation with B&A, will upgrade and repair problem components and designs. In addition, to broaden the range of application, Sandia and B&A are designing a new generation system which can be used in smaller casing sizes, greater temperature ranges, and on industry-available wirelines.

Field tests of the microseismic system have shown that the viewing distance of microseismic events will vary widely from field to field, with observation ranges found to be from 700-1600 ft for the four cases tested.

15.0 OBJECTIVES AND WORK PLANNED FOR NEXT YEAR

The refurbishing of the current 5-level system into a fully working, reliable receiver string for microseismic monitoring will be achieved in 1998.

A new generation microseismic receiver system will be designed, built, and tested in 1998.

Multiple industry diagnostic tests will be conducted in 1998, leading to commercialization of the technology by the end of the year. Along with standard diagnostic tests in a production environment, at least one more elaborate diagnostic test with multiple technologies will be performed. Sandia will continue to support all aspects of design, conduct, and analysis of these tests.

Processing software will continue to be upgraded and refined as new data show weaknesses in the processing algorithms.

Reports, papers, seminars, and workshops will be performed to continue to transfer this technology.